Università degli Studi di Ferrara

DOTTORATO DI RICERCA IN
FISICA

CICLO XXI

COORDINATORE Prof.Frontera Filippo

Magnetostatic interactions in arrays of nanostructures

Settore Scientifico Disciplinare FIS/03

Dottorando
Dott. Bonanni Valentina

Tutore
Dott. Vavassori Paolo

Anni 2006/2008

Contents

Introduction

The understanding of magnetization reversal process in magnetic nanostructures shows interesting aspects both from the scientific point of view and also for potential magneto-electron device applications, such as magnetic field nanosensors (as, e.g., hard disk read-heads) and magnetic random access memories (MRAM). The miniaturization trend demands the theoretical and experimental investigation in this scientific field, especially now that a good understanding of the bulk properties of materials has been achieved.

The rapid development of fabrication and characterization technologies has made it possible to produce and investigate periodic arrays of sub-micron structures in metallic and superconducting films. The correlation of the magnetic properties of patterned arrays with the size and the shape of the single element, as well as with the array spacing and symmetry represent challenges in this investigation field in which the small lenght scale and low dimensionality lead to new and enhanced properties. In particular the study of interacting submicron magnetic structures show many unresolved issues regarding the strength of inter-particle coupling and its dipolar or exchange mediated origin.

In this thesis three different cases have been discussed about the mechanisms of interactions among the magnetic elements of very densely packed systems. An alloy of Ni and Fe, called permalloy (Py) has been selected as ferromagnetic material constituting the presented samples. Its almost vanishing intrinsic magnetic isotropy enables to ascribe the magnetic anisotropy of the investigated sample to only the shape and size of the single element of the array.

The experimental section opens with the study of magnetostatically interacting nanowires, as example of one-dimensional arrays of magnetic dipoles. The investigation has expecially been directed towards the understanding of the influence of the thickness of these ferromagnetic elements on the magnetization reversal process.

The second system is a set of triangular microrings magnetostatically interacting, which are of interest in the research field of the magnetic domain walls and their relative manipulation. The study has been focused on the effects of the dipolar interaction on the pinning of domain walls into the geometrical constrictions of triangular rings.

Finally, the last chapter has been dedicated to trilayered heterostructures, such as patterned arrays of pseudo spin-valves in which a layer of Py has been coupled with a layer of Co, through an interspacer of non-magnetic Cu. Playing with the thickness of the Cu spacer and the different reversal nucleation fields of Py and Co, it is possible to investigate not only the dipolar interaction between the two layers of Py and Co but also the shorter range exchange coupling between the two ferromagnetic layers, mediated by the Cu spacer.

The magnetic domain structure within the micro or nano-objects as well as their remanent magnetization and the shape of their magnetic hysteresis loop may be investigated by a number of experimental methods. In this thesis the Magneto-optical Kerr effect (MOKE) technique is the principal tool of investigation, used for each of the three presented samples. However the higher complexity of the two last samples, the triangular microrings and the trilayered stacks, has required the employment of other experimental techniques. In this way it has been possible to support and complete the picture of the interactions among magnetic structures.

For the Py tringular rings, the complementary measurements have been performed using an imaging technique, the magnetic force microscopy (MFM), and the diffracted magneto-optic Kerr effect (D-MOKE). The hysteresis loops measured with this last technique are proportional to the magnetic form factor and also sensitive to the magnetization structures developing during the reversal process (e.g., domain formation). The investigation of the patterned multilayers has been completed by employing of an element sensitive techinque, the X-ray resonant magnetic scattering (XRMS) and of the Brillouin light scattering (BLS), that has allowed the study of dynamical properties of the samples.

Chapter 1

Nanomagnetic systems

1.1 The Nanomagnetism

Nanomagnetism is the discipline dealing with magnetic properties of structures having dimensions in the submicron range. Although the magnetism is one of the oldest scientific disciplines, the physics of surfaces, interfaces and nanostructures has become one of the main areas of research in the last few decades, driven by the scientific and technologic trend towards miniaturization of physical systems. Oscillatory exchange coupling [1], giant magnetoresistance [2, 3] and perpendicular surface anisotropy [4, 5] are only a few of the exclusive magnetic phenomena discovered during this period. The magnetic properties of the so-called nanomagnets or nanoelements are very different from their parent bulk material, thanks to their extremely small size. In the nanometer regime the surface and interface sites contribute considerably to the magnetic properties and the system results sensitive to local symmetry of these sites. The magnetization shows a different behaviour, for example, varying the substrate or crystal face on which the film is grown or chemisorbing material on the outer surface. In this way new materials with specific properties and response can be created controlling such features. The spin engineering is an example of the application field in the materials' design. The rapid development of thin-film fabrication and surface characterization has led to the improvements in surface preparation techniques and epitaxial growth of thin films. Another important contribution to the high quality of the magnetic elements has come from the development of lithography techniques, that has allowed the patterning of well-defined structures with sub-100nm resolution.

Getting from the growth of thin films to the patterning by lithography, a property of a naturally occuring magnetic element or alloy becomes fundamental: the anisotropy [6], i.e. the presence of preferred magnetization directions within the material. In nanomagnets the anisotropy depends not only on the shape and symmetry of the electronic Fermi surface (as in the bulk) but also on the shape. Therefore another attractive research field is the engineering of the magnetic properties through the choice of the shape of the nano-object, as in the case of the magnetic random access memory (MRAM) and spin-valve magnetic field sensors [7].

In order to provide a theoretical framework in which to interpret the experimental data, the semi-classical formalism of micromagnetics is an appropiate method [8, 9].

1.2 The Micromagnetic modelling

In a thermodynamic context, any system in equilibrium is in a local minimum of the total free energy. In the micromagnetics theory such total free energy is a result of several terms, whose balance determines the material's magnetic properties. If thermal fluctuations are not considered, i.e. the system is at $0K$, this can be written as:

$$E_{tot} = E_d + E_{ex} + E_Z + E_{anis} \tag{1.1}$$

where E_d is the magnetostatic energy, E_{ex} is the exchange energy, E_Z is the Zeeman energy and E_{anis} is the anisotropy energy.

1.2.1 The magnetostatic energy

The magnetostatic energy arises from the stray magnetic field $\mathbf{H_d}$ i.e. the field coming only from any divergence in the magnetization $\mathbf{M}$. The magnetostatic energy density can be expressed in the following term:

$$E_d = -\frac{\mu_0}{2}\mathbf{M} \cdot \mathbf{H_d} \tag{1.2}$$

Low magnetostatic energy favoured a magnetization uniformity, which reduces the "volume charges", and a magnetization arrangement parallel to the structures borders, which minimizes the "surface charges". This often results in a little bending of the magnetization close to the edges and, in drastic cases, in the formation of a new configuration, such as the vortex, that will be successively explained.

1.2.2 The exchange energy

The exchange energy is a quantum mechanical quantity that can be described by a phenomenological approach. Considering the following expression:

$$E_{ex} = -JS^2 \sum_{\substack{ij \\ i \neq j}} \cos \phi_{ij}^2 \tag{1.3}$$

where S is the total spin momentum per atom and ϕ_{ij} is the angle between the directions of the spin momentum vectors of atom i and j, the term J is an integral which may take either sign, the positive and negative signs corresponding to parallel and antiparallel alignment of the spin moments respectively. Wherever there is a gradient in the internal magnetization field, there will be a positive exchange energy term. It follows that an infinite ferromagnet is in a minimum energy condition if all its magnetic moments are aligned parallel. From this point of view, the exchange energy is in competition with the magnetostatic energy (if magnetic anisotropy is negligible) and the equilibrium point is determined by the shape, size and thickness of the object.

1.2.3 The Zeeman energy

Simple application of an external magnetic field brings about this energy density term:

$$E_Z = -\mu_0 \mathbf{M} \cdot \mathbf{H_{ex}} \tag{1.4}$$

Zeeman energy is minimized when the magnetization is aligned with the external field, as we can see from the Eq. (1.4).

1.2.4 The anisotropy energy

For almost every material, the magnetic properties depend on the relative orientation of the magnetization and preferential directions, called easy axes. For a preferential axis **n**:

$$E_{anis} = -\mathbf{K_1}(\mathbf{n} \cdot \mathbf{M})^2 \tag{1.5}$$

There are different sources of the anisotropy: magnetocrystalline, surface and interface anisotropy, strain anisotropy and growth induced anisotropy. The shape anisotropy is already introduced and will be discussed in some length later.

The magnetocrystalline anisotropy is related to the crystal axes of the lattice and it is an effect of the spin-orbit coupling and the crystal symmetry. The relationship between the magnetization and the crystal directions can be phenomenologicaly obtained from symmetry condition. For example, the anisotropy energy density for a cubic crystal can be written as:

$$E_{anis} = K_1(\alpha_x^2\alpha_y^2 + \alpha_y^2\alpha_z^2 + \alpha_z^2\alpha_x^2) + K_2\alpha_x^2\alpha_y^2\alpha_z^2 + \cdots \tag{1.6}$$

where K_1 and K_2 are constants for a specific material [10].

The surface and interface anisotropy is due to the broken symmetry at surface and interface of the system. A common example is the CoPt or FePt thin film where an out-of-plane surface anisotropy leads to a strong easy axis perpendicular to the film surface.

The strain anisotropy is related to the distortion of the crystal or surface shape, giving rise, in the first instance, to a uniaxial term in the magnetic anisotropy. Finally, the growth induced anisotropy is an asymmetry introduced in the material by external source, such as a particular deposition direction or the application of an external magnetic field during the deposition.

1.3 Domains and magnetic configurations.

In presence of a magnetization $\mathbf{M}$, the magnetic field $\mathbf{H}$ can be split in two components, the applied field $\mathbf{H_{ext}}$ and the magnetostatic field $\mathbf{H_d}$, coming only from the magnetization $\mathbf{M}$. For $\mathbf{H_d}$ the following equation is valid: $\nabla \times \mathbf{H_d} = 0$, given that $j = 0$. The most general solution is $\mathbf{H_d} = -\nabla U(\mathbf{r})$. From the third Maxwell's equation ($\nabla \cdot \mathbf{B} = 0$), $\mathbf{B}$ being $\mathbf{B} = \mu_0(\mathbf{M} + \mathbf{H})$ and substituting $-\nabla U(\mathbf{r})$, it is obtained that $U(\mathbf{r})$ is solution of: $\nabla^2 U = \nabla \cdot \mathbf{M}$. Considering the boundary conditions, the solution of the equation can be calculated :

$$U(\mathbf{r}) = \frac{1}{4\pi} \left(- \int_V \frac{\nabla' \cdot \mathbf{M}(\mathbf{r}')}{|\mathbf{r} - \mathbf{r}'|} d\tau' + \int_S \frac{\mathbf{n} \cdot \mathbf{M}(\mathbf{r}')}{|\mathbf{r} - \mathbf{r}'|} d\mathbf{S}' \right) \tag{1.7}$$

From Eq. (1.7) two terms can be identified: a bulk term ($-\nabla \cdot \mathbf{M}$), that is zero when $\mathbf{M}$ is uniform everywhere and a surface term ($\mathbf{n} \cdot \mathbf{M}$), that is zero when $\mathbf{M}$ is parallel to borders.

When a high external field is applied so that the sample reaches a saturated state, uniform magnetization is favoured. At small magnetic field, the magnetization is generally arranged in order to reduce the magnetostatic energy. The way to do so is formation of domains structure, where the magnetization is arranged in a closed flux circuit without leakage outside the material. In each magnetic domain the magnetization is homogenous and oriented parallel to one of the easy directions. At the interface between one domain and the next, the magnetic spins have to change their orientation. Into the material there are then regions, called domain boundaries, which are costly in terms of energy [10]. An excess of anisotropy and exchange energy is stored in domain bound-

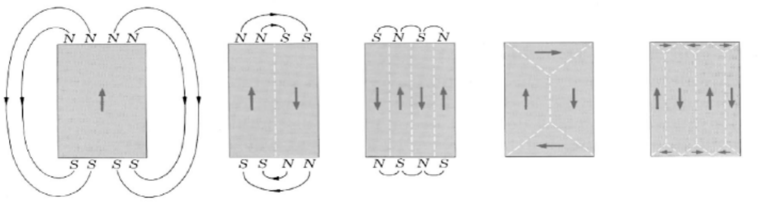

Figure 1.1: Some examples of magnetic domain structures in a rectangular ferromagnet taken from [11]. The magnetostatic energy is considerably reduced for the last two examples where a closure domain configuration is clearly visible.

aries, considering that within the wall each spin is misaligned slightly from its neighbours, against the exchange energy that will tends to align the adjacent spins. On the other hand, these same atomic spins within the wall do not lie parallel to an easy direction, so there will be an anisotropy energy associated with the wall presence. Summarizing, the number and the shape of domains are determined by the balance of three energy terms: the magnetostatic energy and the anisotropy and exchange energies associated with the walls.

Upon sufficient lateral confinement the size of a ferromagnet can become so small that not even a single domain wall can be accommodated inside the system. The magnetization configuration thus becomes a single domain. If then the size becomes too small, the magnetic moment of the single domain ferromagnet can fluctuate due to the thermal energy and the object becomes superparamagnetic [12]. Although the treatment of the domain boundaries is anything but simple, in this context turning to the Bloch wall type can be useful to express the relative strenght of the above energies. In this ideal case, it is assumed that the rotation of the magnetization across the wall is such that the magnetization always lies parallel to the plane of the wall, itself assumed planar [10]. In this way there is no associated magnetostatic energy because there is no divergence of the magnetization across the wall. The energetic cost due to the presence of a domain wall can be evaluated as:

$$\sigma_W = \alpha\sqrt{AK_1} \tag{1.8}$$

where $A = JS^2/a$ is the exchange stiffness constant (J is the nearest neighbours exchange integral value, S is the spin number and a is the unit cell edge) and α is a coefficient depending on the material, the type of boundary and the direction normal to the boundary.

Considering the example of a spherical object with radius R and constituted by a specific material (so that A and K_1 are known) and calculating the energy for the single domain state and for a two domains state, the critical radius below which the former state is energetically stable can be written as [13]:

$$R_{sd} = \frac{36\sqrt{AK_1}}{\mu_0 M_s^2} \tag{1.9}$$

The competition between exchange and dipolar energy can be expressed in terms of the exchange length l_{ex} [14]:

$$l_{ex} = \sqrt{\frac{2A}{\mu_0 M_s^2}} \tag{1.10}$$

The comparison between exchange and anisotropy may be expressed through the length l_w:

$$l_w = \sqrt{\frac{A}{K_1}} \tag{1.11}$$

Another used length scale is l_d, strictly related to the Bloch domain wall energy (1.8), defined as:

$$l_d = 2\frac{\sqrt{AK_1}}{\mu_0 M_s^2} \tag{1.12}$$

The uniform magnetization configuration is favoured when the size of the ferromagnetic element becomes comparable to the domain size. For example, the critical size for a spherical element is $r_{cs} \approx 4l_{ex}$ for a soft magnetic material and $r_{ch} \approx 18l_d$ for a hard one [15]. If the magnet is constituted by cobalt, the critical diameter is $70nm$, whereas for iron is $15nm$ and for nickel is $55nm$. The selection of the magnetic configuration type depends also on the smoothened ends and the aspect ratio of the magnet. For example it was found that a prolate ellipsoid has a $r_{ch} \approx 6l_d$, i.e. three times smaller than the sphere.

A fundamental role is played by the geometric shape. Looking at Eq. (1.7), considering $\mathbf{M}$ uniform inside the body ($\nabla \cdot \mathbf{M} = 0$), only the surface term, that depends on the shape of the object, remains.

The uniformity condition can be realized only for isotropic ellipsoids and for such special cases $\mathbf{H_d} = -\mathbf{N}\mathbf{M}$, where $\mathbf{N}$ is called demagnetizing tensor [16]. Even small perturbations from uniform magnetization which must exist in any nonellipsoidal magnet give rise to an anisotropy called configurational anisotropy.

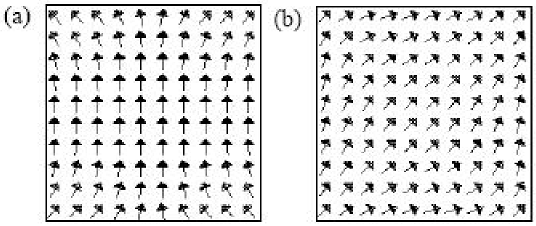

Figure 1.2: Simulated magnetization vector fields in a square nanomagnet of edge $100nm$ and thickness $20nm$ if magnetized (a) parallel to an edge and (b) parallel to a diagonal, taken from [6].

Figure 1.2 shows two examples of equilibrium magnetization vector fields calculated for square nanostructures. The panel (a) shows a plan view of the magnetization vector fields in a nanomagnet of square shape of edge length 100nm and thickness 20nm when it is magnetized parallel to an edge. This configuration is usually named the "flower" because of its flare at the top and bottom. The panel (b) shows the same magnetic object, but when the square is magnetized along its diagonal. This configuration is called "leaf" because of the way that it bows out in the centre and then nips together at the end [6].

The circular shape has a strong potential for nanomagnets, due to its lack of shape anisotropy and configurational anisotropy. If they are constituted by an intrinsically isotropic material, as it is for Py, it results that their magnetization can be changed in direction by a very weak applied magnetic field. It is just in the circular objects that it appears a particular closure domain: the magnetic vortex [17], in which the magnetization direction changes in the plane of the object, lowering the system energy by reducing the stray field. In the core the magnetization is perpendicular to the surface plane, so the only residual magnetostatic energy is confined in this zone of the singularity, that gives to the object two key properties: chirality (clockwise or counterclockwise rotation of magnetization) and polarity (positive or negative direction of the core magnetization), that underlie the dynamic response of submicron structures to rapid magnetic field pulses [11].

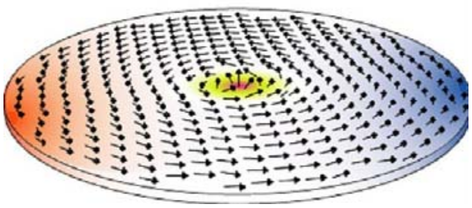

Figure 1.3: Schematic of the magnetization in a vortex configuration. The turned-up core is well visible at the center of the dot.

1.4 The magnetization reversal

Considering the description given until now, the magnetization reversal process is energetically favoured if it passes through a domain walls motion. A coherent rotation means moving the magnetization inside the entire volume away from the easy axis defined by crystalline anisotropy. This implies an energetic cost, which in the case of domain walls motion is absent, since the wall energy necessary at the new position is released at the previous position. Only in the case of domain wall pinning at local defects (non-magnetic impurities, voids, grain boundaries ...) some activation energy is necessary to release the domain wall from the pinning centre.

An irreversible component causing hysteresis and related to the impedance to domain walls motion, is always present. These irreversible processes is the consequence of discretation of magnetization reversal process, corresponding to small, irreversible movements of the domain boundaries (Barkhausen discontinuities) [10].

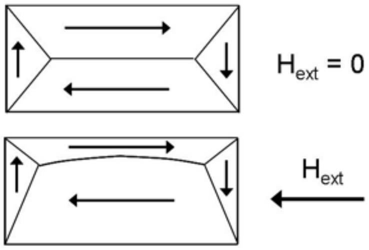

Figure 1.4: Schematics of the effect on a magnetic domain structure by the external magnetic field H

At low fields the Zeeman energy is not too high, the magnetization in every domain is parallel to an easy axis and, in a general case, misaligned with the applied field. With increasing field strength, first domain walls will move and increase the size of domains with a magnetization component parallel to the field. At high fields the domain walls are removed and the magnetization is rotated coherently towards the field direction (Fig.1.4).

In a sample with reduced lateral dimension, the confinement hinders the formation of domains and results in a higher reversal nucleation field (higher coercivity) as compared to continuous film. However, the nucleation field is still smaller than that for coherent reversal. Two different mechanism of incoherent spin rotation, the magnetization buckling and magnetization curling, are now energetically favoured (see also Fig.1.2).

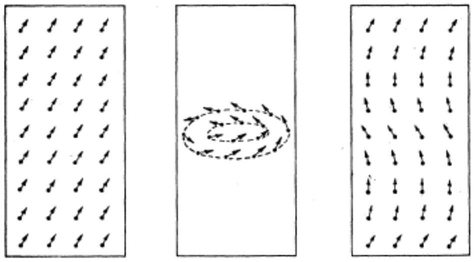

Figure 1.5: Mechanisms of magnetization change in an infinite cylinder, from left to right: spin rotation in unison; magnetization curling; magnetization buckling. Taken from [18].

The coexistence and the balance of possible magnetization reversal mechanisms have not always a simple theoretical approach. Different parameters can influence and determine the process through which it will take place the magnetization reversal, i.e. in elongated ellipses and wires for the external field applied along the short axis (hard direction), the process is almost coherent. However the same type of nanomagnets develops a domain structure (and also not switching by coherent rotation) during the reversal process if the external field H is applied along their major axes. This is confirmed by the absence of a sizable magnetization component perpendicular to H [19]. In such condition, the switching onset field shows different values if the aspect ratio of the elongated magnet is modified [20]. The onset field is assumed to be the field at which the magnetization starts to decrease as effect of reducing of the external field H, after saturation.

Other studies on the effects of changes in shape [19, 21, 22, 23] established that subtle shape defects near the borders of the individual magnets produce a wide range of changes in both the switching field and in the domain structure at remanence. Comparing two samples with similar aspect ratio but different shape of their ends, it results that the presence of domains at the ends of each magnetic particle (end-domains) provides a reverse domain from which to switch easily the magnetization of the rest of the particle. Since the effect of sharp ends is to prevent end-modes formation, magnets with sharp ends show a higher nucleation field than rounded elements.

1.5 The hysteresis loop

In order to develop applications of magnetic materials it is necessary to know the magnetic response of the sample when an external magnetic field is applied. This means to know also the magnetic configuration through that the system passes to reverse its magnetization. The hysteresis loop is just the measurement of the component of the magnetization $\mathbf{M}$ parallel to the applied field $\mathbf{H}$ as a function of the strength of the field. $\mathbf{M}$ is often normalized to the absolute value of $\mathbf{M}$ when it is parallel to $\mathbf{H}$, i.e. when the system is in the saturated state.

When the field is dropped to zero, the ferromagnetic material retains some degree of magnetization (magnetic remanence) and to drive the magnetization to zero it is necessary to reverse and increase the external magnetic field up to value, called coercitive field.

From a micromagnetic point of view, the problem is to determine $\mathbf{m}(\mathbf{r})$, per unit volume, (i.e., $\mathbf{M}$ normalized to the saturation, $\mathbf{m}(\mathbf{r}) = \mathbf{M}/\mathbf{M_s}$) so that the energy is a minimum at any value of the applied field. Recalling the energetic terms of the Eq. (1.1), the total energy of the ferromagnetic object is

$$\epsilon = \int_V \epsilon'_d + \epsilon'_{ex} + \epsilon'_Z + \epsilon'_{anis} d\tau \tag{1.13}$$

with

$$\epsilon'_d = -\frac{\mu_0}{2}\mathbf{h_d} \cdot \mathbf{m} \tag{1.14}$$

where h_d is the stray field normalized to the saturation magnetization M_s.

$$\epsilon'_{ex} = -A\left[(\nabla m_x)^2 + (\nabla m_y)^2 + (\nabla m_z)^2\right] \tag{1.15}$$

where A is the macroscopic exchange constant specific for the material.

$$\epsilon'_Z = -\mu_0 \mathbf{m} \cdot \mathbf{h} \tag{1.16}$$

where h is the external field H normalized to saturation magnetization M_s.

$$\epsilon'_{anis} = -K_1(\mathbf{m} \cdot \mathbf{n})^2 \tag{1.17}$$

where K_1 is the first-order anisotropy constant.

Considering small variation of the magnetization vector around its value $\mathbf{m^{(0)}}$, bound by the constraint that the magnitude of $\mathbf{m}$ must be 1, it is possible to obtain Brown's equations [9]:

$$\begin{cases} \mu_0 M_s \mathbf{m} \times \mathbf{H_{eff}} = 0 \\ \frac{\partial \mathbf{m}}{\partial \mathbf{n}}\big|_{\Omega} = 0 \end{cases} \tag{1.18}$$

with

$$\mathbf{H_{eff}} = \mathbf{H} + \mathbf{H_d} + \frac{2}{\mu_0 M_s} \nabla \cdot (A \nabla \mathbf{m}) - \frac{1}{\mu_0 M_s} \frac{\partial E_{anis}(\mathbf{m})}{\partial \mathbf{m}} \tag{1.19}$$

The first of Brown's equations shows that the torque exerted on magnetization by the effective field must vanish at equilibrium and that the magnetization is parallel to the effective field.

The minimization of the total energy equation can find an equilibrium magnetization distribution, but it should be considered that the energy landscape of micromagnetic systems is usually very complicated, with various local maxima and minima. Therefore, the choice of the initial magnetization distribution can strongly influence the result. The micromagnetic approach can then be facilitated by a dynamic description of the path through the energy landscape.

Considering that the motion of a magnetic moment in a magnetic field is mainly governed by its Larmor precession around the local magnetic field and introducing as damping a phenomenological term, necessary to establish the experimentally observed magnetization reversal in an applied field, the Gilbert equation is obtained [24]:

$$\frac{d\mathbf{M}}{dt} = -\gamma \mathbf{M} \times \mathbf{H} + \frac{\alpha}{M_s} \mathbf{M} \times \frac{\mathbf{M}}{dt} \tag{1.20}$$

where γ is the gyromagnetic ratio, $\gamma = g\mu_B/\hbar$.

The second term on the right represents the torque caused by the damping (α is the damping parameter). The magnetization is not precessing but it spirals down to a stable configuration with $\mathbf{M}$ parallel to $\mathbf{H}$.

It is possible to demonstrate that the Gilbert equation is equivalent to an older form, the Landau and Lifshitz equation:

$$\frac{d\mathbf{M}}{dt} = \frac{1}{(1+\alpha^2)}\left[-\gamma \mathbf{M}\times\mathbf{H} - \frac{\alpha\gamma}{M_s}\mathbf{M}\times(\mathbf{M}\times\mathbf{H})\right] \tag{1.21}$$

This equation is applied and computed in the simulation program used in this thesis work and explained in the next chapters.

Chapter 2

The interactions among nano-structures

In the previous chapter the influence of various parameters on the magnetic properties has been discussed for single nanomagnets. All of the experiments presented in this thesis work and many of the potential technological applications of nanomagnets are performed with a large ensemble of magnetic objects (dots) arranged on some lattice. If the lattice spacing is sufficiently small the magnetic field leaking out of one nanomagnet can influence its neighbours and the geometry of the lattice, as well as the shape of the motif, has to be considered.

The principal coupling inside the magnetic array is the dipolar interaction, usually defined as a long-range force. But there are other types of coupling, at shorter range, as the magnetic interaction across the interface between a ferromagnetic and an antiferromagnetic spin system (exchange coupling); or as the interaction between two ferromagnetic materials through a non-magnetic interlayer (interlayer exchange coupling).

2.1 The dipolar interaction

The dipole-dipole interaction depends on a term $1/r^3$, so in a packed system, not only the distance between the centres of the magnetic elements but also the distance between the edges of them becomes important. Supposing a direction along which the spacing between nanomagnets is sufficiently reduced, the magnetostatic coupling becomes an anisotropic coupling, with an energy minimum (easy axis) when the dipoles are aligned with this joining direction and an energy maximum (hard axis) when aligned perpendicular to this direction.

The effects of the interaction are various, e.g., change of the coercive field or susceptibility [6] and will be more significant in systems with a small crystalline and shape anisotropy and consequently, small saturation and coercivity [14]. Several experiments were done to investigate and understand the dots' dipolar interaction and to valuate the flexibility and the control of magnetic devices [25, 26, 27]. Moreover, it has been shown that by controlling the shape of the dots and varying the lattice symmetry, it should be possible to tailor the magnetic ground state of arrays of magnetic dots [28].

Another important factor influencing the interactions among dots is the magnetization state of each individual dot. It is just explained as the magnetic state tends to reduce the external stray field in zero applied field (there are even configurations in which this stray field is absent, e.g., closure domains or vortex state). The dipolar interaction among these magnetic objects should be negligible at low external field and should become significant only at large applied field, near the saturation. If instead single domain elements are considered, the interaction field depends on their thickness because of the proportionality between the dipolar field and the magnetic moment. A similar argument concerns also the type of material composing the magnetic dots or the direction of the magnetization, i.e. if it is in plane or out of plane.

In order to have a simplified picture of the effect of dipolar interactions, it is convenient to consider two dipoles as are represented in the figure 2.1, such as with moments parallel to each other and perpendicular to their separation line. The dipolar field H_i, generated by the first dipole and acting on the second one, is opposite to the magnetization direction and tends to reverse it. Supposing that the two dipoles have a slightly different switching field H_{1s} and H_{2s} ($H_{1s} < H_{2s}$), as is possible given that two magnetic elements are never

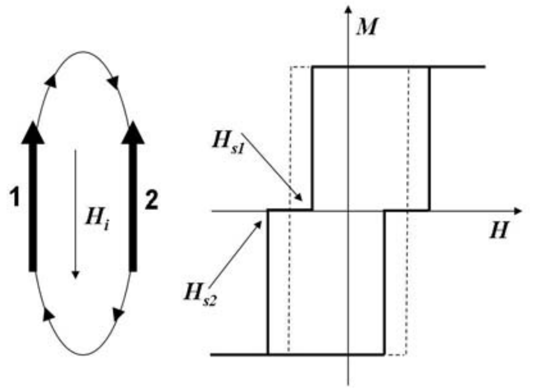

Figure 2.1: Schematic of the dipolar field H_i and the hysteresis loop for a system constituded by two magnetic moments parallel to each other and perpendicular to their separation distance. The dashed line represent the hysteresis loop of a single dipole moment.

identical, the dipole with switching field H_{1s} will reverse itself first stabilizing the unswitched second dipole. In the hysteresis loop it results in two jumps (one for each dipole reversal), instead of a single jump as it is observed for a single object. Even if both dipoles had the same switching field H_s, they would reverse themselves simultaneously, but at a value of external field $H = |H_s| - |H_i|$, i.e. smaller than that of a single element.

In the other case, showed in figure 2.2, in which the two dipoles are collinear, the switching field is larger than that of the individual dipoles, because the dipolar field is parallel to the moment direction and tends to stabilize the unswitched state. Moreover the two dipoles reverse themselves at the same value of external field, even in the case of slightly different switching fields.

In arrays every aspect illustrated in these two examples become more complex, so this kind of explanation is a good starting point but is not sufficient to describe the magnetic samples. Moreover it is almost always impossible to consider the magnetic dots as single dipoles because of their finite size which at short distances becomes critical in the determination of the created field. Even the change in the coercive field H_c, i.e. the switching field discussed above, reports several contradictory results with respect to the theory in many stud-

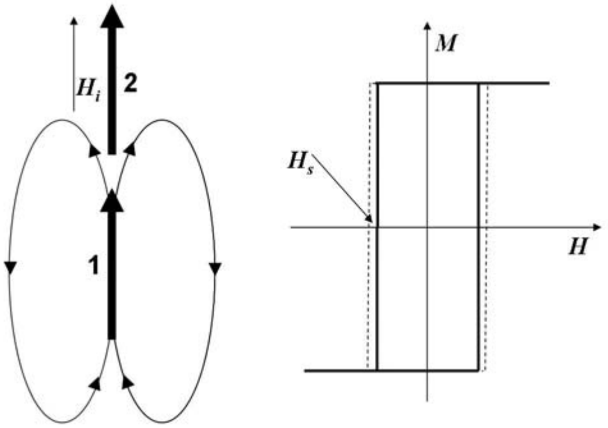

Figure 2.2: Schematic of the dipolar field H_i and the hysteresis loop for a system constituded by two magnetic moments parallel to each other and also to their separation distance. The dashed line represents the hysteresis loop of a single dipole moment.

ies of different materials or differently shaped elements or differently structured arrays.

2.2 The interlayer exchange interaction

Among the various short-range interactions, now the interlayer coupling through a non-magnetic material will be introduced, because it was topic of study for a system presented in this thesis.

The interest in the interlayer coupling on the magnetic switching of a multilayer was already born in the mid-eighties, but it is with the discovery of the giant magnetoresistance (GMR) [2, 3] that it significantly increased, leading to the nobel prize of Physics in the 2007. It becomes necessary to understand the physics of coupling and its effects on the properties and stability of magnetic structures as spin-valves or magnetic tunnel junctions (MTJs) [29].

A first approach consists in considering a bilinear interaction between the ferromagnetic layers (Fig.2.3), i.e. a coupling energy proportional to the magnetization product:

$$E_c = -J\mathbf{m_i}\mathbf{m_{i+1}} = -J\cos(\theta_i - \theta_{i+1}) \tag{2.1}$$

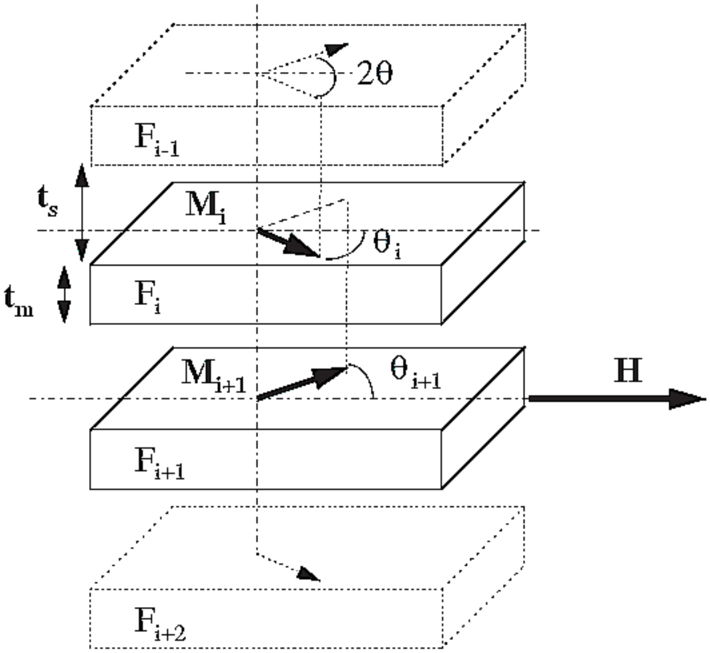

Figure 2.3: Schematic of the bilinear interaction between ferromagnetic layers in a multilayered system, taken from [30].

where J is the coupling constant, m_i and $m_{i+1}$are the magnetization unit vectors of two consecutive ferromagnetic layers in the multilayer structure and θ_i and θ_{i+1} are the angles between the magnetization of the two specific layers and the applied field direction [30]. A positive interaction is relative to a parallel alignment between the magnetizations of the two layers and the coupling is called ferromagnetic, in the same way, a negative coupling induces an antiparallel alignment and is called antiferromagnetic. Generally, this bilinear term in multilayered structures results from the combination of two contributions: the conduction-electron-mediated exchange coupling, which oscillates in sign as a function of the thickness of the non-magnetic spacer and which is related to the RKKY (Ruderman-Kittel-Kasuya-Yosida) model [31, 32, 33]; and the dipolar magnetic coupling (also know as Néel or ‘orange peel’ coupling), which is ferromagnetic and comes from magnetostatic charges present at the interfaces and induced by surface roughness. In presence of variations in the spacer layer thickness, the intralayer exchange coupling being finite, a second coupling contribution, a biquadratic term is generated [34]. Actually the forms of this term are various and difficult to predict, as its sources and to separate those from others is often difficult and not well defined. The biquadratic coupling was introduced because of discrepancies between the bilinear model and experimental results. It is primarily explainable through physical defects and in particular the presence of so called pinholes [35, 36].

2.2.1 Oscillatory exchange coupling

When the thickness of the non-magnetic layer is sufficiently reduced to make the dipolar interaction between consecutive magnetic layers negligible, the coupling is substantially an exchange interaction through the electrons of the spacer layer. When the thickness of this latter is varied, the coupling can oscillate in sign, as was observed both in transition metal [37, 38] and in rare-earth systems. Several studies about such systems show a rather general feature of these oscillations [39, 40], typical of the RKKY interaction between magnetic impurities in a non-magnetic host. In both cases, interfaces in the present case and impurities in the other one are coupled to each other by their influence on the electrons in the spacer or host, respectively. Several refinements are introduced throughout the last recent years [41, 42, 43], emphasizing the role of the intrinsic properties of the spacer material, namely its Fermi surface [44]. Without entering in a specific theory, it is in anyway important to stress that other strategies and models were introduced to explain the interlayer exchange coupling [45, 46], in particular for transition metals, for which the itinerant electrons have to BE taken into account [47].

2.2.2 The Néel or 'orange peel' coupling

Already in 1962 Néel introduced a ferromagnetic coupling between magnetic films in contact due to the magnetic dipoles at the interface induced by a morphological corrugation [48, 49]. This model thus concerns a kind of magnetostatic interaction on a microscopic scale, in which the roughness of the thin film creates magnetic poles at the surface, considering that the intralayer exchange is strong enough to prevent the magnetization from rotating and following the surface profile. The directionality of the roughness and the relative correlation with the magnetization direction that can be uniform or fluctuating, makes the argument more complex. In general it refers to ‘orange peel’ when the coupling is a bilinear term, i.e. when the magnetization is considered uniform and the roughness correlated. When these two conditions fail, the ‘orange peel’ coupling becomes zero, but there is still a microscopic magnetostatic contribution to biquadratic coupling [46].

2.2.3 The biquadratic coupling: pinholes

The pinholes represent a break in the spacer layer that connects the two ferromagnetic layers through a direct exchange coupling and for this reason, ferromagnetic coupling. They were born as a frustration in the separation of magnetic layers, but throughout the years have shown interesting aspects, that have encouraged their investigation in particular when the bilinear coupling is antiferromagnetic [35]. In fact, even when pinholes do not dominate the bilinear coupling, they can cause a biquadratic coupling in an appropriate distribution, due to the thickness fluctuation of the spacer.

Chapter 3

Magneto-optical Kerr effect

The magneto-optical Kerr effect (MOKE) is the principal technique employed to investigate the magnetization mechanisms of each sample discussed in this thesis work. Therefore this entire chapter has been dedicated to explain the physical basics and the measurements setup of this technique.

The classic MOKE measurements have been supported, for the last two studied samples, by other techniques that will be described in the next chapter.

3.1 Basics

In the magneto-optical Kerr effect (MOKE) [50, 51], the magnetization of a ferromagnetic sample breaks the spatial as well time reversal symmetries, causing the change of polarization and/or intensity of the light beam reflected by the sample surface.

The transmission analogous to the Kerr effect is the Faraday effect, where the polarization of the light beam transmitted through the ferromagnetic material is changed from the polarization of the incident light beam [52].

The Kerr effect can be observed in three different dispositions of the magnetization with respect to both the plane of incidence and the sample reflecting surface [53]. In the polar configuration the magnetization is perpendicular to the sample surface and it is often performed at normal incidence. Longitudinal and

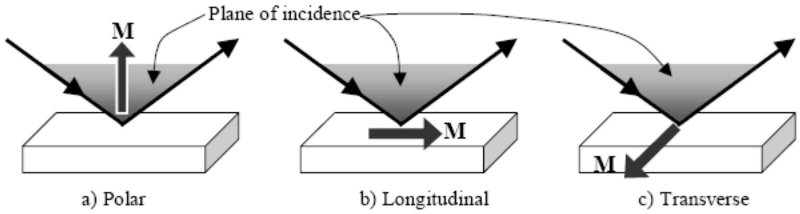

Figure 3.1: Geometry of the three magneto-optical Kerr effects: polar; longitudinal and transverse. Taken from the work 'Magneto-Polarimetry Advanced Lab' by John Cerne, Physics Department University at Buffalo, SUNY Buffalo, NY.

transverse MOKE operate at a certain angle of incidence, with a magnetization parallel to the sample surface, either parallel (longitudinal) or perpendicular (transverse) to the optical plane of incidence.

The simplest model to explain the MOKE phenomenon is to consider a Lorentz-Drude model for a metallic film. The incident light causes an electrons oscillation parallel to the plane of polarization. In the presence of a non-ferromagnetic sample, the polarization plane of the reflected light is the same as the incident light. When the sample has an own magnetization that acts on the oscillating electrons through a Lorentz force, like an internal magnetic field, the result is a second oscillating component perpendicular to the direction of the magnetization and to the primary motion. Using a linearly polarized incident light, the polar and longitudinal MOKE yield the orthogonally polarized component upon reflection whereas the transverse geometry only affects the intensity, i.e. the amplitude of the incident polarization [54].

However, the complexity of MOKE theory requires a quantum description, that stems from the need for explaining the large magneto-optical effect in the ferromagnetic materials [55].

It is with Heisenberg that the Weiss theory, postulated to account for the existence of ferromagnetism, begins to be explained through the exchange interaction among electrons. Although this is not sufficient to explain the magneto-optic effects, because it is not the electron motion that determines the dielectric properties of a material. The solution is in the spin-orbit coupling, introduced by Hulme [56] and improved by Kittel [57] and Argyres [58]. The spin-orbit interaction couples the magnetic moment of the electron with its motion, connecting the magnetic and optical properties of a ferromagnet. This effect is present also in the non-magnetic materials, but it is only in the ferromagnets that it manifests itself thanks to the unbalanced number of spin up and spin down electrons.

3.2 Macroscopic formalism

The macroscopic formalism to explain the MOKE effect is the same used for the other magneto-optical effects. If the linearly polarized incident light is considered as a superposition of two circularly polarized components, the Faraday effect, as also the Kerr effect, can be thought as the result of two processes [55]. First, the two circularly polarized modes propagate with different velocities, gaining two different phase shifts and resulting in a rotation of the polarization plane. Second, the material absorbs differently the two modes, resulting in an ellipticity phenomenon.

Considering for the moment the polar Kerr effect at normal incidence, the complex refraction index of the sample is n_+ for the right circularly polarized light and n_- for the left circularly polarized light, where $n_\pm$ can be conceived as $n(1 \pm \frac{1}{2}Q)$. Q is the so-called Voigt's magneto-optical constant, that is proportional to the value of the magnetization in the linear approximation. The reflected amplitude, such as the Fresnel coefficient, will be:

$$r = |r|\, e^{i\phi} = \frac{E_1}{E_0} = -\frac{n-1}{n+1} \tag{3.1}$$

Therefore, it is that:

$$\frac{r_+}{r_-} = \left|\frac{r_+}{r_-}\right| e^{i(\phi_+ - \phi_-)} \tag{3.2}$$

using the indices + and − to denote, for each cited quantity, the right and left circularly polarized light, respectively. If the incident light is linearly polarized, the reflected light will be elliptically polarized because the circular components, in which it is resolved, will no longer have equal amplitude and the major axis will be rotated from the direction of incident polarization because of the phase difference introduced between these circular vibrations [59]. This rotation angle, the Kerr rotation, is given by:

$$\vartheta_K = -\frac{1}{2}(\phi_+ - \phi_-) \tag{3.3}$$

considering that the minus sign is due to the reflected light travelling in the negative direction, in accordance with a coordinate system where the z direction is positive if going into the sample surface.

The Kerr ellipticity will be instead:

$$\epsilon_K = \frac{|r_+| - |r_-|}{|r_+| + |r_-|} \tag{3.4}$$

To first order in $(n_+ - n_-)$, such as to first order in Q, the two terms become:

$$\vartheta_K = -\Im\left(\frac{n_+ - n_-}{n_+ n_- - 1}\right) = -\Im\left(\frac{nQ}{n^2 - 1}\right) \tag{3.5}$$

$$\epsilon_K = \Re\left(\frac{n_+ - n_-}{n_+ n_- - 1}\right) = \Re\left(\frac{nQ}{n^2 - 1}\right) \tag{3.6}$$

The relation among the components of the magnetization, the Voigt's constant Q and the Kerr rotation and ellipticity, can be resumed introducing the dielectric tensor of the medium ϵ, that can be decomposed into a symmetric, thus diagonalizable and an antisymmetric part, that gives rise to the Kerr effect. Considering a thick magnetic film where the multiple reflections could be ignored [60], when a light beam is incident on this ferromagnetic medium 1,

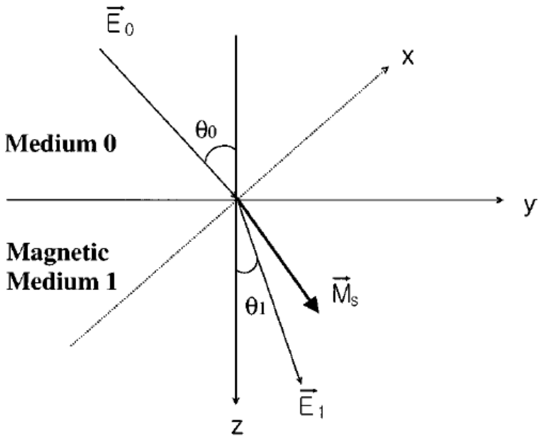

Figure 3.2: The coordinate system of a non-magnetic medium 0 and a magnetic medium 1. The direction of the magnetization is arbitrary. Taken from [60].

from a non-magnetic medium 0, the dielectric tensor ϵ can be written as:

$$\epsilon = \epsilon_{xx} \begin{pmatrix} 1 & -iQm_z & iQm_y \\ iQm_z & 1 & -iQm_x \\ -iQm_y & iQm_x & 1 \end{pmatrix} \tag{3.7}$$

m_i are the direction cosines of the magnetization vector M_s and Q is the already cited Voigt's magneto-optical constant. At this point is useful to clarify that there are two different sign formalisms to describe of dielectric tensor and also the sense of magneto-optically induced rotations and ellipticities [61]. The coordinate system and the sign convention chosen in this treatment are the same used by Ref. [62] and Ref. [63] and resumed in the Ref. [60].

The reflection from the sample can be evaluated through the Fresnel reflection matrix:

$$R = \begin{pmatrix} r_{pp} & r_{ps} \\ r_{sp} & r_{ss} \end{pmatrix} \tag{3.8}$$

where the terms r_{ij} are the Fresnel reflection coefficients, with the indices j and i related to the polarization of the incident and reflected electric field, respectively. s is the polarization state perpendicular to the plane of incidence, whereas p

is the polarization state parallel to the plane of incidence. The complex Kerr angle can be now written as:

$$\theta_K^p = \vartheta_K^p + i\epsilon_K^p = \frac{r_{sp}}{r_{pp}}, \qquad \theta_K^s = \vartheta_K^s + i\epsilon_K^s = \frac{r_{ps}}{r_{ss}} \tag{3.9}$$

with ϑ_K and ϵ_K the Kerr rotation and ellipticity.

The r_{ij} will be dependent on magnetization components, refractive index and refraction angle inside the ferromagnetic medium, in different way depending on the geometry of the magnetization in relation to the plane of incidence and the sample plane.

The investigations presented in this thesis work involve an in-plane magnetization and are mainly performed in the longitudinal (magnetization parallel to the plane of incidence) geometry. In this configuration, with $m_y = 1$ and $m_x = m_z = 0$, the coefficients r_{ij} are expressed by [64]:

$$r_{pp}^l = \frac{n\beta - \beta'}{n\beta + \beta'} \tag{3.10}$$

$$r_{ss}^l = \frac{\beta - n\beta'}{\beta + n\beta'} \tag{3.11}$$

$$r_{ps}^l = -r_{sp}^l = \frac{\gamma\beta\kappa_2}{n^2\beta'(n\beta + \beta')(\beta + n\beta')} \tag{3.12}$$

where $\kappa_2 = in^2Q$, $\beta = \cos\theta$ (θ is the angle of incidence measured from the sample normal) and $\beta' = \sqrt{1 - (\sin^2\theta/n^2)}$.

3.3 Optical components in a measurement setup

The magneto-optic response is measured with a homebuilt SMOKE system [65] sketched in Fig. 3.3. The incident light originates from a He-Ne laser, passes through a rotatable Glan-Thompson polarizer, incides on the sample surface and it is reflected. The reflected light beam passes through a photo-elastic modulator (PEM), vibrating at a frequency $\omega = 50kHz$ and through a second rotatable Glan-Thompson polarizer, to be finally detected by a pre-amplified photodiode. The components of the detected signal modulated at ω and 2ω are measured with two lock-in amplifiers, whereas the dc component of the signal is measured with a high precision voltmeter. The sample is positioned between the poles of a two-axes ferrite electromagnet in order that the magnetic field H can be applied in the sample surface plane, parallel or perpendicular to the plane of incidence.

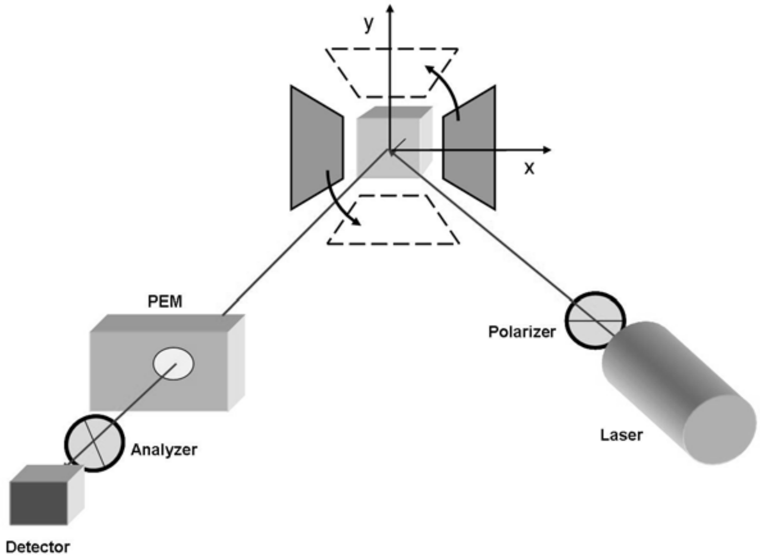

Figure 3.3: Schematic of the classic magneto-optic setup.

The optical arrangement can be analyzed by using the Jones-matrix formalism [66], where the polarization state of the incident and the reflected electromagnetic waves is expressed by a column vector:

$$\mathbf{E} = \begin{pmatrix} E_p \\ E_s \end{pmatrix} \tag{3.13}$$

where the subscriptions p and s denote the electric field components, normalized to one, parallel (p) and perpendicular (s) to the plane of incidence.

Every optical element can be represented by a 2x2 matrix, expressing the polarization change of the light passing through this element. A sequence of optical elements is expressed as the product of the Jones matrix of each element.

In the measurements presented in this thesis work, the incident light is polarized perpendicular (s) or parallel (p) to the plane of incidence. The matrices describing a polarizer that sets these two polarization state are, respectively:

$$\mathbf{P_s} = \begin{pmatrix} 0 & 0 \\ 0 & 1 \end{pmatrix} \qquad \mathbf{P_p} = \begin{pmatrix} 1 & 0 \\ 0 & 0 \end{pmatrix} \tag{3.14}$$

The analyser, in contrast, is positioned at a certain angle θ_a respect to the incidence plane and its matrix results to be:

$$\mathbf{A} = \begin{pmatrix} \cos^2\theta_a & \sin\theta_a\cos\theta_a \\ \sin\theta_a\cos\theta_a & \sin^2\theta_a \end{pmatrix} \tag{3.15}$$

The sample is described by the reflection matrix $\mathbf{R}$, showed in Eq. (3.8).

The photo-elastic modulator is used for modulating or varying at a fixed frequency, the polarization of the light beam. The PEM principle of operation is based on the photoelastic effect, in which a mechanically stressed sample exhibits birefringence proportional to the resulting strain. Creating an optical axis in the PEM, a linear polarization of light, parallel to the optical axis, have a slightly different speed from that of a linear polarization perpendicular to this axis. Defining Δn the difference between the two respectively indices of refraction, it is given that $\Delta n = A\cos\omega_M t$. A is proportional to the amplitude of the voltage applied to the piezoelectric transducer causing the vibration, at the frequency ω_M in the photoelastic material. The phase angle introduced between two waves travelling through the PEM, with polarization parallel and perpendicular to the optic axis, is $\phi = \frac{2\pi\Delta n l}{\lambda}$, where l is the thickness of the optical element and λ is the wavelength of the incident light. The matrix of the photo-elastic modulator can be written as:

$$\mathbf{P} = \begin{pmatrix} 1 & 0 \\ 0 & e^{i\phi} \end{pmatrix} \tag{3.16}$$

if the optical axis of the PEM is perpendicular to the plane of incidence, thus parallel to the **s** polarization direction.

As just explained, the signal measured in the Kerr experiment can be expressed as the product:

$$i_f = \frac{I_f}{I_{dc}} = \frac{|\mathbf{A} \cdot \mathbf{P} \cdot \mathbf{R} \cdot \mathbf{E}|^2}{I_{dc}} \tag{3.17}$$

where f is the frequency of the measured signal (ω_M or $2\omega_M$), I_{dc} is the dc intensity and $\mathbf{A}, \mathbf{P}, \mathbf{R}, \mathbf{E}$ are the Jones matrices described above. Supposing that the incident light is polarized s, from Eq. (3.17), neglecting terms of second order in the magnetization ($|r_{ps}|^2$ in this case), it is for the normalized lock-in output at ω and 2ω:

$$i^s_\omega = C_1 f(\theta_a) \Im \{r_{ss} r{*}_{ps}\}, \qquad i^s_{2\omega} = C_2 f(\theta_a) \Re \{r_{ss} r{*}_{ps}\} \tag{3.18}$$

where $f(\theta_a) = \sin\theta_a / \cos\theta_a$, $C_1 = -4J_1/\sqrt{2}\,|r_{ss}|^2$ and $C_2 = 4J_2/\sqrt{2}\,|r_{ss}|^2$. $J_1 = 0.519$ and $J_2 = 0.432$ are, respectively, the first and the second order Bessel function evaluated at $\phi = 137.8°$ [67]. In fact, the term ϕ in the Jones matrix of the PEM [Eq. (3.16)] is proportional to $\cos\omega_M t$. If $e^{i\phi}$ is expanded in the following manner:

$$e^{i\phi} = e^{i\frac{2\pi A l}{\lambda}\cos\omega t} = J_0(\phi_M) + 2iJ_1(\phi_M)\sin\omega t + 2J_2(\phi_M)\cos 2\omega t + \dots \tag{3.19}$$

and if $\phi_M = \frac{2\pi A l}{\lambda}$ is set at 137.8°, J_0 results to be equal to zero and the first and second order Bessel functions have the values cited above. The other higher order terms of Eq. 3.19 are negligible not because are small, but because the lock-in detections are limited to measuring signals at ω_M and $2\omega_M$ frequencies.

Considering Eq. (3.18) and the relations between Kerr rotation ϑ_K and Kerr ellipticity ϵ_K [Eq. (3.9)], it is simple to show that the former term i^s_ω is proportional to the Kerr ellipticity, whereas the latter term $i^s_{2\omega}$ is proportional to the Kerr rotation.

It is interesting to remark the relation that connects the measured signal with the magnetization components, through the Fresnel reflection coefficients r_{ij}:

$$\Re\left\{r_{ss}r*_{ps}\right\} = \Re\left\{g^s_1(n\,Q\,\theta)\right\}m_x - \Re\left\{g^s_2(n\,Q\,\theta)\right\}m_z \qquad (3.20)$$

where g^s_i are functions of the complex refraction index n, of the Voigt's magneto-optical constant Q and of the incidence angle θ.

Similar relation is obtained if the incident light is polarized parallel to incidence plane (p- polarization), so that, with opportune arrangement and approximations, the measurement of the single magnetization components is possible . However this thesis work is not interested in to measure the absolute value of samples magnetization (normalized to its saturation value), that after all requires a certain number of experiments [65]. To study the interaction effects between nanomagnetic structures is sufficient to obtain the rotation and ellipticity quantities that contain the magnetization, though they are not simply proportional to it.

Chapter 4

The complementary techniques

As explained in the previous chapter, in addition to classic MOKE, other techniques have been selected and employed to investigate the magnetization behaviour of two of the samples discussed in this thesis. In this chapter the basic description of such techniques is separated in two parts, relative to the two samples: the Py triangular microrings and the trilayered Py/Cu/Co nanodots. For the former sample the used complementary techniques are: the diffracted magneto-optic Kerr effect (D-MOKE) and the magnetic force microscopy (MFM). For the trilayered samples the complementary techniques are: the X-ray resonant magnetic scattering (XRMS) and the Brillouin light scattering (BLS).

4.1 The Py triangular microrings

4.1.1 Diffracted magneto-optic Kerr effect

When a light beam is incident upon a sample that has a periodic structure with a pitch comparable to the wavelength of the radiation, the beam is not only reflected but is also diffracted. Given that the reflected light from a magnetic material carries information about the magnetic state of the sample, to wonder whether the diffracted beams also carry magnetic information becomes very interesting . Experimental data confirm this theory and indicate that this magnetic information is different to that of reflected beam [68, 69, 70, 71]. The resulting hysteresis loops can exhibit unusual shapes, caused by the magnetization structures developing during the reversal process, e.g., domains formation or vortex configuration. The diffracted magneto-optic Kerr effect (D-MOKE) is also a powerful tool to understand the magnetization reversal path in patterned magnetic arrays, to address the possible mechanisms of magnetization reversal and to test the validity of many assumptions that are made in micromagnetic simulations.

As it has already been explained in the third chapter, there are three different MOKE geometries: polar, longitudinal and transverse. This last one is sensitive to the in-plane component of the magnetization M that is perpendicular to the incidence plane. Calculating the Fresnel reflection coefficients for the transverse geometry, one should note that the reflected light does not undergo rotation ($r_{ps} = r_{sp} = 0$) and that the only quantity depending on magnetization is the component r_{pp} [64]. There is no a priori reason that one should use one of the three geometries for the D-MOKE measurements, however it is preferred the transverse one that, depending only on one Fresnel coefficient, simplifies the interpretation of the data.

The theoretical approach to the D-MOKE problem requires the complete diffraction theory including the magneto-optical contributions, resulting very complex. The formalism that will be use here for the interpretation of measured loops of studied samples, is quite clear, but not rigorous [72]. Therefore it has to be treated with some caution since it may not be valid for all situations. The purpose of this analysis is not to attempt to predict the intensity of the magneto-optic effects, but to describe the behaviour of the intensity changes caused by changes in the magnetization configuration within the single particle of the studied array.

Considering the transverse MOKE, the Fresnel coefficient r_{pp} can be separated in two components:

$$r_{pp} + m_y r_{pp}^m \tag{4.1}$$

where r_{pp} and r_{pp}^{m} are, respectively, the non-magnetic and magnetic parts of the reflectivity, and m_y is the averaged magnetization component, normalized to the saturation value, perpendicular to the scattering plane. Restricting to reflected and diffracted beams in the scattering plane (plane xz, in the chosen coordinate system), the electric field in the nth order diffracted beam E_n can be considered as:

$$E_n = E_0 \left[r_{pp} f_d(n) + r_{pp}^{m} f_d^{m}(n) \right] \tag{4.2}$$

with E_0 the incident electric field and $f_d(n)$ the non magnetic form factor, defined as:

$$f_d(n) = \int\int exp\left[in(2\pi/L)x\right] dS \tag{4.3}$$

where the integration is carried out over one unit cell of the array, L is the array period in x direction and n is an integer. $f_d^{m}(n)$ is instead the so called magnetic form factor of order n and can be written as:

$$f_d^{m}(n) = \int\int m_y exp\left[in(2\pi/L)x\right] dS \tag{4.4}$$

The intensity of the measured loops, i.e. the variation $\Delta I_d^{m}(n)$ of the intensity of the nth diffracted order, can be considered proportional to [73]:

$$\Delta I_d^{m}(n) \propto \Re\left[f_d^{m}(n)\right] + A(n)\Im\left[f_d^{m}(n)\right] \tag{4.5}$$

For $n = 0$, i.e. in the case of reflected beam, the signal $\Delta I_d^{m}(0)$ is just proportional to the average value of m_y in all dots of the array, the D-MOKE loop is like a standard averaging loop of the classical MOKE. On the other hand, at higher order of diffraction, the loops contain information about the Fourier components of the magnetization and consequently provide information on the magnetization distribution within the unit cell of the array, i.e. the single dot of the array. The number $A(n)$ can be evaluated from r_{pp} and r_{pp}^{m}. However, this requires an accurate knowledge of all the optical constants of substrate and particles, the magneto-optic coefficients, the thickness of the particles and the incidence angle. Therefore $A(n)$ is usually treated as an adjustable parameter, being the uncertainties affecting the measurements large due to the material inhomogeneity.

4.1.2 Magnetic force microscopy

The basic concept of a force microscopy is the measurement of a force between the sample surface and a sharp tip, mounted on the end of a cantilever which serves as force sensor [74]. In the MFM system the tip is coated with a ferromagnetic thin film and previously magnetized so that the detected force is the one acting on the magnetic dipoles contained in the ferromagnetic material on the tip located in the magnetic field produced by the ferromagnetic sample (Fig.4.1). Any scanning probe method needs of a piezoelectric actuator in order to achieve a good spatial resolution. Piezoelectric materials change their shape in an electric field due to their anisotropic crystal structure. By means of applying a high voltage to a bar of a such material, its lenght's variation can be controlled. Another necessary component of the instrument is a controller, that calculates line-by-line the $x-y$-position of the scanning probe. The z-position, i.e. the tip-sample separation, is controlled by a closed-loop feedback system. Finally mechanical stability and vibrational isolation are essential prerequisities to achieve a high-resolution of the microscope.

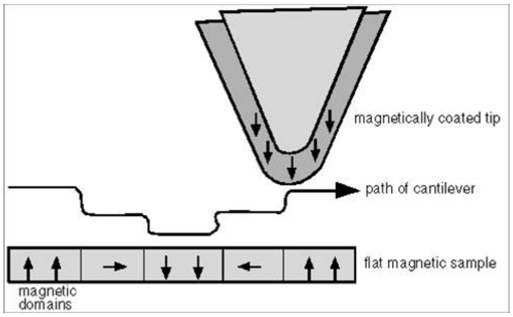

Figure 4.1: Schematic of the map of magnetic domains in a sample surface by the magnetic force microscope.

Several modes of operation are possible in the force microscopy and can be divided into two groups, the static and the dynamic modes. The formers control the static bending of the cantilever, whereas the latters measured its dynamic properties, e.g., the eigenfrequency, the oscillation amplitude or the phase between excitation and oscillation. Furthermore, the operation modes are often distinguished with respect to whether the tip is in contact with the sample's surface or not.

The tip-sample magnetic forces are tipically two or three orders of magnitude smaller than the other tip-sample forces in a scanning force microscope dedicated to measuring the topography of the sample. Assuming that the force and the direction of the cantilever are aligned in the z direction, the deflection of the cantilever due to the magnetic interaction between the tip and the sample can be written:

$$\delta z_{mag} = \frac{F_{mag}}{k_{eff}} \tag{4.6}$$

where $k_{eff} = k_L + \frac{\partial F_{nonmag} + \partial F_{mag}}{\partial z}$, k_L is the force constant of the free cantilever and $\partial F_{nonmag}/\partial z$ is the z component of the force derivative of all non-magnetic tip-sample interactions. In order to avoid the strong non-magnetic interaction due to topography-dependent forces, the magnetic force microscope must be operated in non-contact mode.

In most scanning force microscopy experiments, the control of the distance tip-sample is obtained keeping constant the interaction between them. To reach a good feedback stability it is necessary that the sign of the derivative of the measured interaction does not change. This condition is fulfilled in the topographical forces, but in the case of magnetic forces the repulsion and attraction within the imaged sample area complicate the measurements. However this operation mode has been used in the early MFM experiments, introducing additional servo-forces. Anyway this difficulty can be partially overcome if the control interaction is different from the magnetic tip-sample force. In practice, a distance-dependent physical property is used as an input signal for the tip-sample distance feedback, while local variations in the magnetic force lead to a varying magnetic interaction.

The MFM used for the measurements of the Py triangular microrings is an A.P.E. Research AFM A50-CL tool with a tip coated by CoCr and magnetized to be a north pole. The system operates in non-contact mode and controls the changes of the tip-sample distance by the changes in the amplitude of the resonant frequency of the cantilever.

As already introduced, an image taken by the MFM instrument contains both the topographic and magnetic properties of the sample surface and a scan height of about $100nm$ was then used in order that the predominant effect is the magnetic one.

4.2 The trilayered Py/Cu/Co nanodots

4.2.1 X-ray resonant magnetic scattering

The observation and performing of magneto-optical effects at x-ray wavelengths is strongly related to availability of high-brilliance synchrotron light sources with tuneable photon energy and polarization. The microscopic origin in nearly every magneto-optical effects is based on electric dipole transitions driven by the electric field of the electromagnetic radiation. In the case of the visible light, the photon energy allows to probe the intraband transitions and being the spin-orbit energy within the d shell in $3d$ transition metals of the order of $0.1eV$, the magneto-optical effect results small. The situation changes significantly for $2p \rightarrow 3d$ interband transitions, since the spin-orbit splitting of L_2 and L_3 edges reaches values of the order of tens eV and the effect becomes much larger. In this case the photon energies lie in the soft x-ray range between $512eV$ and $870eV$ considering the $3d$ transition metals between V and Ni.

The use of x-rays for studies of magnetic properties is more than a simple extension of visible light investigations because it offers the possibility to separate the magnetic hysteresis of a selected element, by tuning the photon energy to a specific absorption edge. This is a powerful tool in the field of magnetic heterostructures and it is the reason for which this probe was chosen for studying the Py/Cu/Co nanodots. Moreover the x-rays allow to investigate the magnetic contributions of different kinds of valence electrons by probing the various absorption edges of the same element according to the dipole selection rules. However this latter aspect was not treated in the performed studies of this thesis.

The more relevant among these x-ray effects is the x-ray magnetic circular dichroism (XMCD) [75], defined as the difference in the absorption of the left- and right-circularly polarized x-rays in a sample with the magnetization along the photon propagation direction. The x-ray resonant magnetic scattering (XRMS) combines the advantages of XMCD with the characteristics of the conventional x-ray scattering [76]. Under resonant conditions, the scattering becomes sensitive to the spatial distribution of magnetic and orbital moments, e.g., to the presence of a well defined long range magnetic structure or to the setup of orbital ordering [77].

The microscopic interaction between x-rays and matter can be described in terms of scattering amplitude:

$$f(\mathbf{q},\omega) = f^0(\mathbf{q}) + f'(\omega) + if''(\omega) \tag{4.7}$$

where $f(\mathbf{q},\omega)$ is related to the differential cross section:

$$\frac{d\sigma}{d\Omega} = |f(\mathbf{q},\omega)|^2 \tag{4.8}$$

The first term of Eq.4.7 gives rise to the non-resonant Thomson scattering, the second one is the resonant scattering while the last one is related to the absorption. If the photon energy is tuned close to an absorption edge, the resonant scattering term will be dominant and the process can be viewed as absorption of the initial photon exciting an electron to an intermediate state, the decay from which leads to emission of a photon. Following the notation of Hannon [76] the resonant scattering amplitude, in the dipole approximation, can be written as the sum of three terms of order 0, 1 and 2 in $\mathbf{m}$, i.e. the unit vector of the atomic magnetic moment:

$$f^{res} \propto (\mathbf{e_f^*} \cdot \mathbf{e_i})F^{(0)} - i(\mathbf{e_f^*} \times \mathbf{e_i}) \cdot \mathbf{m}F^{(1)} + (\mathbf{e_f^*} \cdot \mathbf{m})(\mathbf{e_i} \cdot \mathbf{m})F^{(2)} \tag{4.9}$$

with

$$\begin{aligned} F^{(0)} &= [F_1 + F_{-1}] \\ F^{(1)} &= [F_1 - F_{-1}] \\ F^{(2)} &= [2F_0 - F_1 - F_{-1}] \end{aligned} \tag{4.10}$$

e_f and e_i are the polarization vectors of the incoming and outgoing photons and F_i is related to the coupled between the ground state and the excited state with a change ΔM $(= +1, 0, -1)$ in the magnetic quantum number. These functions $F_{\Delta M}$ are directly connected to the diagonal and off-diagonal elements of the dielectric tensor. The term proportional to $(\mathbf{e_f^*} \cdot \mathbf{e_i})$ is sometimes called anomalous scattering and it does not depend on the magnetization. The second term, linear in $\mathbf{m}$, is directly related to the x-ray equivalent of Kerr effect, as well as of circular dichroism. The third term in Eq.4.9 is second order in the magnetization and causes linear dichroism or the Voigt effect.

From Eq.4.9 is clear that in a magnetic sample the relative orientation between the polarization of incoming and outgoing photon determines the components of the magnetization contributing to the scattering amplitude. The experimental geometry is coplanar (Fig.4.2), i.e. the scattering plane coincides with the incidence plane (xz-plane). In such conditions for an elastic scattering process, the photon momentum transfer $\mathbf{q} = \mathbf{k_f} - \mathbf{k_i}$ can be considered as:

$$\begin{aligned} q &= |\mathbf{k_f} - \mathbf{k_i}| = \tfrac{4\pi}{\lambda}\sin(\theta) \\ q_x &= q\sin(\Delta\theta) = \tfrac{4\pi}{\lambda}\sin(\theta)\sin(\Delta\theta) \\ q_z &= q\cos(\Delta\theta) = \tfrac{4\pi}{\lambda}\sin(\theta)\cos(\Delta\theta) \end{aligned} \tag{4.11}$$

where $\theta = \theta_D/2$ and $\Delta\theta = \theta_S - \theta$, i.e. the deviation from the specular condition.

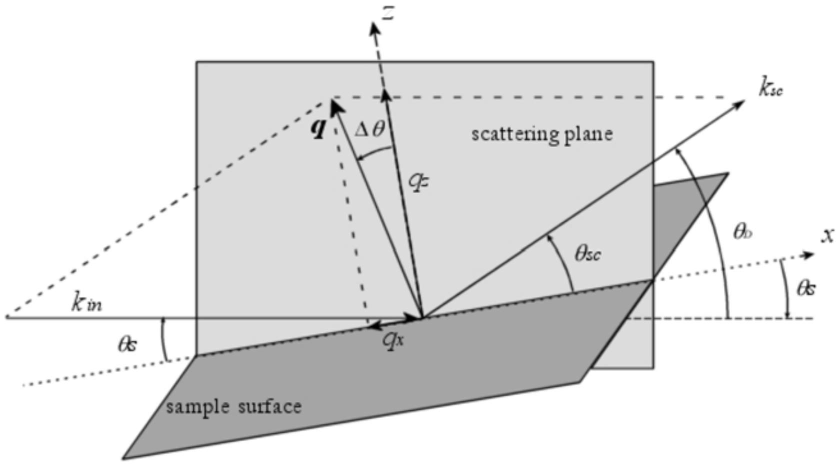

Figure 4.2: Schematic of co-planar scattering geometry with the notation adopted in the text. Taken from [77].

4.2.2 The Brillouin light scattering

The Brillouin light scattering is generally referred to the inelastic light scattering from thermally excited spin waves and offers the possibility to explore the dynamical magnetic excitations in ultrathin film as well as in multilayered metallic structures.

The induced modulation of the optical constants of the medium, achieved via the magneto-optic interaction in the case of spin waves, can be considered in analogy with the elasto-optic effect caused by acoustic phonons, but every peculiarity related to the polarizability and the transverse nature of the electromagnetic waves have to be taken into account [78].

In a BLS experiment, a beam of highly monochromatic light is focused on the surface of the sample and the light scattered within a solid angle is analysed in frequency using a multi-pass Fabry-Perot interferometer. This last one is required in order to extract and separate the weak inelastic component of light from the elastically scattered contribution [79]. If the process is viewed as a two-particles diffusion, a photon and a magnon (the energy quantum of spin waves), the conservation of the wave vector brings that the wavelength of the revealed spin waves is of the same order of the magnitude as that light, i.e. much larger than the interatomic distances. Therefore the medium can be considered as a continuum.

The BLS measurements offer also the way to determine different magnetic parameters as the saturation magnetization or intra- and inter-layer exchange constants, monitoring the spin wave frequencies as a function of the direction and magnitude of the in-plane wave vector $q_{\|}$ and of the direction and strength of the applied magnetic field H. Figure 4.3 shows a typical setup of a BLS experiment in the backscattering configuration, which is usually exploited in studies of thin films or layered structures. In this geometry, the magnon wave vector component parallel to the sample surface $q_{\|}$ is linked to the optical wave vector k_i by the following simple relation:

$$q_{\|} = 2k_i \sin\theta_i \tag{4.12}$$

where θ_i is the angle of incidence of light. The energy conservation guarantees that if $\hbar\omega_L$ is the energy of the incident photon and $\hbar\omega$ is the energy of the magnon then the energy of the backscattered photon will be $\hbar(\omega_L \pm \omega)$ according

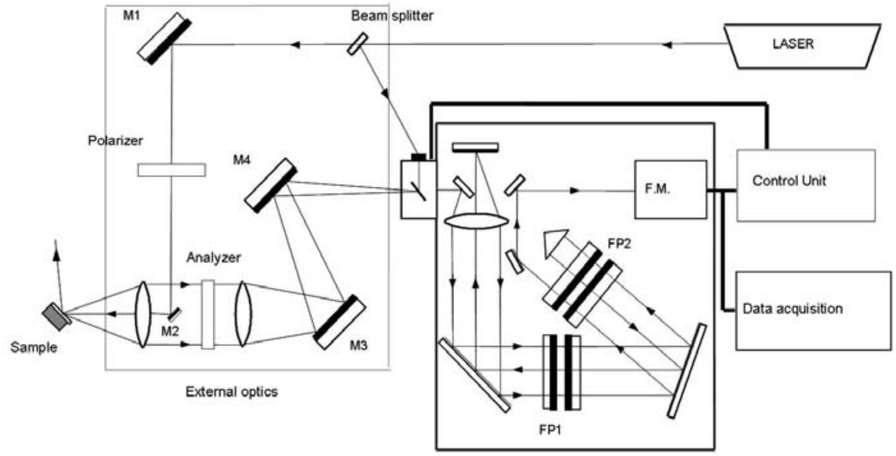

Figure 4.3: Schematic of the Brillouin scattering apparatus, taken from [78].

to the magnon absorption or creation in the process, respectively.

Chapter 5

Magnetization reversal process in interacting Py nanowires

This chapter is dedicated to study the magnetization reversal process in interacting Py nanowires, using the vectorial magneto-optical Kerr effect magnetometry. It opens with an overview of the problem, focusing then on the specific investigated case. A section has been dedicated to previous studies of interacting and isolated Py nanowires in order to have a starting point to show the experimental results.

5.1 The sample

5.1.1 Magnetostatically interacting nanowires

In data storage devices, the reduction of the spatial separation of the elements is essential in order to increase the bit areal density. For this purpose, the study of the magnetic long-range interactions among the elements constituting the array becomes fundamental for testing and investigating the magnetization reversal process and the domains structures.

Advances in lithographic fabrication techniques have given rise to the possibility of producing arrays of laterally controlled magnetic structures of a few nanometers size.

In the wide set of investigated magnetic systems [6, 80, 81], the fabrication and characterization of nanostructures have received a considerable interest. There are various techniques for fabricating a such system, these include electro-beam lithography and lift-off technique [82], inrotating-water quenching technique [83], epitaxial growth on single crystal and electrodeposition on nanoporous template [84]. The main problem with electro-beam lithography is the difficulty to produce closely packed nanoelements arrays due to the proximity effects. Moreover, its serial writing process results too slow for making a large area fabrication. Electrodeposition offers a cheap and simple way to fabricate arrays of cylindrical nanowires but their orientation and spacing result difficult to control due to the distribution of pore size and orientation of the nanoporous membranes [85]. Being interested in investigation of the magnetization reversal process, the selected fabrication technique of the presented nanowires is the deep ultraviolet (DUV) lithography and lift-off process. This technique is a parallel process that allows to obtain in relatively short time highly ordered closely packed nanoelements arrays with an extreme uniformity in width and interwires spacing [86].

For an individual long wire the magnetization reversal is determined by its strongly shape anisotropy, but for a wires array in which the inter-wire spacing is much smaller than the lateral size of the wires, the magnetization reversal of the individual magnetic element affects the behaviour of its neighbours due to the stray field emanating from its edges.

Even an array composed of few ferromagnetic wires turns out to be very intricate, although it could seem a quite simple problem to study. The complication is that the magnetic fields resulting from the dipolar interaction depend on the magnetization state of each entity, which, in turn, depends on the effective field of neighboring elements [87].

Previous studies on interacting microwires [87, 88, 89] have showed that the hysteresis loops of a such system, for the external applied field parallel to the wires axis, are characterized by defined Barkhausen jumps corresponding each to the magnetization reversal of individual microwires. These jumps can be theoretically interpreted according to a model based on the nucleation of closure domains at the ends of the wires and the subsequent depinning and propagation of a domain wall [89].

If all wires were really identical, they would feel exactly the same effective field and they would reverse at exactly the same field value. In real situation this does not happen and the wires can display fluctuations in both magnetization and coercive fields. Since some wires reverse magnetization before the others, an energy stable structure is achieved for an antiparallel alignment among the wires. Therefore, the intrinsic reversal field distribution plays a crucial role for similar systems, also in the case of nanometric wires, as demonstrated by a previous work about the comparison between two arrays of Py parallel nanowires with the same thickness and width but different inter-wires spacing [90]. In the non-interacting case, the magnetization reversal is ruled by the distribution of energy barriers for the reversal nucleation, determined by the morphological defects. In case of interacting nanowires the magnetization reversal takes place through a series of steps followed by plateaus corresponding to stable magnetization configurations related to the antiparallel aligment of wires.

The dipolar interaction influences the way in which the magnetization reversal proceeds after the initial stage. Angular dependent measurements can help to understand such mechanisms, varying the orientation of the applied field relative to the nanowires easy axis [84, 91]. A cross-over from coherent reversal mode to curling magnetization is observed when the thickness to width ratio of the wires exceeds a specific value [91]. Applying the external field parallel to the hard axis of the interacting wires, the saturation fiels H_s is given by [92]:

$$H_s \approx H_k + \frac{3}{2} H_d \tag{5.1}$$

where H_k is the intrinsic magnetic anisotropy field (negligible in the structures studied in this thesis) and H_d represents the average demagnetizing field. For wires arrays H_d can be estimated as [93]:

$$H_d = 4\pi M_s \frac{t}{w} \alpha(r) \tag{5.2}$$

where s, t, w are inter-spacing, thickness and width of the wires, respectively and $\alpha(r)$ is a function of (s/w) in order that if the ratio $(s/w) \rightarrow 0$ also the factor $\alpha(r) \rightarrow 0$, while, if $(s/w) \rightarrow \infty$, then $\alpha(r) \rightarrow 1$. With such conditions, the two limit cases of a continuous film and isolated wires are taken into account. This relation confirms that the wires thickness is a fundamental parameter, in fact if the inter-spacing and the width of wires are fixed, an increasing of the wires thickness leads to an increasing of the demagnetizing field and also to an increase in the saturation field.

5.1.2 Sample description

The samples presented in this chapter are large area ($4 \times 4mm^2$) arrays of Py nanowires with a fixed width of $185nm$, spacing of $35nm$ and varied film thickness from 10 to $120nm$ (Fig.5.1). As already explained, they are fabricated using the deep ultraviolet lithography (DUV) at $248nm$ exposing wavelength and lift-off process, employed by the Information Storage Materials Laboratory of the Department of Electrical and Computer Engineering of the National University of Singapore. The hysteresis loops have been measured using a vectorial magneto-optic Kerr effect magnetometry and microscopy setup [65]. With the vectorial magnetometry (V-MOKE) the measurements apparatus is sensitive to both in-plane components of the magnetization, parallel (longitudinal loop) and orthogonal (transverse loop) to the external applied field H. In this way it is possible to reconstruct the magnetization vector at any step of the magnetization reversal.

To gain more information about the reversal process, the laser beam has been focused over a circular spot with a diameter of about $7\mu m$ (μ-MOKE). In this way the measured hysteresis loops are relative to only a few wires of the

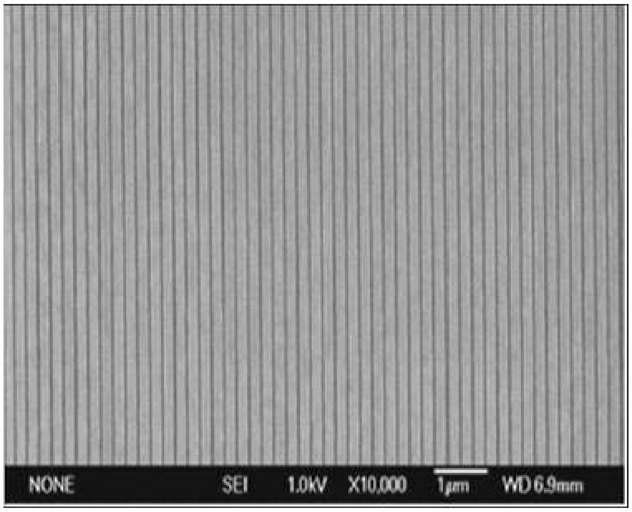

Figure 5.1: Scanning electron microscopy image showing the lateral dimensions of the nanowire arrays(the image is taken from the $20nm$-thick wires sample).

sample, as it will be explaned afterward.

The purpose of the study presented in this thesis is to investigate the strong influence of the thickness on the magnetization reversal process for magnetostatically interacting nanowires [94].

5.2 Interacting and isolated Py nanowires: previous studies

The already cited work [90] about the two arrays of Py nanowires (one interacting and the other isolated) will be often recalled in the section dedicated to the experimental results of the presented nanowires arrays. In fact these two systems are very similar to the samples studied in this chapter: the same material, fabrication technique, almost the same width and interwires spacing and also the same investigation technique. In the first istance, it has allowed the estimation of the number of wires illuminated by the focused beam and the consequent beam diameter ($7\mu m$). As already introduced and as it will be explaned in more detail for the measurements relative to this thesis, both the hysteresis loops measured in Ref. [90] with μ-MOKE technique show visible steps, evidenc-

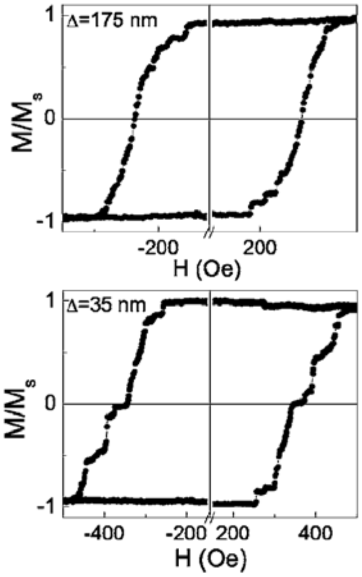

Figure 5.2: μ-MOKE easy axis magnetization curves of the paper [90] for two arrays of wires with same thickness ($20nm$) and same width ($175nm$) but different spacing ($\Delta = 175nm$ in the upper panel and $\Delta = 35nm$ in the lower panel). The field H is applied parallel to the easy direction.

ing how the magnetization reversal is occuring through the separate switching of either individual wires or groups of a few wires (Fig. 5.2). The evaluation of height of the smallest steps observable in both the loops recorded from the two samples (non-interacting and interacting wires) leads to the estimate of the number of wires illuminates by the focused beam. Since such height is about 1/30 and 1/20 of the total MOKE signal for the interacting and non-interacting wires, respectively, and since such smallest step is consistent with the switching of a single wire, the total number of illuminated wires is about 30 and 20 in the two cases (consistent with a diameter of the beam of about $7\mu m$).

Being the wires quite long (order of hundreds μm), the magnetization reversal could take place through domain walls motion and the observed step could then be relative to a partial switch of one wire. However, the plateau following the analysed step covers a field range of tens Oe in both samples, thus, it is very likely that the step is relative to the switch of a single wire.

This work shows also the differences between the longitudinal hysteresis loops measured along the easy and hard axis for the two interacting and isolated wires arrays. The magnetostatic interaction between the wires does not affect the onset of the magnetization reversal process, because the role of defects is dominating. However the applied field range required for the magnetization reversal is substantially wider for the interacting sample. The effects of the dipolar interaction are visible in the way in which the magnetization reversal evolves.

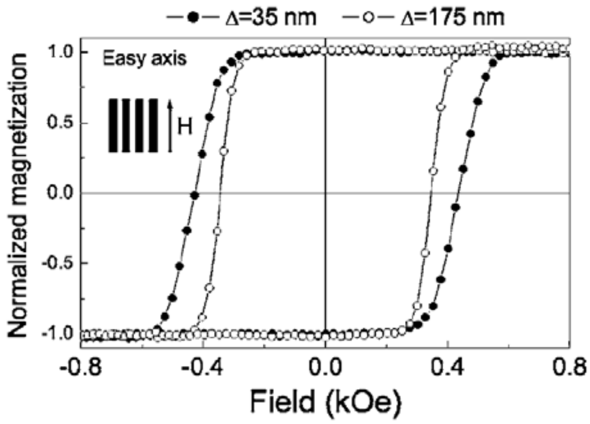

Figure 5.3: Comparison between the longitudinal hysteresis loops for the two wires array (interacting and isolated) studied in the paper [90]. Δ indicates the spacing between the wires of the array (full point correspondes to $\Delta = 35nm$ and open points to $\Delta = 175nm$). The external field is applied parallel to the easy axis.

Applying the external field H along the hard axis, the hysteresis loops show a lowering of the saturation field for the interacting nanowires compared to the isolated case. The magnetostatic interaction between the neighboring wires has the same direction of the applied field and the effective demagnetizing field in each wire is then reduced.

5.3 The micromagnetic simulations

A representative simulation has been performed by using the OOMMF package [95], in order to show how the magnetization reversal is strongly affected by the reversal fields distribution due to defects of the wires array. The material parameters are those contained in the OOMMF program for Py, i.e. saturation

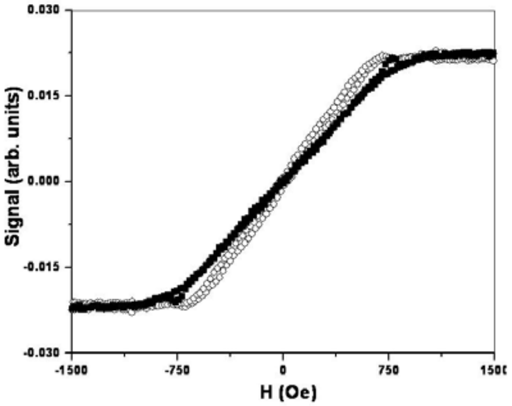

Figure 5.4: Comparison between the longitudinal hysteresis loops for the two wires array (interacting and isolated) studied in the paper [90]. Δ indicates the spacing between the wires of the array (full point correspondes to $\Delta = 35nm$ and open points to $\Delta = 175nm$). The external field is applied parallel to the hard axis.

magnetization $M_s = 800 \times 10^3 A/m$ and exchange stiffness constant $A = 1.3 \times 10^{-11} J/m^3$. The material has been considered lacking in magnetocrystalline anisotropy and the cell dimensions are fixed to $10 \times 10 \times 10nm^3$. An array of only ten wires has been simulated, the width of each wire has been fixed to $180nm$, the length to about $1.2\mu m$ and the inter-wire spacing is $30nm$. The same array has been simulated modifying three of the ten wires (reducing their width to $140nm$) in order to introduce the defects that lead to a different switching field of the wires.

5.4 Experimental results

5.4.1 The V-MOKE measurements

Applying the magnetic field H parallel to the wires length (easy magnetization direction), only the longitudinal component has been observed (Fig.5.5).

The coercivity results strongly dependent on the thickness of the film and the $t = 80nm$ delimits a critical region, over which the coercivity begins to decrease as thickness is increased, after that it has increased for thickness values between $10nm$ and $80nm$. This non-monotonic thickness dependence of the coercive field

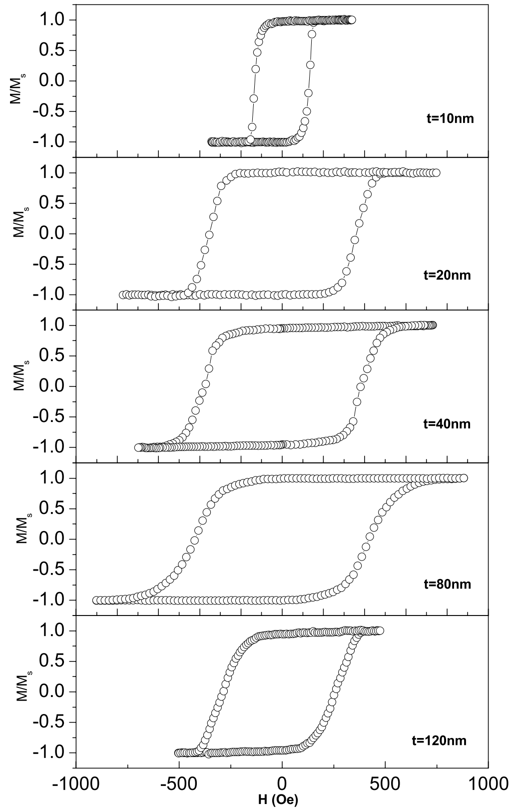

Figure 5.5: Representative hysteresis loops of nanowire arrays of different thickness t measured with the external field H parallel to the wires length.

suggests that there may be a cross-over in the magnetization switching mode at a critical thickness above $80nm$ value. To further investigate this aspect, the hysteresis loops recorded applying the external field H perpendicular to the wires length were measured (hard magnetization direction). In this geometry both the in-plane magnetization components (parallel and perpendicular to the field H) are observed (Fig.5.6). In the film thickness range $10nm \leq t \leq 80nm$ the transverse component, normalized to the magnetization saturation value, reaches the maximum value of 1 at zero external field H while the longitudinal component goes to zero, as expected. Moreover, the longitudinal loops display a negligible hysteresis, demonstrating that, for thicknesses in this range, the reversal takes place with a coherent rotation of the magnetization of all wires. A slight misalignment between H and the wires edges is inevitable and determines

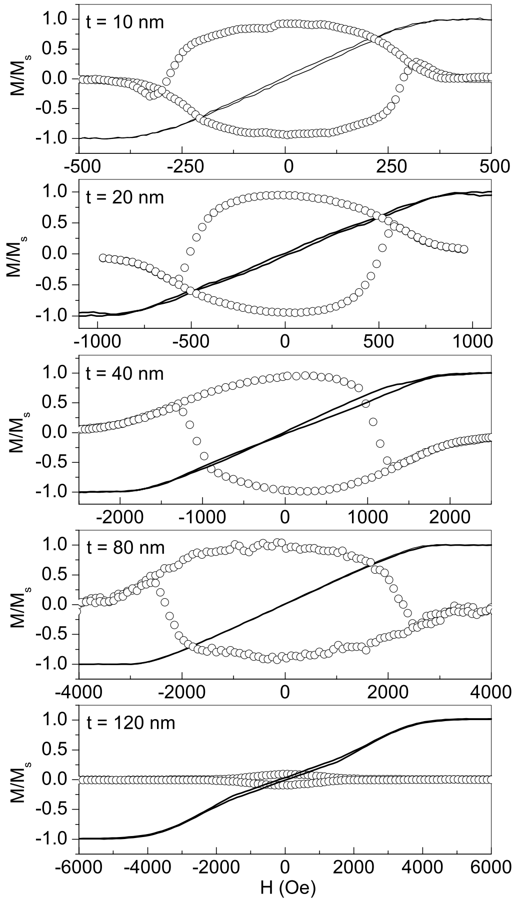

Figure 5.6: Measured in-plane magnetization components parallel (solid lines) and perpendicular (open dots) to the external field H as a function of H applied perpendicular to the wires length, for wires of different thickness t.

the sense of rotation of the magnetization for all wires because the small component of H parallel to the wires length biases the rotation of the magnetization towards the same direction.

In the case of $t = 120nm$ the transverse component of the magnetization is markedly suppressed and the longitudinal loop shows also a reduction of the slope in the H range between $-2000Oe$ and $2000Oe$. These results indicate that the magnetization reversal does not occur in the $120nm$-thick wires through a coherent rotation process. As explained in the first chapter, several mechanisms may characterise the magnetization reversal in nanostructures: coherent rotation, magnetization curling, buckling or domain wall motion. In this case it can be said that the magnetization reversal becomes inhomogeneous and the mechanism involves probably the formation of several magnetic domains, considering the wires length (hundreds microns) and the wires thickness ($120nm$).

5.4.2 The μ-MOKE measurements

The μ-MOKE measurements have been performed applying the external field H parallel to the wires length, in order to deepen the effects of the magnetostatic dipolar interaction. The comparison among the μ-loop portions relative to the magnetization reversal, for different thicknesses, shows how, for a $t \geq 20nm$, the loops exhibit a number of Barkhausen jumps and plateaus while in the $10nm$-thick sample, the magnetization reversal occurs in a single large Barkhausen jump (Fig.5.7). As already introduced, the plurality of jumps and plateaus

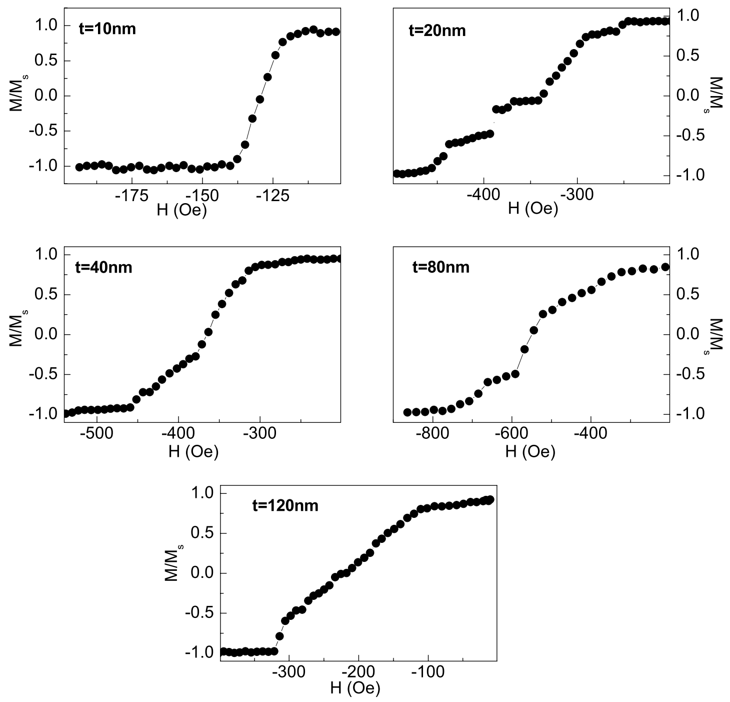

Figure 5.7: The portion of the hysteresis loops during the reversal from $+H$ to $-H$ recorded for the different t-samples, focusing the laser beam over a circular spot with diameter of about $7\mu m$.

evidences that the reversal is occurring through the successive switching of either individual wires or groups of a few wires. Therefore, there is a distribution of the switching fields of the single wires and the width of the distribution is increasing with the film thickness (for $t \geq 20nm$).

It is important to stress that the dipolar interaction does not cause the presence of the steps in the hysteresis loops, but determines their stability (as showed by the wide plateaus), decreasing the demagnetizing field if the neighboring elements are aligned antiparallel.

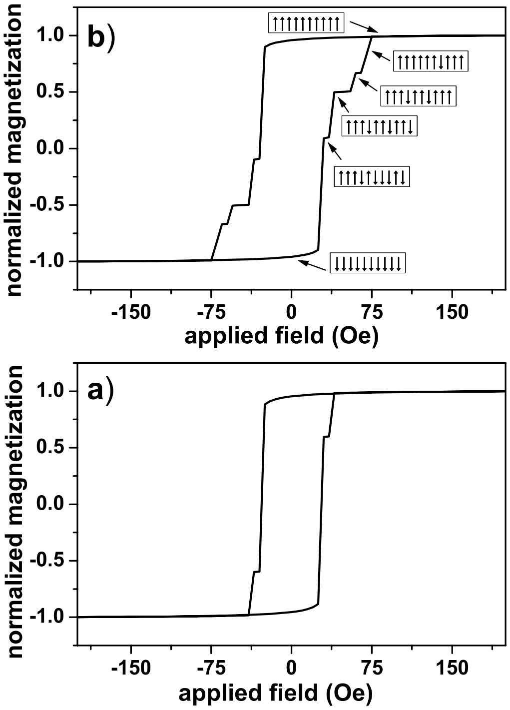

Figure 5.8: The calculated hysteresis loops of an array of 10 identical interacting wires (a) and the hysteresis loop for the same array in which three wires have been made thiner (b). The insets in panel (b) show the progressive switching of the 10 wires.

The performed simulations verify two important aspects, on the one hand the hysteresis loops of the two calculated arrays of ten wires show, on a quality level, the fundamental role played by the defects. Modifying three wires of the ten-wires array, the steps number in the loop increases from one to four (Fig. 5.8). In the case of identical wires the magnetization reversal should take place in one jump, because the 'felt field' is the same for each element of the array. The limited number of simulated wires causes this discrepancy, but the calculations purpose is only to approximate the ideal case. On the other hand the simulations show how the antiparallel alignmet between nearest wires or group of wires is energetically favoured. Fig. 5.9 shows the demagnetizing field at the remanence and at the second plateau, evidencing, in this latter case, its decreasing in corrispondence to the antiparallel alignment of the magnetization of two near wires. A further investigation of the dipolar interaction among the wires can be

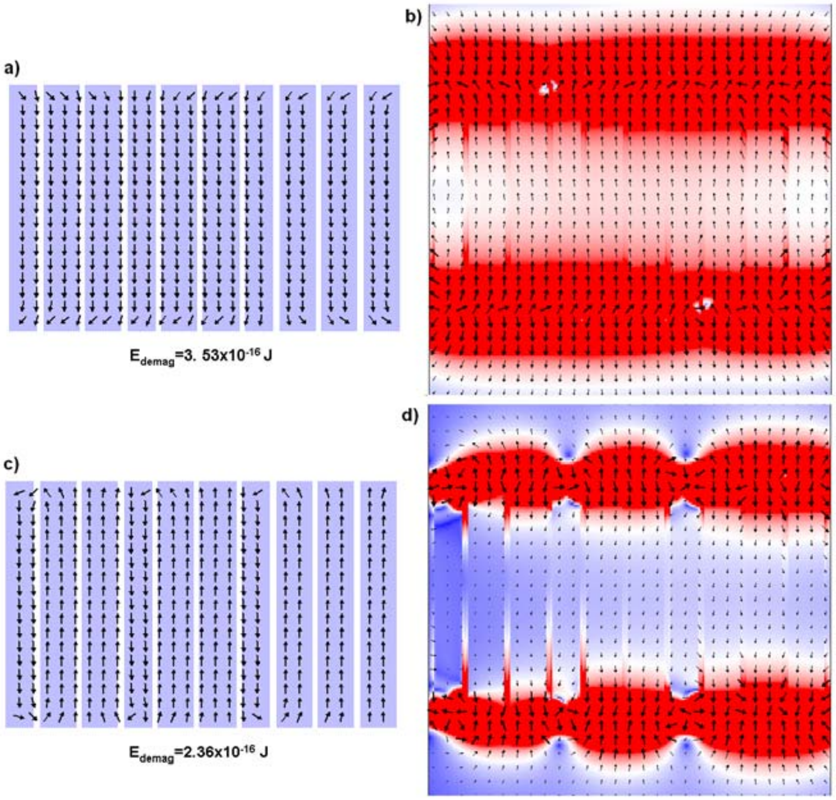

Figure 5.9: Magnetization configurations (a,c) and demagnetizing field configurations (b,d) of the simulated array with three modified wires, at remanence and in corrispondence of the second plateau, respectively. For both the configurations is indicated the relative calculated demagnetizing energy.

performed measuring the saturation field values H_s as a function of thickness t, applying the magnetic field H perpendicular to the wires length (hard axis). As explaned in the introduction section, in both the cases of absence of dipolar interaction and interacting wires the saturation field H_s results proportional to thickness if the length and width are fixed [91]. In the investigated samples

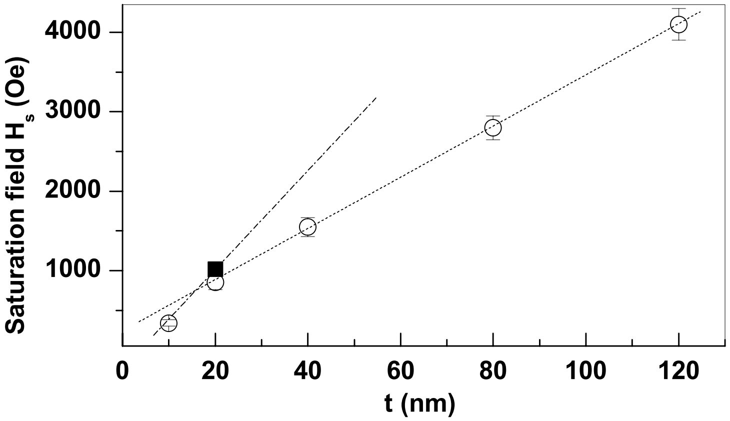

Figure 5.10: Hard axis saturation field H_s vs. wires thickness t. The square full point is taken from Ref. [90]. The lines are a guide to the eye.

this linear behaviour of the saturation field H_s as function of the thickness t is confirmed if the $10nm$-tick sample is exclused (Fig. 5.10). The point at thickness $10nm$ singles out an increase in slope and might indicate that dipolar interaction is effective only for $t \geq 20nm$ as it is confirmed by the position of the point at $20nm$ for non-interacting wires (taken from Ref. [90]) and by the single Barkhausen jump in the μ-MOKE loop of this $10nm$-thick sample.

5.4.3 Conclusions

The vectorial hysteresis loops (in-plane magnetization components parallel and perpendicular to the applied field) recorded with the external field applied perpendicular to the length of wires (hard magnetization direction), show a transition from coherent rotation to inhomogeneous reversal mode for wires thickness above $80nm$. The effects of dipolar interactions are evidenced by the variation of the saturation field in the hard-axis hysteresis loops as a function of wires thickness. In detail, the analysis of the saturation field vs. wires thickness shows that the dipolar interactions start to play a role for wires thickness $\geq 20nm$.

Chapter 6

Magnetostatic dipolar domain wall pinning in Py triangular microrings

This chapter deals with the magnetostatic dipolar domain wall pinning in Py triangular microrings. It is organized following a similar outline of the previous chapter, starting with an overview of the problem and focusing then on the specific investigated case. The complexity introduced by the employment of more experimental techniques has required a section dedicated to detail the experimental setup.

6.1 The sample

6.1.1 Ferromagnetic rings: an interesting geometry

Magnetic nanorings have been intensively studied because of their outstanding magnetic properties that make them good candidates for a wide opportunity of applications from the magnetic random access memory (MRAM) systems [96] to the magnetoresistance sensors [97]. In this field the purpose continues being to find the geometries and materials that provide the simplest, fasts and reproducible switching mechanism, through stable and controllable magnetic states. However the magnetic nanorings have shown interesting aspects for the investigation of fundamental physical questions, as the pinning and structure of domain walls at notches [98, 99], magnetoresistance effects in the domain walls and quantum transport properties as the Aharonov-Bohm oscillations [100]. The study of control the domain wall motion using the magnetostatic interaction has recently received considerable attention as possible application to the so called 'magnetic domain-wall logic' [101].

The first step in the investigation of structures with a new geometry is to consider which magnetic states are permitted and if they are stable [102]. In the case of ring shape, the magnetization tends to be aligned parallel to the branches of the ring or circumference (for circular shaped ring) to minimize the stray field, leading even to the formation of flux-closure vortex states. Differently from discs, where the highly energetic vortex core is pointing out of the film plane, in the rings the core was completely removed making the vortex state very stable. At saturation the magnetization is forced to be aligned to the external field and the ring is also in a single-domain state, but as the field is reduced the magnetization follows the geometry of the object and forms domain walls where two possible kind of polarity in the opposite magnetization directions meeting can be defined: head-to-head or tail-to-tail domain walls. Magnetic measurements and micromagnetic simulations have indicated the existence of two different stable bi-domain states, called onion states, corresponding to opposite circulation of the magnetization in each half of the ring [103].

The theoretical prediction of the possible stable states is based on the energy contributions from exchange, anisotropy and stray field. Local minima in the total energy correspond to accessible stable or metastable states of the system. It is obvious that the stray field energy term will favour the vortex state, but the energy balance from each contribution shows how the magnetization reversal process of different magnetic systems takes place through different configurations, e.g., in the presence of a magnetocrystalline anisotropy the vortex state can no longer exist in submicron Co rings [104].

Neglecting the magnetocrystalline anisotropy, only the geometry determines the microscopic spin structure of the magnetic states. The second step in the investigation of differently shaped rings then consists in the study of the transitions between the various stable and metastable configurations of the magnetization. Starting from a basic case, the perfectly symmetrical rings, only one transition from one onion to the reverse onion states takes place in the magnetization reversal, without going into the vortex state [103]. The main problem associated with symmetrical ring is the difficulty in pinning the magnetic domain walls in determined places. Without pinning, both magnetic poles of the onion state start to rotate simultaneously and in the same rotational direction, the reversed onion state is then reached when the two domain walls have reached the opposite side [102]. The system changes completely its behaviour if an asymmetry is introduced in the object. Rings with both variable width and presence of notches [105] show a switching mechanism from onion to vortex state consisting in the displacement of one of the head to head or tail to tail domain wall as far as the annihilation with the opposite wall and then a vortex to onion transition by nucleation and propagation of magnetic domain in the half of the ring which is magnetized anti-parallel to the direction of the applied magnetic field. Similar pinning effects have been also observed at the corners of structures geometrically asymmetric such as triangular rings micromagnets [106], with the advantage that such magnetic configurations are markedly insensitive to shape fluctuations and edge roughness. In earlier works it has come out how the head-to head domain walls can be positioned at selected corners and moved between corners by applying a field along a particular direction and how these structures enable the intentional design of clockwise and counter-clockwise magnetic vortex groundstates [107].

6.1.2 Sample description

The samples presented in this chapter are arrays of equilateral triangular rings of nominal side $2\mu m$, width $250nm$ and thickness $25nm$, fabricated using e-beam lithography and lift-off technique, employed by the Department of Electrical and Computer Engineering of University of Illinois at Chigago and by the Cornell

Nanofabrication Facility and Department of Applied and Engineering Physics of the Cornell University, Ithaca, New York.. The study is a combined of magneto-optical (L-MOKE and D-MOKE) and imaging (MFM) techniques, supported by a numerical simulations work (OOMMF). The samples can be divided in two different groups: isolated and interacting triangular rings. In the former the elements are arranged in an array with a slightly rectangular symmetry with a period of $\approx 4.2\mu m$ and of $\approx 4.6\mu m$ along the vertical and horizontal direction, respectively (Fig.6.1).

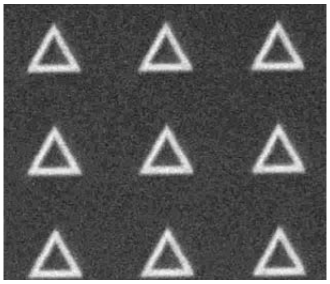

Figure 6.1: SEM image of the array of isolated Py triangular rings. The width of the pitcure is about $12\mu m^2$.

The interacting rings are instead arranged in vertical and horizontal chains as shown in Fig.6.2. In the vertical chains the apex of each triangle is in proximity to the edge centre of the triangle above it while in the horizontal chains the proximity is between the adjacent corners of the triangles. Both interacting samples have an inter-element spacing of $50nm$ along the proximity direction and the same spacing of the isolated rings along the non-interacting direction. The reversal mechanism is substantially the same for the three samples, as will explaned further in detail. The magnetization passes through two onion states via the formation of an intermediate vortex state. However the combined experimental and numerical study has permitted to determine the field dependence of the spin structure in the rings for each investigated array and to determine the related effects of the dipolar interaction on the pinning of the domain walls into the geometrical structure of the triangular rings.

In the case of horizontal chains the dipolar interaction affects the field range

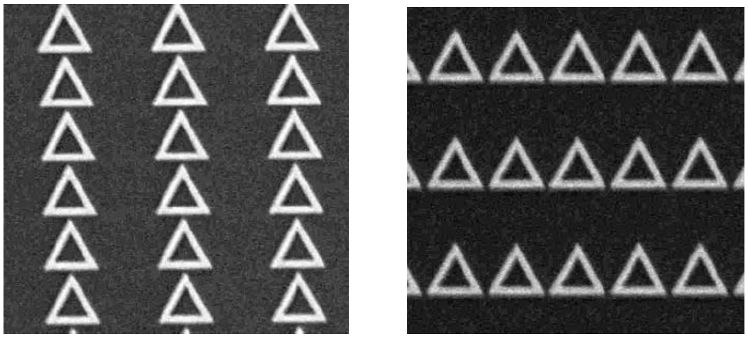

Figure 6.2: SEM image of the array of vertical chains (on the left side) and horizontal chains (on the right side) Py triangular rings. The width of the pitcure is about $12\mu m^2$.

in which the triangles are in the vortex state.

In the case of vertical chains an additional intermediate state is observed during reversal. The new state involves a domain wall pinned at the center of the edge that is in close proximity to the apex of its neighbor. In this last case the domain wall motion can be modelled by a triple potential well and because the mechanism of pinning-depinning of the domain wall is related to the geometry of the interacting elements, the study can be viewed as a very elementary form of magnetic logic.

6.2 Experimental details of the employed techniques

6.2.1 Diffracted magneto-optic Kerr effect

For the simple transverse D-MOKE measurements, an incident beam of a red-diode laser (wavelength 633nm) is polarized in the plane of incidence and the magnetic field is applied perpendicular to the plane of incidence. In order to reduce the noise in the measurements, the laser intensity I is modulated with a sine wave at 1.190 Hz and a lock-in amplifier is used to detect I.

However the measurements presented in the section dedicated to the experimental results employ two different types of MOKE measurements carried out simultaneously. The external field was applied in the sample plane (xyplane) using a quadrupolar electromagnet that allows to apply simultaneously two mutually orthogonal fields: a vertical magnetic field H_y perpendicular to the incidence plane and a horizontal magnetic field H_x parallel to both the incidence and sample plane. In this way it is possible to monitor the magnetization reversal and the domain wall displacement combining the diffracted magneto-optic Kerr effect for a determined nth order diffracted beam and the longitudinal Kerr effect (L-MOKE) for the reflected beam. The measurements related to this latter was carried out as was already described in the chapter dedicated to the classical Kerr effect, i.e. modulating the reflected beam by a photoelastic modulator (PEM) operating at $50Hz$ and detecting the signal using a lock-in amplifier locked either at 50 or 100 kHz for obtaining Kerr ellipticity or rotation, respectively. With such experimental configuration it results possible to probe the magnetization components parallel and perpendicular to the applied field as well for D-MOKE as well L-MOKE.

6.2.2 Magnetic force microscopy

The used MFM system is not equipped for recording images applying an external field on the sample, so that the measurements are performed preparing the samples in various metastable states, choosing the field value from the D-MOKE loops and quenching it to zero field.

In the collected pictures a white spot indicates a repulsive interaction between the sample and the MFM tip, thus, it corresponds to a head-to-head domain wall. In the same way, a black point indicates an attractive interaction, corresponding to a tail-to-tail domain wall. In the presence of a vortex state the MFM image does not detect any spot on the triangular ring, because the closed magnetization flux determines only a slight leak in the corner due to the change in sign of the magnetization divergence between two continuous adjacent branches. The resolution of the used microscopy does not allow to value these properties, but it was observed in the previous work on isolated triangular rings [106].

6.3 The micromagnetic simulations

The field dependence of the spin structure in the rings as well as the magnetic form factors are evaluated calculating the magnetization distribution inside the particle at each applied field, using the micromagnetic OOMMF code [95]. In the case of the chains of triangles it is used a version of OOMMF modified in order to allow for periodic boundary conditions (PBCs) along the chain direction [108]. This update enabled to simulate a chain of interacting rings while actually considering a single ring in the simulations.

The material parameters are those contained in the OOMMF program for Py, i.e. saturation magnetization $M_s = 800 \times 10^3 A/m$ and exchange stiffness constant $A = 1.3 \times 10^{-11} J/m^3$. The material has been considered lacking in magnetocrystalline anisotropy and the damping coefficient used in the simulation is equal to 0.5. The used cell is a cube of $8.5nm$ side, which is slightly larger than the exchange length ($l_{ex} = \sqrt{(2A/\mu_0 M_s^2)}$), but necessary due to limited computational resources. In a few cases the results have been checked using a smaller cell of $5nm$ side to confirm the simulations validity.

For the D-MOKE loops, the zeroth-order, which corresponds to the average magnetization is provided directly by OOMMF program. The higher order diffraction loops require extracting the magnetization distribution from OOMMF and performing the integration for the magnetic form factor (Eq.4.4). When the magnetic form factor $f_d^m(n)$ is calculated, the hysteresis loops are valuated with Eq.4.5 using $A(n)$ as an adjustable parameter.

6.4 Previous studies on isolated Py triangular rings

Combining the diffracted magneto-optic Kerr effect, MFM imaging and numerical simulations the previous work [106] demonstrated how the magnetization reversal in isolated Py triangular rings takes place through a three-step switching process as the external field is swept along both any of the ring edges and edge normal. The results are summarized in Fig.6.3 and Fig.6.4. In the case of

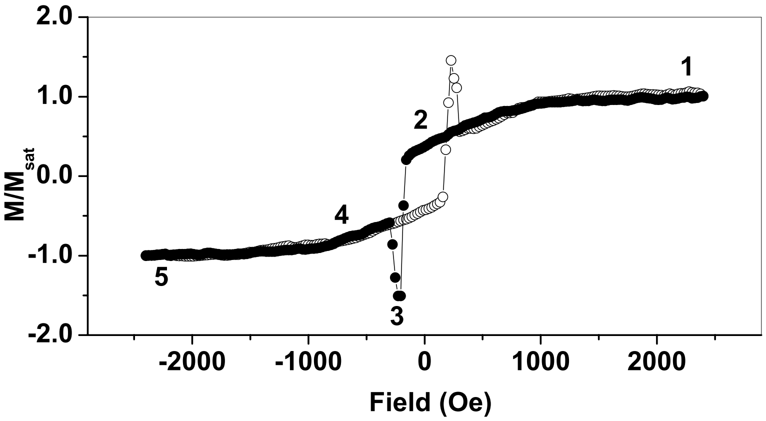

Figure 6.3: Second order diffracted MOKE hysteresis loop from the array of isolated rings with the external field perpendicular to an edge. The sketch below the loop shows the magnetic configurations that are reached during reversal.

H along the corner bisector (6.3), the diffracted hysteresis loop can be described as following: at the saturation (state 1) all three sides of the ring are aligned along the field direction. As the external field is reduced, shape anisotropy aligns the magnetization parallel to each branch of the ring and leads, at remanence, to an asymmetric onion state (state 2). At this point it is important to stress that the state 2 is determined by the magnetization direction of the horizontal branch of the ring and results from the assumption that H will never be perfectly aligned along bisector. In the simulations reported in this work, it is considered this aspect and a tilt of few degrees in the external magnetic field is introduced to reproduce the experimental condition. As H is reduced further (it has now a opposite sign) one of the lateral branches of the asymmetric onion state switches before the other one leading to a vortex state with the magnetization circulating counter-clockwise (state 3). As it is already explained, the magnetostatic and exchange energies bring to this configuration of continuous magnetization profile at the corners of the ring, getting rid of the high energy head-to-head and tail-to-tail domain walls. At a slightly lower H, also the other lateral branch switches leading to an asymmetric onion state (state 4) having the mirror asymmetry respect to the previous onion state (compare state 2 and state 4). At high negative fields, all three sides of the ring align again along the field direction (state 5). Differently from the ideal rings with other shape [107, 109], the vortex state takes place in triangular rings thanks to the asymmetric switching of the lateral branches and the assumption of any deviation of the shape from ideal case due to the fabrication process is not requested.

When the external field H is applied along one of the edges (Fig.6.4), the magnetization reversal process follows similar steps of the previous case: from the saturation (state 1), through a asymmetric onion state forced by shape anisotropy at the remanence(state 2), then a vortex with a well defined circulation of the magnetization (state 3) and the appearance of a reversed asymmetric onion state as H is further reduced (state4). Differently from the case with H applied along the bisector, the formation of this last onion state requires the switching of both lateral branches of the ring and its nucleation is also retarded. Finally, when H is high enough, the magnetization in the three branches aligns along the field direction (state 5). It is worth noticing that both the measurements and the simulations show how the tilt of the external field H from the ideal direction of the ring edge in either direction (clockwise and counterclockwise) does not modify the asymmetry of the onion state at remanence, differently from the previous case with H along the corner bisector.

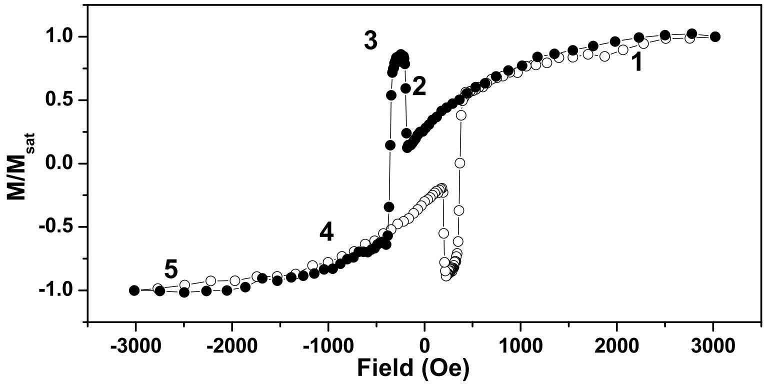

Figure 6.4: First order diffracted MOKE hysteresis loop from the array of isolated rings with the external field parallel to an edge. The sketch below the loop shows the magnetic configurations that are reached during reversal.

6.5 Experimental results

6.5.1 Magnetostatic dipolar domain wall pinning

Vertical chains

The D-MOKE loops measured from the sample of vertical chains of triangular rings, with the external field applied parallel to the chains direction(H_y in the chosen coordinate system) do not show appreciable differences with respect to those obtained from the just discussed isolated rings [110]. This means that the magnetization reversal of the rings arranged in vertical chains takes place via the same states as for the isolated rings, i.e. through an onion-vortex-onion transition. That being so, both the samples (isolated and vertical chains) were prepared in a defined onion state by applying a positive saturating field H_y and then reducing it to a well defined negative value after the complete cancellation of the vortex state (see Fig.6.5). This value of field has been selected by monitoring in real time the diffracted loop. The onion state obtained for each ring of the samples shows a head-to-head domain wall pinned at the bottom-right corner of the triangle and another tail-to-tail domain wall in the upper

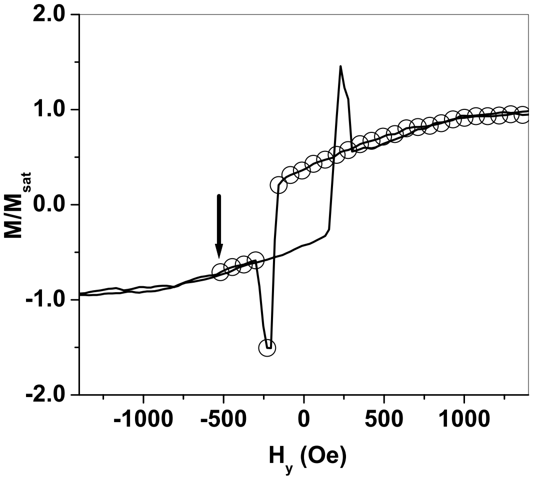

Figure 6.5: Second-order diffracted MOKE (full line) and minor (open dots) loops used to prepare the rings of the vertical chains in the same onion state.

corner. This magnetic state is stable at zero field, as shows the MFM image taken after the above process (Fig.6.6). Maintaining a certain constant value of H_y in such way to avoid the switching of the magnetization inside the lateral oblique branches of the triangles, the motion of the bottom-right domain wall is induced by means of a horizontal magnetic field H_x. This motion along the bottom edge of the ring is monitored by recording the L-MOKE loop, as a function of the strength of the final H_y field used to prepare the initial onion state. The H_x range values were chosen in order to complete the head-to-head domain wall motion from the right to the left vertex of the horizontal edge, but at the same time in order to avoid the magnetization switching inside the lateral branches of the ring.

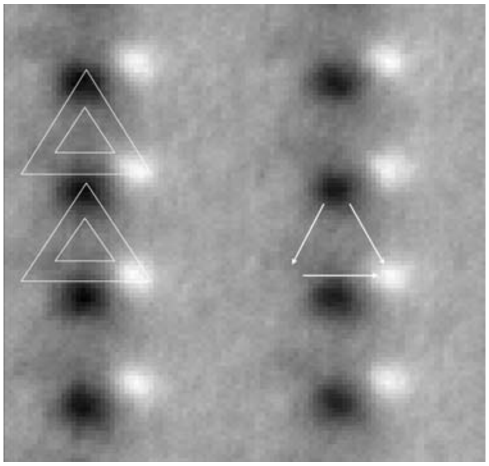

Figure 6.6: Zero-field MFM image of the vertical chains showing the head-to-head and tail-to-tail DW that are present in the onion state.

The effect of the dipolar interaction in the vertical chain becomes more evident by decreasing H_y, i.e. by increasing the absolute value of it.

At high values of the vertical field both the experimental and simulated data show a L-MOKE loop with a single transition for both the isolated and the vertical chains rings (Fig.6.7). The domain wall moves freely between the geometric pinning potential wells determined by adjacent corners as the external field H_x reaches a critical value: H_d and H_{d1} for the isolated and vertical chains sample, respectively. The lower value of H_{d1} respect to H_d is confirmed by the micromagnetic simulations and is due to the presence of the magnetostatic dipolar interaction between the rings in the chains as will be explained further through an additional potential well. At lower values of H_y, the measured and calculated L-MOKE loops show still a single transition for the isolated triangles, but in the case of interacting rings the loops show an intermediate step caused by the pinning of the wall at the center of the horizontal branch due to the dipolar field emanating from the corner of the nearest ring neighbor. The domain wall continues to be released from the right corner at $H_x = H_{d1}$ but when it arrives

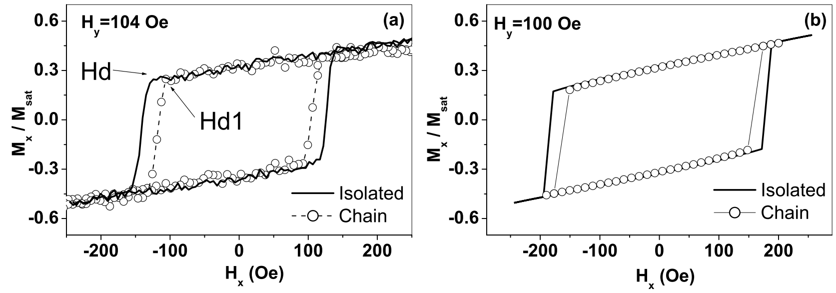

Figure 6.7: Measured (a) and simulated (b) hystresis loops for the domain wall motion from the right to the left vertex of the horizontal edge. Hd and $Hd1$ are the fields necessary to unpin the DW from the vertex in isolated and interacting triangles, respectively. H_y is the vertical field used to prepare the initial onion state.

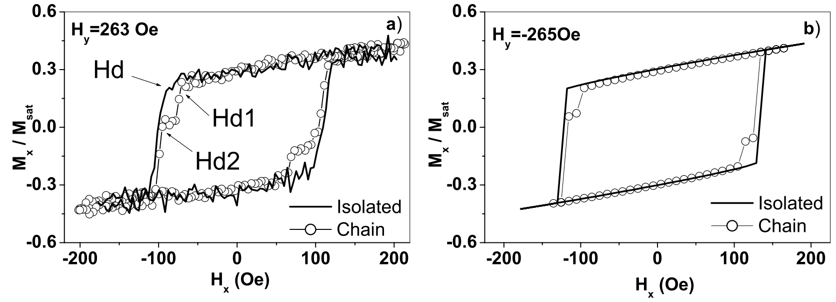

Figure 6.8: Measured (a) and simulated(b) hystresis loops for the domain wall motion from the right to the left vertex of the horizontal edge. Hd and $Hd1$ are the fields necessary to unpin the DW from the vertex in isolated and interacting triangles, respectively. $Hd2$ is the field necessary to unpin the DW from the potential well at the center of the base created by neighboring ring. H_y is the vertical field used to prepare the initial onion state.

at the center of the edge it is pinned by the dipolar interaction and manages to rid only when H_x reaches a second value H_{d2}, moving toward the left corner.

Measuring the L-MOKE loops as function of the absolute value of the preparation field H_y in a range of $50 - 450 Oe$, it is noticed that the values of the depinning field from the right corner H_d and H_{d1}, are significantly affected by H_y, whereas the depinning field from the potential well created by the magnetostatic interaction is almost constant(Fig.6.9). For higher values of $|H_y|$ both

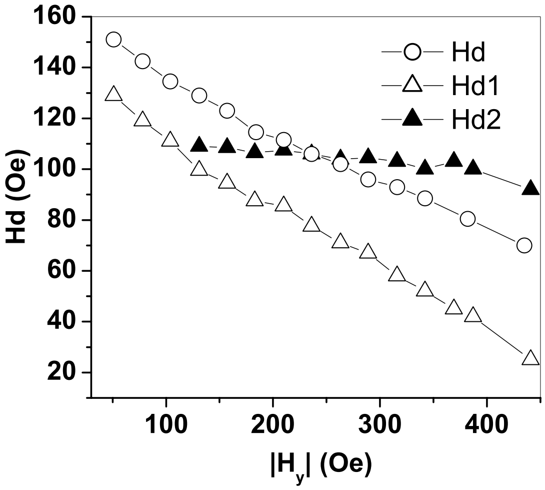

Figure 6.9: Evolution of Hd, $Hd1$, and $Hd2$ as a function of the field strength (absolute value) along y, (H_y).

H_{d1} and H_{d2} are affected by the preparation field H_y, since the domain wall begin to change its spatial configuration.

In the $|H_y|$ range up to $450 Oe$ the process for the vertical chains can be modelled as a domain wall in a triple potential well landscape that evolves as a function of the vertical field H_y as it is sketched in Fig.6.10. Not considering the effect of H_x on this potential landscape model, the behaviour can be summarized as follows: the vertical field H_y modifies the energy landscape through which the domain wall has to move toward the left corner, from the right one. It makes this by progressively twisting toward the y-direction the spins in the horizontal branch. If H_y is small the spins are nearly horizontal and the displacement of the domain wall costs more energy then in the case in which the spins are

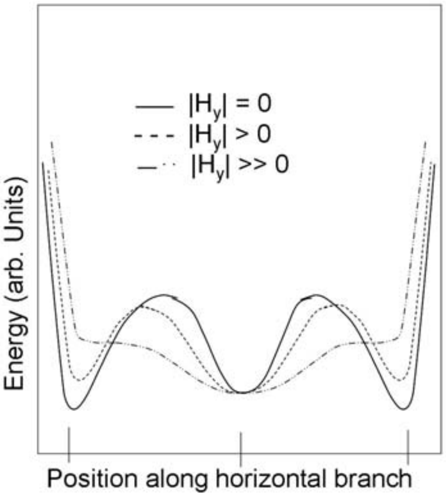

Figure 6.10: Schematic of the triple potential well and its evolution with H_y. The two side wells are a geometric effect of the vertices; the central well is caused by the neighboring ring.

twisted toward the y-direction, the domain wall can then move easily along the ring segment. The effect of increasing $|H_y|$ can be considered as a progressive reduction of the energy barrier separating the two external potential wells, i.e. related to the two corners of the horizontal edge. For small $|H_y|$ the value of H_x required to unpin the domain wall from the right corner is also sufficient to draw it across the entire horizontal segment and a single transition is observed in the L-MOKE loop. As $|H_y|$ increased above a certain threshold, the value of the horizontal field H_{d1} required to de-pin the domain wall from the right corner is lower than the value of H_{d2} needed to unpin it from the central well, so that once the wall has reached the mid point of the horizontal segment it is blocked until H_x reaches the value H_{d2}. This results in the observation of two transitions in the L-MOKE loop.

The field H_y affects also the isolated triangles, as demonstrated by the reduction of H_d increasing of $|H_y|$, but the energy landscape is now a only two potential wells model due to geometrical pinning sites at the corners of the triangle.

Based on this triple potential well model, there should be a value of H_y

at which the domain wall moves to the centre of the horizontal segment even if H_x has not yet changed sign. This indeed is observed experimentally and in the simulated data, as shown in Fig.6.11. To investigate if the state with the domain wall pinned at the mid point of the horizontal edge is stable like the starting onion state, it was measured the minor L-MOKE loop shown in Fig.6.12. Selecting a H_y value for which it was observed a two transitions loop, the field H_x is reduced to zero from the saturation, in order to moving the domain wall as far as the centre of the horizontal segment, stopping before that

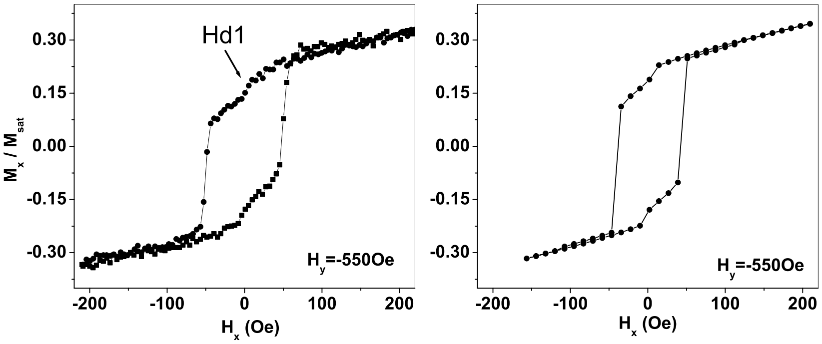

Figure 6.11: Measured and simulated L-MOKE loops for $H_y = -550Oe$ and for the vertical chains.

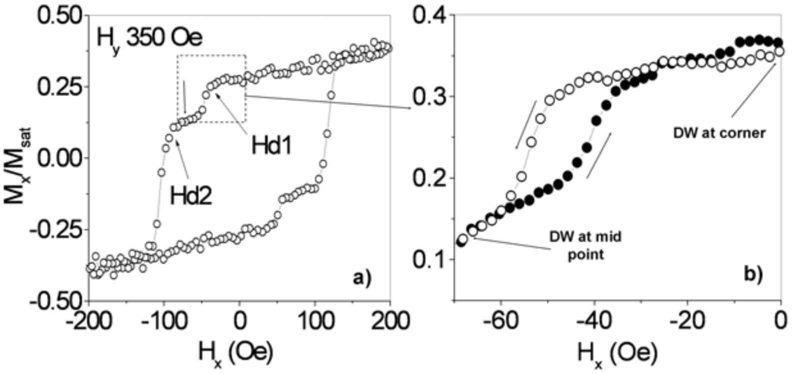

Figure 6.12: (a) Full and (b) minor longitudinal MOKE loops for $H_y = -350Oe$ and for the vertical chains. The minor loop shows the reversibility of the DW motion.

the domain wall goes to the left corner. It is observed that the signal returns to its starting value, closing the minor hysteresis loop, i.e. the domain wall moves back to initial right corner as the H_x is removed. It is important to note that the small horizontal field component introduced by the tilt of vertical field H_y is selected in order to favour the domain wall motion toward the left corner, thus, this comeback to initial position does not depend on this geometrical orientation between the external vertical field and the horizontal edge of rings.

A closer look at the details of the simulated magnetization configurations in the horizontal segment during the wall displacement evidences an additional effect neglected up to now. In particular, when the domain wall is pinned at the center of the bottom edge, the spins configurations inside result asymmetric with respect to the wall position, for different value of H_y (Fig.6.13). On the left-hand side the magnetization vectors are aligned along the same direction and pointing against the domain wall, while on the right side the spin distribution forms a so called 'C' configuration. This asymmetry in the spins configuration gives rise to a kind of pressure, that can be defined as 'exchange' pressure P, which acts against the wall and is opposite to the external field H_x. When this last one is removed, the domain wall is pushed back to its original position by the 'exchange' pressure and the onion state with the domain wall pinned at the center of the segment results to be unstable. It is worth noticing that this asymmetric configuration is the reason of the different drop in magnetization at the first and second jump, evident in both the measured and calculated L-

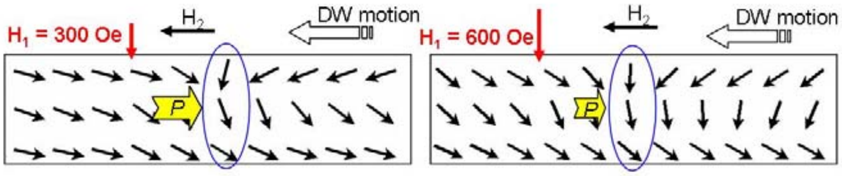

Figure 6.13: Schematic of the spin distribution in the horizontal edge of an interacting ring for two different values of H_y, when the domain wall is pinned at the center. The big arrow with the label 'P' indicates the exchange pressure determined by the asymmetric spin distribution at the two sides of the DW.

MOKE loops (see also Fig.6.8).

Horizontal chains

In the case of horizontal chains, the dipolar interaction effects become appreciable when the external field is applied parallel to the chains direction. As the sample with vertical chains, also this sample shows the same magnetization reversal mechanism of isolated rings. However the first onion state (state2 of Fig.6.4) presents an alternated head-to-head and tail-to-tail domain walls very close each other at the corners of adjacent rings along the chain and a strong dipolar stabilizing interaction between neighbouring triangles is then expected (Fig. 6.14). Considering again the first order D-MOKE loops measured from the isolated and horizontal chains of rings, it is possible to focus the attention on the mesa-like peak (state3 of Fig.6.4) corresponding to the formation of the intermediate vortex state occurring during the magnetization reversal process. An expanded view of it shows how the peak observed in the D-MOKE loop from the horizontal chains is significantly narrower than that measured on the isolated rings. (Fig.6.15). The figure shows also a different intensity of the two peaks, but it depends on the slightly different periods of the two arrays along

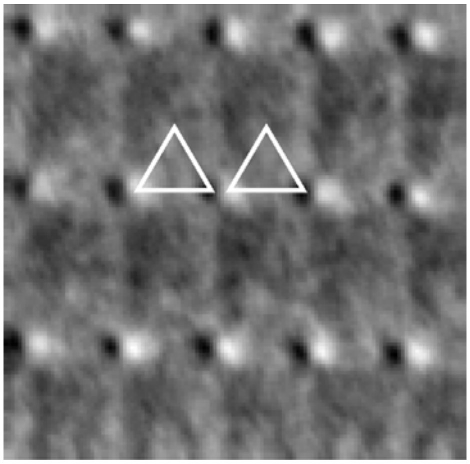

Figure 6.14: MFM image of the orizontal chains prepared in the first onion state (state2 of Fig.6.4). The size of the image is about $10 \times 10 \mu m^2$.

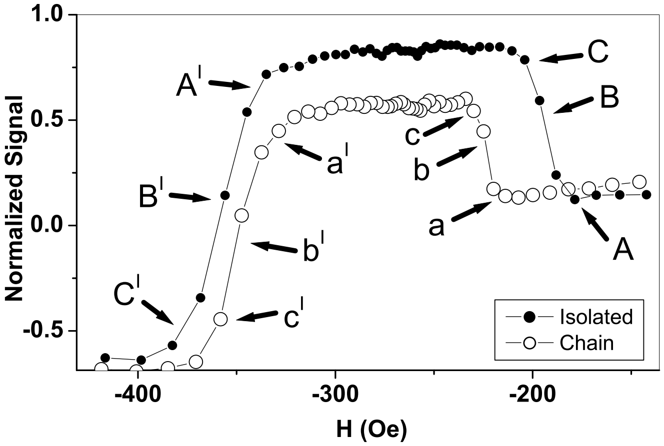

Figure 6.15: Enlargement of one of the peaks in the first-order diffracted MOKE hysteresis loops for isolated rings (full dots) and horizontal chains (open dots) corresponding to the formation of the vortex state. The figure shows how the rings interaction changes the vortex nucleation field in the case of horizontal chains.

the y direction, considering that it results in different values of the parameter $A(n)$ introduced in Eq. 4.5.

The narrowness of the peak indicates that the dipolar interaction reduces the field range in which the intermediate vortex state exists by about $35Oe$. The reduction is due mainly to a delayed nucleation of the vortex configuration, as confirmed by the micromagnetic simulations. This delayed nucleation can be understood considering that the attractive character of the dipolar interaction between the domain walls in the chains increases the stability of the onion state preceding the formation of the vortex. Fig. 6.15 shows also a slightly anticipated annihilation of the vortex state but the effect is small and could be caused by a slightly different distribution of the vortex annihilation fields in the two samples. It could be released to fabrication defects, such as deviation from the ideal shape or edge roughness or material inhomogeneities.

The transition from the onion to the vortex state is observed imaging, through MFM measurements, the distribution of these two different magnetic configurations in the isolated and horizontal chains of rings by reducing to zero the external field after having reached different points on the D-MOKE loop.

From Fig. 6.16 it is clear how the transition from the onion to the vortex state occurs in the horizontal chains as a 'domino effect'. The attractive dipolar energy stabilizes the onion state well below the intrinsic nucleation field so that as one ring switches to the vortex configuration the two nearest neighbor rings become unstable and switch as well to the vortex state and so on in a sort of cascade process that might lead to the switch of an entire chain. The effect is more evident if it is compared with the same transition in the isolated triangles sample (Fig.6.17). In this last case the dipolar interaction is always negligible so that the intrinsic nucleation field distribution governs the transition and the nucleation of the vortex occurs at random positions in the sample.

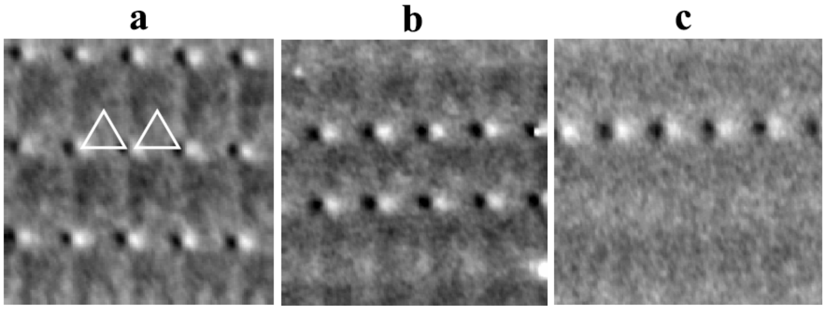

Figure 6.16: MFM images corresponding to points labeled *a*, *b*, *c* in Fig.6.15. The figure shows the correlated nucleation of the vortex state in the horizontal chains. The size of the image is about $10 \times 10\mu m^2$.

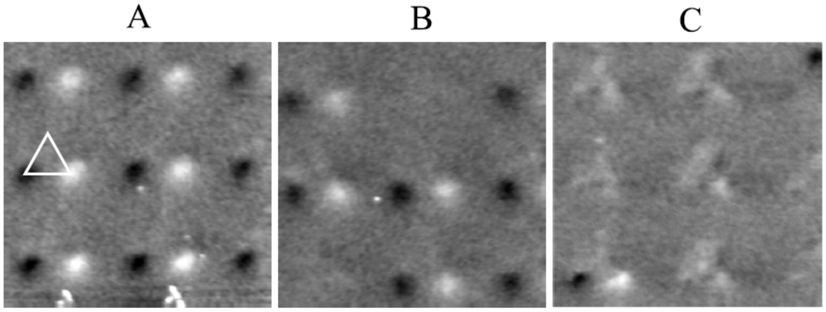

Figure 6.17: MFM images corresponding to points labeled *A*, *B*, *C* in Fig.6.15. The figure shows the uncorrelated nature of the vortex state in the isolated rings. The size of the image is about $10 \times 10\mu m^2$.

It is also interesting to observe the annihilation of vortex configuration, i.e.

the transition from the vortex to the second onion state. As it is expected, the annihilation of the vortex does not show significant differences for the horizontal chains and isolated rings samples (Fig. 6.18). The dipolar interaction between the vortex states is negligible in the horizontal chains as well as in the isolated triangles,thus, the annihilation process is still determined by the intrinsic properties of each ring in the sample, i.e. ring geometry and fabrication defects.

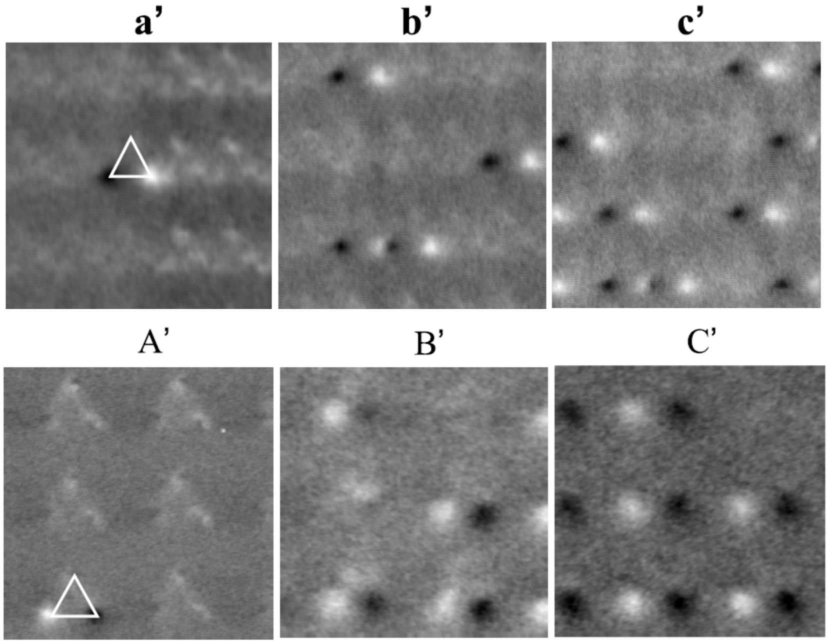

Figure 6.18: MFM images corresponding to points labeled a', b', c', A', B', C' in Fig.6.15. The figure shows that the annihilation of the vortex does not show significant differences for the horizontal chains and isolated rings. The size of the image is about $10 \times 10 \mu m^2$.

6.5.2 Conclusions

In both the interacting samples the magnetic dipole fields generated by the domain walls of the onion states are shown to affect the switching of their neighbors. In the vertical chains (head to base chains) the presence of a vertex close to the center of an edge can qualitatively change the manner in which reversal occurs by trapping the domain wall in the center of the base rather than at the vertices. Based on the above results, it is interesting to speculate that if one were to construct a triangular ring with two smaller triangular rings below its base, switching in the large ring might be tailored to depend on the magnetic state of both small rings. Such structures could lead to magnetic logic gates.

Chapter 7

Trilayered Py/Cu/Co nanodiscs: static and dynamical properties

The chapter is dedicated to the investigation of trilayered heterostructures, such as patterned arrays of pseudo spin-valves in which a layer of Py has been coupled with a layer of Co, through an interspacer of non-magnetic Cu. The outline is the same of the previous two experimental chapters, with an overview of the general problem and a section dedicated to detail the experimental setup. However, the section dedicated to the experimental results has been devided in two parts related to dipolar and exchange coupled patterned trilayers.

7.1 The sample

7.1.1 Systems of heterostructures F/NM/F

The 1986 is the date of the experimental demonstration that a short-range coupling takes place between the magnetizations of two ferromagnetic layers separated by a non-magnetic spacer layer (F/NM/F) [37, 111, 112]. Following discoveries, of that the GMR is one of the most important [2, 3], have grown interest in these coupling mechanisms and in particular in the simplest form of coupling: the bilinear ($E_c = -J\mathbf{m_i} \cdot \mathbf{m_{i+1}}$). As already explaned in the second chapter, positive values of J favor a parallel alignment of the magnetization of the two layers ($\mathbf{m_i}$ and $\mathbf{m_j}$), whereas negative values favor antiparallel alignment. These intensive studies led to the discovery of the oscillating behaviour of the J sign, varying the thickness of the spacer layer [1]. A such discovery opened the door to the investigation of this peculiarity on a large variety of systems, also including more complex form as the biquadratic coupling and quantum well states [113]. Systematic studies have been performed in structures which employ interlayers possessing simple Fermi surfaces, where the exchange coupling is significantly simplified. Elements, such as Cu, Ag and Au have approximately only one s-p electron per atom and can be grown epitaxially on Fe and Co. Since the first experiments that showed the cross-over from ferromagnetic to antiferromagnetic coupling, in b.c.c. Fe/Cu/Fe(001) [114] and f.c.c. Co/Cu/Co(001) [115], numerous measurements followed, showing the long-range oscillatory period of the exchange coupling in both f.c.c. and b.c.c. Cu, as well in epitaxially grown as well in sputtered structures [40, 116, 117, 118]. Successively the study of role of interlayer crystallographic orientation showed how the interface roughness can play a relevant role in the exchange coupling behaviour and several theoretical models have been proposed to take into account imperfect interfaces [34, 119]. This is a very strong effect as demonstrated by studies in which the pinholes presence leads to a relevant (50%) increase of the remanent magnetization [36].

Sputtered Co/Cu/Co and Fe/Cu/Fe multilayers have shown oscillations of the interlayer coupling with substantially the same long period (about $10 - 12.5\AA$) but in opposite phase for the two different materials and with an eximated interlayer coupling constant J around $0.15erg/cm^2$ [39], $0.095erg/cm^2$ [40] and $0.3erg/cm^2$ [120].

The multilayered stacks are more complex systems respect to the continuos multilayered films but at the same time their interplay between the exchange interlayer coupling and the dipolar coupling can introduce further possibilities for manipulating the magnetic behaviour with a strong potential for future applications.

Magnetization reversal in similar Py/Cu/Py patterns has been investigated

[121, 122], showing a intermediate state with antiparallel alignment of the two layers (nearly single domain states in [90] and vortex state in [122]).

The system Py/Cu/Co studied in this thesis, have added the effects of the different reversal nucleation fields and saturation magnetization values for the two layers of the single stack.

7.1.2 Sample description

The samples presented in this chapter are multilayered discs consisting of Py and Co ferromagnetic layers separated by a Cu non-magnetic spacer layer. These pseudo-spin valves are arranged in arrays with square symmetry on a $4 \times 4mm^2$ area and with a such edge-to-edge spacing to neglect the dipolar interaction between adjacent trilayer disc structures. In this way only the interaction between the Py and Co layers within a single pseudo-spin valve is considered. Continuous Py/Cu/Co trilayers have also been prepared and measured as reference films.

The selected fabrication technique is the deep ultraviolet lithography at $248nm$ exposing wavelength on $Si(001)$, employed by the Information Storage Materials Laboratory of the Department of Electrical and Computer Engineering of the National University of Singapore [86].

The samples can be divided in two different groups: dipolar and exchange coupled Py/Cu/Co nanodiscs. In the former the copper spacer thickness equal to $10nm$ makes dominant the dipolar interaction between the two ferromagnetic layers, whereas in the latter case the copper spacer thickness reduced to a range of $0.7 - 2.0nm$ makes dominant over the dipolar interaction an interlayer exchange coupling between the two layers of Py and Co.

The principal sample of the former group is an array of trilayered circular nanodiscs having diameter $d = 230nm$ and edge-to-edge spacing $s = 160nm$, as shown in Fig.7.1. The two ferromagnetic layers have a thickness equal to $10nm$, i.e. the scheme of the structure is $\mathrm{Py}_{(10nm)}/\mathrm{Cu}_{(10nm)}/\mathrm{Co}_{(10nm)}$. Successively other two samples of the same group have been investigated: trilayered circular

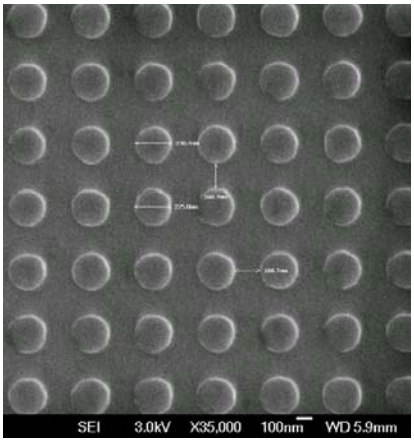

Figure 7.1: Scanning electron microscope (SEM) image of the array of circular Py/Cu/Co nanodiscs.

discs with the same diameter and edge-to-edge spacing but with the thickness of the Py and Co layers increased to $30nm$ and a trilayered sample with the same layering scheme of the principal one but with elliptical shape of the nanodiscs, i.e with a long axis of $205nm$, a short axis of $155nm$ and an edge-to-edge spacing of $130nm$ as shown in Fig.7.2. These two complementary samples have been studied in order to gain information about the role played by the thickness of the ferromagnetic layers and the element shape on the magnetization reversal process. Concerning the second group, with reduced Cu spacer thickness, the

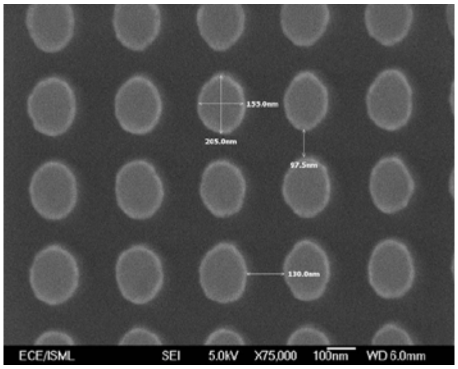

Figure 7.2: Scanning electron microscope (SEM) image of the array of elliptical Py/Cu/Co nanodiscs.

investigation has focused on a sample of $\text{Py}_{(10nm)}/\text{Cu}/\text{Co}_{(10nm)}$ circular discs with the same diameter and edge-to-edge-spacing of the principal sample, but with the Cu spacer thickness equal to $1nm$ in order to explore a new region of short-range interaction between the two ferromagnetic layers. In this case have also been studied other complementary samples with Cu spacer thickness equal to $0.7, 1.2$ and $2.0nm$ in order to clarify the origin of this short-range coupling between the two Py and Co layers.

7.2 Experimental details of the employed techniques

7.2.1 X-ray resonant magnetic scattering

The performed XRMS measurements have been carried out at the circularly polarized x-rays beamline (CiPo) at the Elettra synchrotron radiation facility [123], tuning the photon energy to the L_3 Fe and Co edges ($707eV$ and $777eV$, respectively) and working in the specular geometry. The principal reason for having choosen the XRMS technique is the possibility to obtain the separated

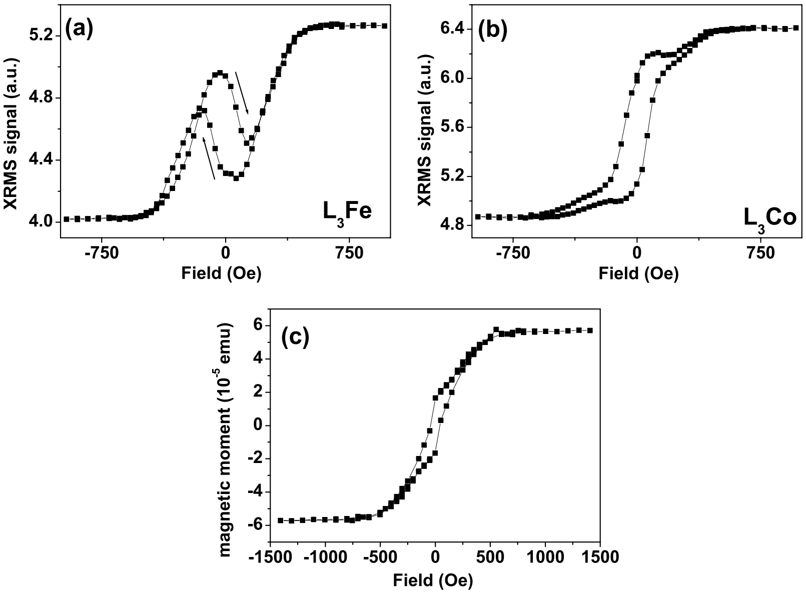

Figure 7.3: Hysteresis loops of circular $\text{Py}_{(10nm)}/\text{Cu}_{(10nm)}/\text{Co}_{(10nm)}$ nanodiscs measured with XRMS, at the Fe L_3 (a) and CoL_3 (b) thresholds and the hysteresis loop of the same sample measured with SQUID (superconducting quantum interference device) (c).

magnetic component of Py and Co layers along the x-direction, measuring the variation of the scattered intensity at the absorption edge of the selected element, while a magnetic field is applied. For system constituded by almost two ferromagnetic elements, the hysteresis loops measured with XRMS are completely different respect to the hysteresis loop of the total magnetization, as it will be observed in Fig. 7.3.

On the other hand, the instrument allows the setting of the incident and the scattering angles independently, in order to perform various types of scans. The so- called 'rocking scan' involves the only rotation of the sample (θ_S) holding the angle of detector θ_D constant. In this way the vector $\mathbf{q}$ is fixed during the scan and the Bragg condition is satisfied when the sample has a periodicity in the surface plane along the x-axis. The n-th order peak corresponds to the condition $q_x = 2n\pi/d$, with n positive or negative integer and d the order parameter in the x direction. Measuring the angle for the first Bragg peak and comparing the above relation of q_x with Eq.4.11, it is easy to find the periodicity of the sample structure:

$$d = \frac{\lambda}{2} \frac{1}{\sin(\theta)\sin(\Delta\theta)} \tag{7.1}$$

where $\theta = \theta_D/2$ and $\Delta\theta = \theta_S - \theta$.

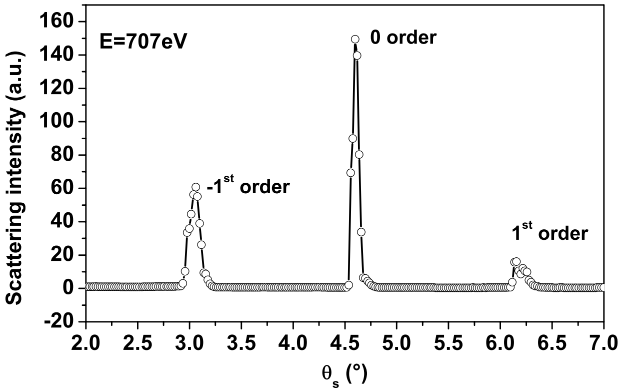

Figure 7.4: Rocking scan (diffused intensity versus θ_S at fixed $\theta_D = 9.2°$) for the sample of $\mathrm{Py}_{(10nm)}/\mathrm{Cu}_{(10nm)}/\mathrm{Co}_{(10nm)}$ circular dot. For the notation of the angles see the section about the XRMS in the chapter 4.

The periodicity of the array of trilayered circular nanodiscs has been verified through this kind of scan. As showed by Fig. 7.4, the angle for the first order Bragg peak is at about 1.5° from the angle of the specular peak, leading to a periodicity d of the sample structure equal to about $400nm$, in good agreement with the nominal $390nm$.

In specular reflectivity as well on a Bragg peak another kind of scan is possible, the energy scan, carried out in the range around the absorption edge of the selected element. This scan has the characteristic to probe the magnetic contribution of a selected element, in fact measuring the energy dependence in the specular reflectivity for two opposite values of the applied field H and calculating the difference, it can be evaluated which element has a maximum magnetic signal. For the Py the magnetic contribution of iron turned out higher

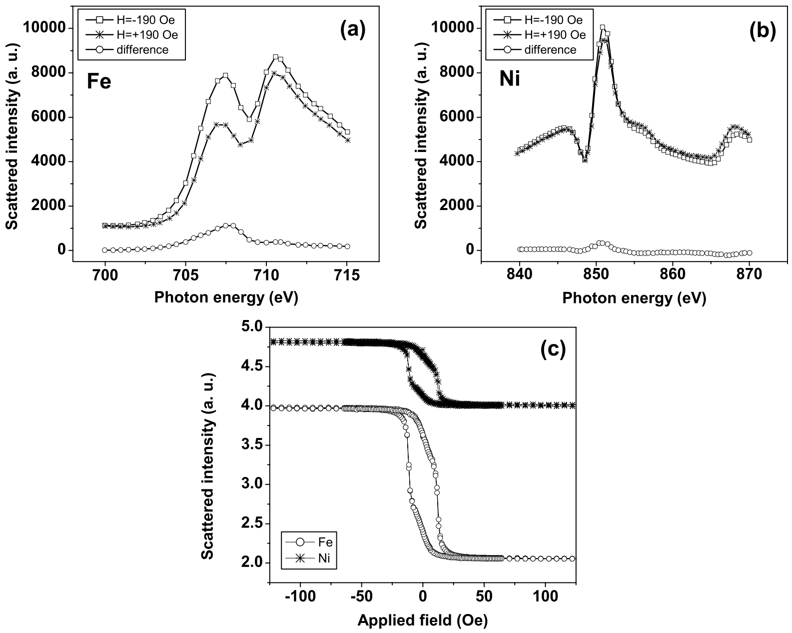

Figure 7.5: Energy scans in the range around the absorption edge of Fe (a) and Ni(b) for the reference film $\mathrm{Py}_{(10nm)}/\mathrm{Cu}_{(1nm)}/\mathrm{Co}_{(10nm)}$. The three curves are relative to the signal measured applying a magnetic field $H = -190Oe$ (square symbol), $H = +190Oe$ (star symbol) and calculating the difference of the two signals (circle symbol). The panel (c) is the XRMS hysteresis loops of the same sample measured at the Fe L_3 and NiL_3 thresholds.

than that of nickel, as shown the energy scans performed on the reference film $\mathrm{Py}_{(10nm)}/\mathrm{Cu}_{(1nm)}/\mathrm{Co}_{(10nm)}$ and as confirmed by the intensity of the signal in the measured magnetic loops of the same sample at the absorption edge of iron and nickel (Fig. 7.5). This is the reason that has brought to work at the iron absorption edge instead of nickel edge. In the shown measurements in this chapter it will be so common to refer to iron when the Py layer behaviour is described. Finally, the instrument allows to performe the '$\theta - 2\theta$ scan', where both the θ_D and θ_S are scanned, with the condition $\theta_S = \theta_D/2$. In this way the vertical modulation of the system is probed, detecting peaks originated from the constructive interference of the scattered radiation by the different layers constituting the sample.

7.2.2 The Brillouin light scattering

The BLS measurements have been carried out at the Group of High Resolution Optical Spectroscopy and Related Techniques (GHOST) laboratory (University of Perugia). A beam of about 200mW of monochromatic p-polarized light from a solid state laser operating at $\lambda = 532nm$ is focused on the samples surface using a camera objective. The scattered light is sent through a crossed analyzer to suppress the background of elastically scattered component and the surface phonon signal. Finally the scattered light is collected and frequency analyzed using a (3+3)-pass tandem Fabry-Perot interferometer and a photomultiplier tube. The sample is placed between the poles of an electromagnet with the external magnetic field applied perpendicular to the scattering plane and parallel to the film surface. With a such system to explore the spin-wave dependence is possible as a function of both the incident light angle and the in-plane angle of the applied field H.

7.3 The micromagnetic simulations

7.3.1 Static simulations

The simulations have been performed by using the OOMMF package [95]. The discs are discretized into cells of $5 \times 5 \times 10nm^3$ and the saturation magnetization values used for Py and Co are: $M_s = 800 \times 10^3 Am^{-1}$ and $M_s = 1200 \times 10^3 Am^{-1}$, respectively. The exchange stiffness constant A is fixed to $10 \times 10^{-12} Jm^{-1}$ for the Py and to $21 \times 10^{-12} Jm^{-1}$ for the Co. These magnetic parameters were derived from the BLS investigation of the continuous $\mathrm{Py}_{(10nm)}/\mathrm{Cu}_{(10nm)}/\mathrm{Co}_{(10nm)}$ reference sample. The magnetocrystalline anisotropy is neglected as well as the dipolar interaction between adjacent trilayer disc structures of the pattern. The only interactions in play are those between Py-layer and Co-layer inside the single nanopillar element of the array.

To simulate the sample with $1nm$-thick Cu spacer, a bilinear ferromagnetic coupling term J equal to $0.16 ergcm^{-2}$ is added in the OOMMF-code, holding unchanged the geometry of the unit cell and the magnetic parameter of the two ferromagnetic elements. For the other samples with reduced Cu spacer thickness, only the $2nm$-thick Cu sample has been simulated, because the smaller thickness values of the other spacers of copper require a very long calculation time due to the necessity of a much smaller cell height. In this case the discs have been descretized into cells of $5 \times 5 \times 2nm^3$ and the coupling constant J has been fixed to $0.25 ergcm^{-2}$.

The OOMMF code has been modified in order to provide as output both the total magnetic moment of the single pseudo-spin valve of the array as well as the magnetic moment of the two Py and Co layers, separately. In this way such simulated loops can be compared with the magnetic information obtained from the element sensitive XRMS technique.

7.3.2 Dynamic simulations

Also the 3D micromagnetic modelling for the dynamic behaviour has been carried out by using the OOMMF package. The geometrical parameters of the simulated cells are the same used for the static ones as well as the saturation magnetization and exchange stiffness constant values of the two ferromagnetic materials. Starting with a static initial state of the multilayer in which an in-plane applied field has a fixed value in the time and space, the system is excited by an out-of-plane (z-axis) Gaussian magnetic field pulse with a full width at half maximum of $1ps$ and an amplitude of $10Oe$. The pulse is applied at the center of the disk and has a circular shape with radius equal to $200nm$. At this point the system is left free to evolve following the Landau-Lifshitz-Gilbert equation with a damping factor set to $\alpha = 0.005$ and an effective gyromagnetic ratio $\gamma = 2.25 \times 10^5 m/As$. The dynamic evolution of the magnetization is tracked by saving the three components of the magnetization $\mathbf{m}(\mathbf{r_i}, t_i)$ at uniform time steps of $5ps$, starting the acquisition next $2ns$ from the pulse. A local Fourier transform in each single cell of each layer allows to calculate the local power spectra $S_z(\mathbf{r_i}, \omega)$, that, summed over i, returns the average power spectrum $\overline{S}_z(\omega)$ [124]. Plotting $\overline{S}_z(\omega)$ several peaks can be observed, both for the Py and Co discs. The peaks correspond to the eigenfrequencies for the oscillating m_z component, which gives the main contribution to the BLS cross section [125]. Finally a surface plot of $S_z(\mathbf{r_i}, \omega)$ for each eigenfrequency provides the spatial profile of the corresponding eigenmode.

Similarly to the acoustic and optical modes assignment in a continuous trilayer consisting of two ferromagnetic films separated by a non-magnetic spacer, the calculated modes can be classified according to whether the precessional motion of the dynamic magnetizations in the Py and Co discs is in-phase or out-of-phase [121, 126].

7.4 Experimental results of dipolar coupled patterned trilayers

7.4.1 Static properties

XRMS measurements

The sample with $10nm$-thick Cu spacer shows a particular oscillating behaviour of the magnetization in the Py-layer, related to the correspondent behaviour of the magnetization in the underlying Co-layer (Fig.7.6) [127]. The hysteresis loops calculated with micromagnetic simulations reproduces quite well the experimental loops and enables to understand the magnetization curves of each layer (Fig.7.6). As the external field is reduced from positive saturation to zero,

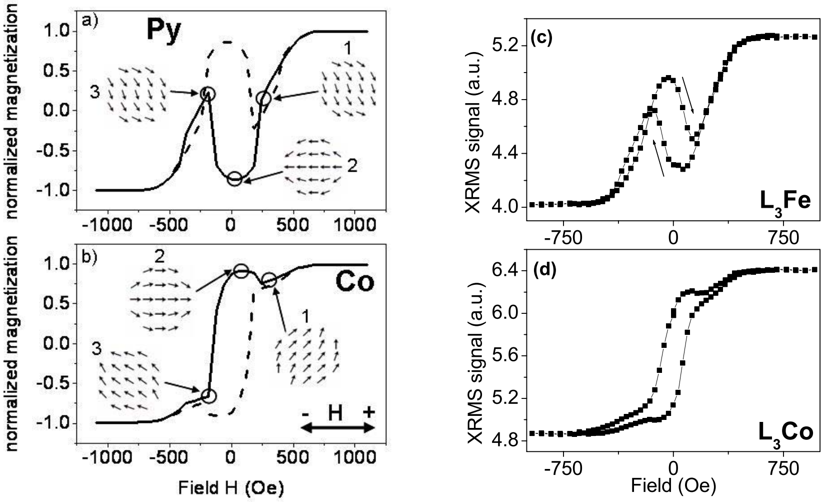

Figure 7.6: Simulated hysteresis loops of the circular discs with 10*nm*-thick Cu for both Py (a) and Co (b) layers. The insets show the relevant magnetization configurations occurring during the reversal (the external field is applied horizontally as sketched). XRMS hysteresis loops of the same sample, measured setting the x-rays photon energy at the Fe L_3 (c) and CoL_3 (d) thresholds.

the magnetization of the Py-layer rotates by 180° clockwise in a continuous way from being parallel to the applied field, first then the Co-layer, due to its lower magnetic moment. This rotation brings to the smooth drop to negative values of XRMS and simulated signals observed in the Py loops. In the same field range the magnetization of the Co first rotates by 45° counter-clockwise yielding to a small decrease in the XRMS and simulated signals and then back to the initial direction as the field is reduced to zero. In the remanent state the magnetization of the two ferromagnetic layers reaches a perfect antiparallel alignment with its direction parallel to the direction of the external applied field. This antiparallel configuration is clearly due to the dipolar interaction between the two layers in order to reduce the stray field of the structure closing the magnetization flux when the external field has reached the value zero. As the field is further reduced to negative values, at a critical field intensity, the magnetization of the Co-layer suddenly rotates by 135° counter-clockwise causing a corresponding rotation by

135° in the same direction, of the magnetization of the dipolar-coupled Py-layer. The magnetizations of the two ferromagnetic layers are antiparallel again but along a direction rotated respect to the external field. Finally, as the external field is increased further towards negative saturation values, the magnetization in both layers aligns gradually along the field direction.

The micromagnetic simulations explain the dominance of the magnetostatic dipolar interaction between the two layers and show that the magnetization of both layers remains in a nearly single domain state during the entire reversal process. Py and Co single discs of diameter and thickness as of those investigated here should show the formation of a vortex state during the reversal [128] just as checked with micromagnetic simulations. The dipolar coupling can be also viewed stabilizing the single domain state in the following way: the vortex nucleation field for such ferromagnetic discs should be near $H = 0$; the dipolar interaction forces the magnetization of the two layers to become antiparallel at a value of external filed $H > 0$ (coming from positive saturation), i.e. when the magnetization configurations are still nearly single domain; the antiparallel alignment of the two magnetizations considerably reduces the magnetostatic energy, just as the formation of the vortex state would do. What decides whether or not there is vortex formation is whether or not the vortex nucleation field of a layer anticipates the critical field for the onset of the antiparallel alignment. These two critical field values can be modified playing with the size, diameter and thickness of the discs as well as with the shape of discs and the thickness of the non-magnetic spacer, as it will be show in the sections relative to the other investigated samples.

MOKE measurements

The magneto-optic Kerr effect (MOKE) measurements have been carried out in the longitudinal configuration using the modulation polarization technique explained in the third chapter.

The magneto-optical sensitivity function, i.e. the dependence of the Kerr effect on the angle of incidence can show very interesting aspects about the investigation of heterostructures, being the profile of such function different for the different material that constitute the multilayered element [129]. In a sample as the trilayers studied in this chapter, the sensitivity of the Py may decrease, vanish or switch sign changing the incidence angle while the sensitivity of the Co may be relatively constant in the same range of angles and vice-versa. Selecting a determined angle of incidence, the MOKE rotation and ellipticity can be linearly combined in order to distinguish each layer's magnetization, practically [127]:

$$I_\epsilon = S_1 M_{Py}(H) + S_2 M_{Co}(H), \qquad I_R = S_3 M_{Py}(H) + S_4 M_{Co}(H) \tag{7.2}$$

where I_ϵ and I_R are the measured MOKE ellipticity and rotation, respectively. The sensitivity coefficients S_i are derived from MOKE measurements on the Py/Cu/Co reference layer. Combining the expressions of Eq.7.2 the magnetization loops for each material can be also obtained:

$$M_{Py}(H) \propto (S_4 I_\epsilon - S_2 I_R), \qquad M_{Co}(H) \propto (S_3 I_\epsilon - S_1 I_R) \tag{7.3}$$

The extracted loops of Py and Co layers (panel (c) and (d) of Fig. 7.7) from the MOKE rotation and ellipticity are in good agreement with those measured with the element sensitive XRMS (panel (e) and (f) of Fig. 7.7).

7.4.2 Dynamic properties

The spin wave modes properties of this patterned trilayer have been studied by the Brillouin light scattering technique [130]. Among the measurements performed at different values of the bias field H, the BLS spectrum at $1000 Oe$ has been selected as representative (Fig.7.8). Two broad peaks are present though the calculated power spectrum for the same bias field shows three principal peaks, activing in the scattering process (Fig.7.9). Considering that the two ferromagnetic layers remain in the nearly single domain state during

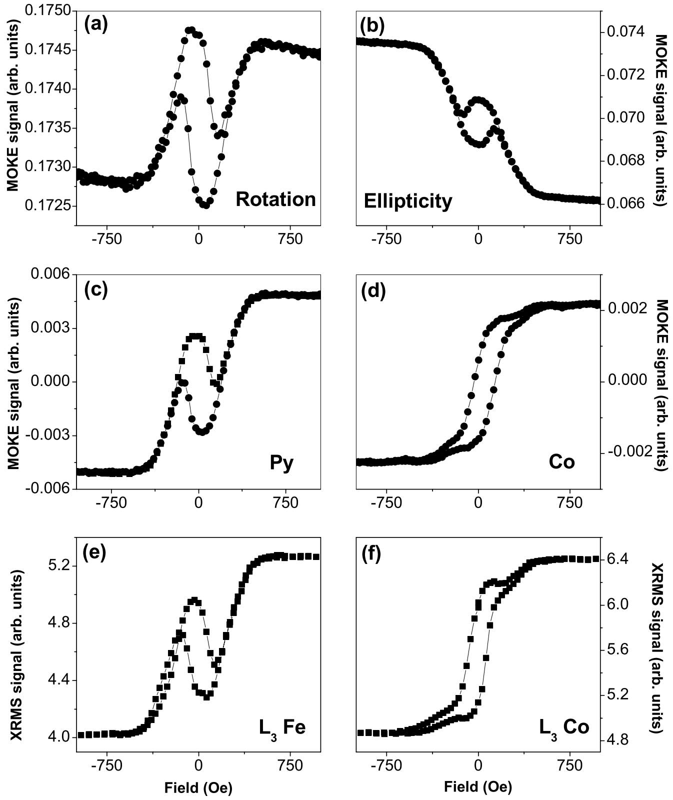

Figure 7.7: MOKE rotation (a) and ellipticity (b) hysteresis loops measured for the sample of $\mathrm{Py}_{(10nm)}/\mathrm{Cu}_{(10nm)}/\mathrm{Co}_{(10nm)}$ circular discs. Extracted Py (c) and Co (d) MOKE loops. XRMS hysteresis loops measured setting the x-rays photon energy at the Fe L_3 (e) and CoL_3 (f) thresholds.

the entire magnetization reversal process, the magnetic eigenmodes relative to the calculated peaks can be classified with similar standard described in the Ref.[125, 126]. Four categories can be pointed out: (i) end modes (n-EM) where all the amplitudes of the mode is concentrated close the sample adge, (ii) backwardlike (m-BA) modes where the nodes are locally perpendicular to the static magnetization $\mathbf{M}$, (iii) modes with nodal lines locally parallel to $\mathbf{M}$ called Damon-Eshbach-like (n-DE) modes and (iv) modes with no nodal lines labelled as fundamental (F). The integer numbers n and m specify the number of nodal lines. Moreover, a mode has been defined as 'hybrid' when is the result of a combination of more 'pure' modes.

The mode at $5.4GHz$ is an end mode (EM) with the magnetization of the

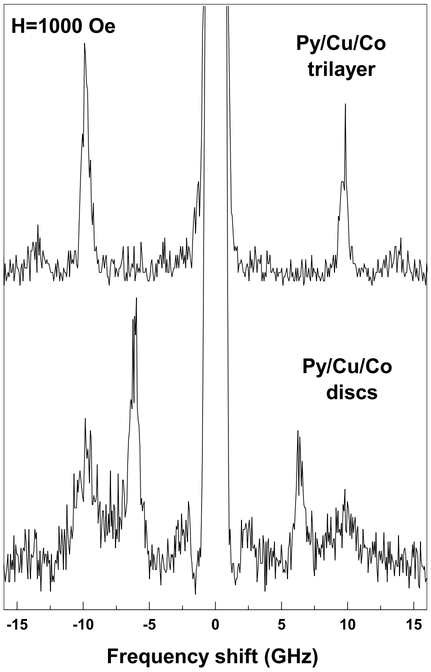

Figure 7.8: BLS power spectra of the $\mathrm{Py}_{(10nm)}/\mathrm{Cu}_{(10nm)}/\mathrm{Co}_{(10nm)}$ continuous film and patterned samples, measured appying $H = 1000 Oe$.

Py and Co layers oscillating in-phase near the particle edges. The mode at $6.8GHz$ has the character of the fundamental mode of the Py layer, but with a hybridization with an end mode, as evidenced by the nodal lines at the edges of the Py disc. A magnetization oscillation of the type EM is showed also in the Co layer, though weaker than that of the Py one. Similarly, the mode at $10.2GHz$ corresponds to the fundamental mode of the Co disc, still hybridized with an end mode. The Py layer shows instead a backwardlike mode at this frequency, i.e. nodal lines perpendicular to the applied field, even if with a reduced oscillation amplitude. The two calculated mode at $6.8GHz$ and $10.2GHz$ result an in-phase and an out-of-phase precessional motions of the dynamical magnetizations in the two layers, respectively.

So these results indicate that the spatial distribution in the two ferromagnetic layers does not have the same symmetry and amplitude, unlike precedent results on similar Py/Cu/Py discs [121]. The field evolution of the simulated

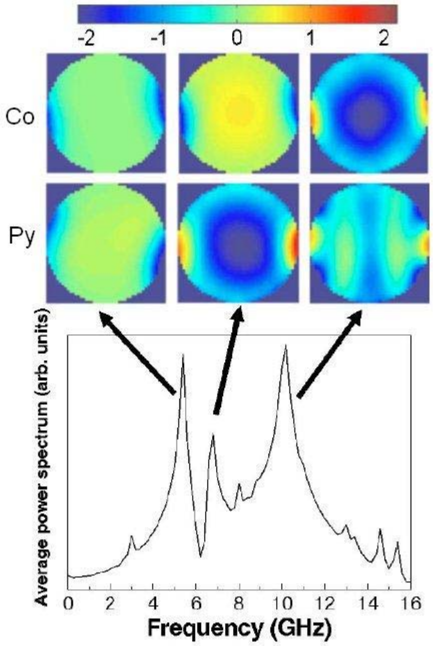

Figure 7.9: Calculated average power spectrum of the $\mathrm{Py}_{(10nm)}/\mathrm{Cu}_{(10nm)}/\mathrm{Co}_{(10nm)}$ circular discs for the external field $H = 1000Oe$ and applied horizontally. On the bottom panel the spatial profiles for Py and Co layers of the three corrispondent eigenmodes.

near-fundamental modes is compared to the measured ones, where the magnetic field has been varied between $+1500Oe$ and $-1500Oe$ (Fig.7.10) In the same figure the data of the continuous reference trilayer are also added. The frequency values of the two experimental peaks of the patterned sample are always smaller than those measured for the continuous trilayer.

On reducing the field intensity, the frequency of all the modes decreases monotonously and reaches a minimum at about $500Oe$, which corresponds to the saturation field of the two ferromagnetic layers (see Fig.7.6). On further decreasing the field intensity, an increase of the frequencies of the modes is observed, reflecting the rotation of the magnetizations of the two layers.

The continuous Py/Cu/Co sample shows instead a monotonic decrease of the frequencies when the magnetic field is reduced to zero.

Finally the presence of hybridized modes is confirmed by the well reproduction of the lowest frequency mode in the region between $350Oe$ and $700Oe$,

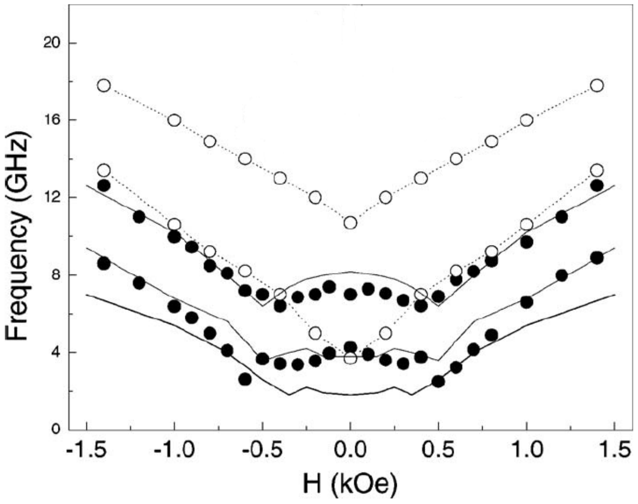

Figure 7.10: Measured frequencies as function of the applied field H from positive to negative saturation values for $\mathrm{Py}_{(10nm)}/\mathrm{Cu}_{(10nm)}/\mathrm{Co}_{(10nm)}$ circular discs (full points) and the continuous $\mathrm{Py}_{(10nm)}/\mathrm{Cu}_{(10nm)}/\mathrm{Co}_{(10nm)}$ trilayer reference (open points). The continuous and dotted curves are the respectively calculated curves.

where the fundamental Py mode is hybridized with the end mode.

7.4.3 Shape and thickness effects

Patterned elements with the same layering scheme but with different shape or thickness of the two ferromagnetic Py and Co layers are investigated in order to gain information about the role played by the geometrical parameters on the magnetization reversal process in multilayered stacks. As it was stressed when the experimental static results of the $\mathrm{Py}_{(10nm)}/\mathrm{Cu}_{(10nm)}/\mathrm{Co}_{(10nm)}$ circular discs were presented, the two critical fields of the antiparallel alignment and of the vortex nucleation can be engineered by playing with just these geometric characteristics of the layers.

The XRMS measurements on the Py/Cu(10nm)/Co circular discs with 30nm thickness of the two ferromagnetic layers do not show a substantially different behaviour in the magnetization reversal process with respect to the principal sample of $\mathrm{Py}_{(10nm)}/\mathrm{Cu}_{(10nm)}/\mathrm{Co}_{(10nm)}$ circular discs, as it can be observed in Fig.7.11. Nevertheless the increased thickness of the Py and Co layers causes

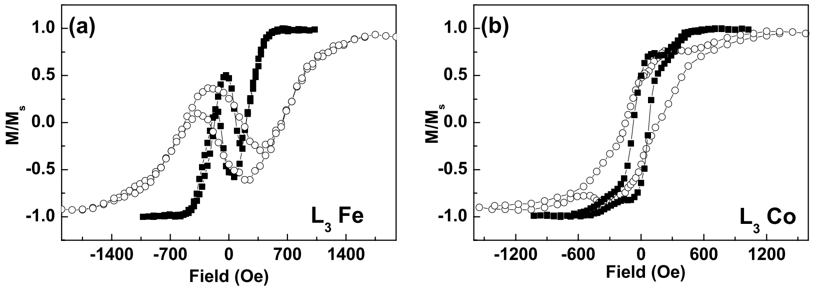

Figure 7.11: XRMS hysteresis loops measured setting the x-ray photon energy at the Fe L_3 (a) and Co L_3 (b) thresholds for Py/Cu$_{(10nm)}$/Co circular discs with $10nm$-thick Py and Co (solid symbol) and $30nm$-thick Py and Co (open symbol).

an increase of saturation field value because of the larger amount of magnetic charges accumulated at the edges of the magnetic elements which produces an increase of the demagnetizing field.

As in the Py$_{(10nm)}$/Cu$_{(10nm)}$/Co$_{(10nm)}$ sample, in this case the magnetostatic dipolar interaction induces an antiparallel coupling between the Py and Co layers, but the magnetic field range where the two ferromagnetic layers are antiparallel aligned is wider. This different peculiarity as well as the increasing of saturation field value is confirmed also by the micromagnetic simulations, performed with the same code of those calculated for the principal sample, changing only the thickness of the Py and Co discs (Fig.7.12).

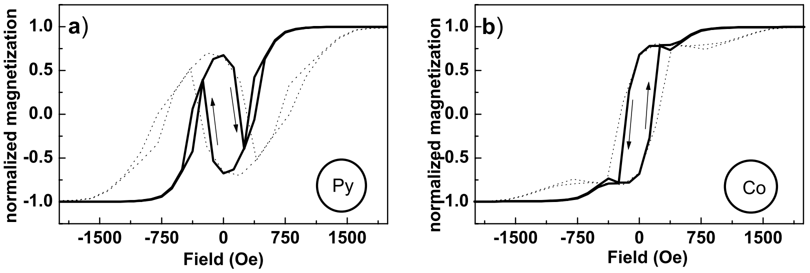

Figure 7.12: Calculated hysteresis loops of Py (a) and Co(b) for Py/Cu$_{(10nm)}$/Co circular discs with $10nm$-thick Py and Co (solid line) and $30nm$-thick Py and Co (dash line).

Despite the larger thickness of the ferromagnetic layers, both the Py and Co nano-elements remain in a nearly single domain state during the reversal magnetic process. This could be ascribed to the fact that the magnetostatic dipolar interaction between the two ferromagnetic layers continues to obstacle the vortex formation in the same way as is explained in the previous section.

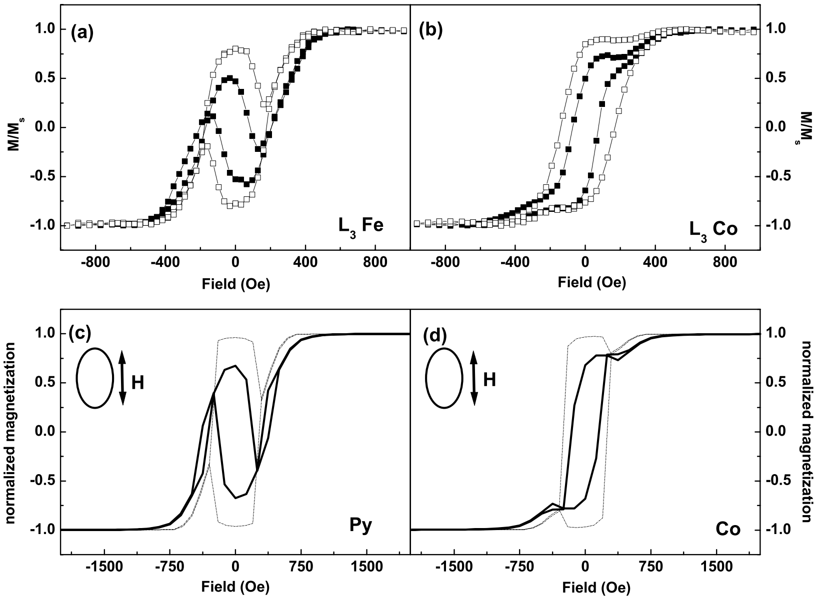

Figure 7.13: XRMS hysteresis loops at the Fe L_3 (a) and Co L_3 (b) thresholds for $\mathrm{Py}_{(10nm)}/\mathrm{Cu}_{(10nm)}/\mathrm{Co}_{(10nm)}$ circular (solid symbol) and elliptical (open symbol) discs. At the bottom panels, the corresponding simulated loops for the same layers thicknesses (solid line is relative to circular discs and dash dot line is relative to elliptical discs).

The investigation on $\mathrm{Py}_{(10nm)}/\mathrm{Cu}_{(10nm)}/\mathrm{Co}_{(10nm)}$ elliptical elements, when the external field is applied along the long axis of the ellipses (magnetization easy direction) confirms again the antiparallel alignment between the two ferromagnetic layers, but the shape anisotropy favours the alignment of the two layers magnetization with the external field. Both the XRMS measurements and the simulated data show a higher remanent state and coercivity for the elliptical elements with respect to the circular ones (Fig.7.13). Therefore the antiparallel state is more pronounced and more stable, i.e. present over a wider field range. This is not in contradiction with the fact that the whole process of inversion of the magnetization undergoes a slight delay in the case of ellipses, setting up at smaller field values, due to the stabilization effect of magnetization in the field direction caused by the elongated shape. Once the magnetization reversal process starts it develops faster in ellipses, as can be observed comparing the different slopes of the loops corresponding to circular and elliptical particles, coming from the saturation.

7.4.4 Conclusions

In the case of $10nm$ thick Cu spacer, the reversal process is determined by the magnetostatic dipolar interaction that favours the antiferromagnetic alignment of the two layer of Py and Co. Moreover, the dipolar interaction prevents the formation of a vortex state in the discs of these pseudo-spin valves.

The comparison between BLS measurements and dynamic simulations has also allowed to correlate the field dependence of the different spin wave modes in each ferromagnetic layer to their localization inside the disc. The spatial mode distribution in the Py and Co layers does not have the same symmetry and amplitude and shows two in-phase and one out-of-phase precessional motions of the dynamical magnetizations in the two layers.

Finally, the thickness increasing of the ferromagnetic layers stabilizes the antiparallel alignment of the layers over a wider field range. A similar behaviour, accompanied by a delay in the onset of the antiparallel aligment, is obtained using elements with elongated shape (ellipses) and applying the external field along the longer axis of the elements, due to the additional shape anisotropy.

7.5 Experimental results of exchange coupled patterned trilayers

7.5.1 Static properties

XRMS and MOKE measurements of the $1nm$ Cu thickness sample

The measurements relative to the sample with $1nm$-thick copper spacer show a remarkably similar shape of MOKE ellipticity and rotation, indicating that both layers undergo the same magnetization reversal process as it is confirmed by the

XRMS loops (Fig. 7.14) [127]. The shape of such loops is typical of a vortex

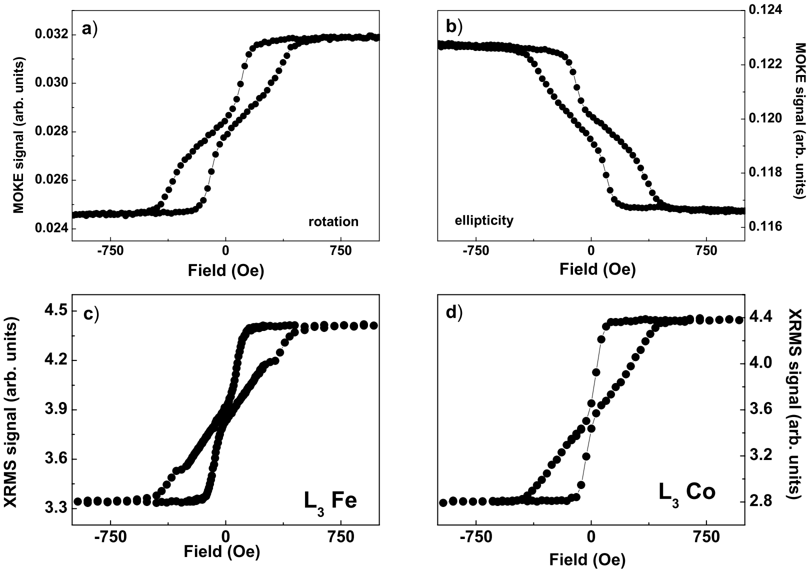

Figure 7.14: MOKE rotation (a) and ellipticity (b) hysteresis loops measured for the sample with $1nm$-thick Cu spacer. XRMS hysteresis loops measured setting the x-rays photon energy at the Fe L_3 (c) and Co L_3 (d) thresholds.

nucleation process [128] for the Py as well as for the Co layers. In this case the critical field for the onset of the antiparallel alignment has been delayed with respect to the case of the $10nm$ Cu thickness so that the vortex formation can occur first. The dipolar coupling can be not the only interaction between the two ferromagnetic layers, there must be a ferromagnetic interaction which, by competing with the antiferromagnetic dipolar coupling, generates frustration and reduces the critical field for the antiparallel alignment below the vortex nucleation field value.

Adding the bilinear coupling term explained in the section relative to the micromagnetic simulations, the calculated loops confirm the vortex formation for both layers and show a quite well agreement with the measured loops (Fig. 7.15). Starting from the saturation of the sample and decreasing the external field value, the magnetization in the two discs evolves toward a vortex nucleation at zero field, getting through an ‘S’ configuration. The chirality of the vortex

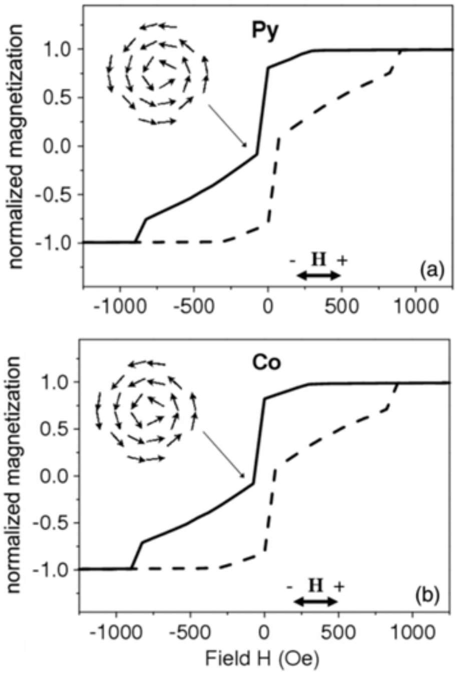

Figure 7.15: Simulated hysteresis loops of discs with $1nm$-thick Cu spacer for both Py (a) and Co (b) layers. The insets show the vortex magnetization configuration occurring during the reversal (the field is applied as sketched).

is the same for the two ferromagnetic layers, as showed by the inset static configurations at remanence in Fig.7.15. When the field changes direction the system keeps its vortex state until the expulsion of the core and the consequent alignment of the magnetization parallel to the external field in both the Py and Co discs.

It is interesting to notice that the saturation field is smaller than that measured for the Cu spacer of $10nm$, because in this latter case a larger magnetic field is necessary to force the magnetization of the two Py and Co layers to be parallel against the antiparallel dipolar interaction.

Through the obtained results of this only sample with a such copper spacer that a short-range interaction is prevailing on the dipolar one, it results difficult to state that the origin of this ferromagnetic coupling is the indirect exchange interaction between the Py and Co layers via the Cu spacer. Although the literature confirms a ferromagnetic coupling for Co/Cu/Co and Py/Cu/Py multilayers with a Cu thickness in the range of $1 - 1.5nm$ and confirms also the coherence of the selected J constant equal to $0.16ergcm^{-2}$ with the typical values for this Cu thickness [40, 114, 118], it is not possible to rule out a partial contact between the Py and Co layers (pinholes) due to a non-homogeneity of the Cu spacer [36].

Therefore static and dynamic studies are performed on similar discs of $\mathrm{Py}_{(10nm)}/\mathrm{Cu}_{(\mathrm{t_{Cu}})}/\mathrm{Co}_{(10nm)}$ with different values of the copper spacer thickness in the range $0.7 - 2.0nm$.

XRMS measurements of the $0.7 - 2.0nm$ Cu thickness samples

In the samples with Cu spacer thickness equal to $0.7, 1.2$ and $2.0nm$ the interlayer exchange interaction continues to couple ferromagnetically the two layers of Py and Co, being dominant over the antiferromagnetic dipolar interaction. The XRMS longitudinal hysteresis loops for both Py and Co layers are substantially identical, as shown in Fig.7.16. As already explaned in the section relative to simulation, the micromagnetic calculation have been carried out only for the trilayered discs sample with Cu thickness of $2nm$ and the J constant has been fixed equal to $0.25ergcm^{-2}$ rather than the $0.16ergcm^{-2}$ value used in the static simulation of the $\mathrm{Py}_{(10nm)}/\mathrm{Cu}_{(1nm)}/\mathrm{Co}_{(10nm)}$ sample. The result is substantially the same as can be seen comparing the continuous curves in Fig.7.16 and Fig.7.15. The shape of the calculated loops reproduce qualitatively well the measured ones, but the vortex annihilation field is overestimated probably because the OOMMF calculations are performed at T$= 0K$.

The shape of XRMS measured loops for the three samples changes appreciably on decreasing the copper spacer thickness, in particular an increase of the remanence value is observed while the saturation field remains almost constant.

7.5.2 Dynamic properties

The dynamic investigation through the Brillouin light scattering (BLS) shows that the Py/Cu/Co reference samples (continuous film) with Cu thickness in

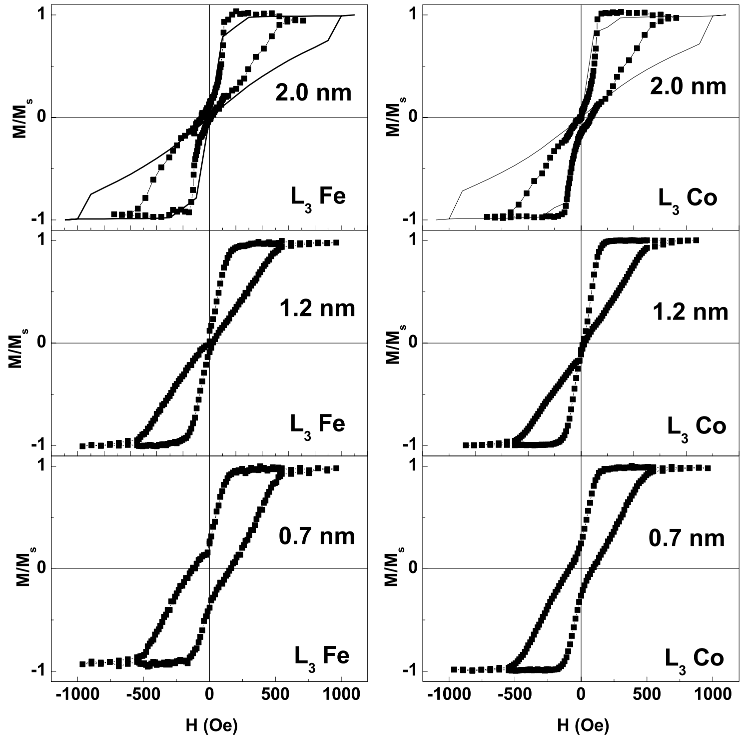

Figure 7.16: Normalized longitudinal hysteresis curves measured by XMRS for different thickness of the Cu spacer. For the sample with $2nm$-thick Cu spacer the simulated magnetization curves are plotted (continuous curve).

this restricted range have spectra consisting of two spin-wave modes associated to the in-phase (acoustic) and out-of-phase (optic) precession of the spin in the Py and Co layers (Fig.7.17) [131]. The presence of these two distinct modes enables to rule out any partial contact between the Py and Co layers and to exclude the presence of pinholes in these trilayered structures is now possible .

Considering a value of $800Oe$ for the applied external field, the measured frequencies can be plotted as function of the copper thickness (Fig.7.18). The frequency of the lowest mode has little dependence on the Cu thickness while that of the high frequency mode largely increased on reducing the copper thickness. Using the bilinear interlayer coupling as unique adjustable parameter in a fitting procedure, it is possible to reproduce the magnetic field dependence of these two modes and also their dispersion curve. In this way the ferromagnetic

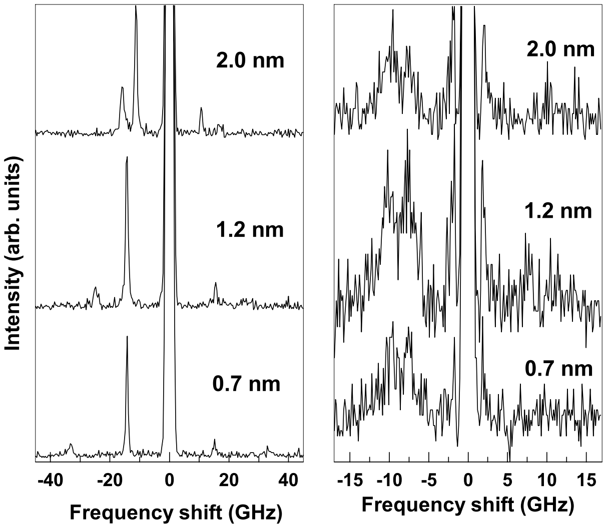

Figure 7.17: Sequence of measured BLS spectra for the unpatterned (left panel) and Py/Cu/Co discs (right panel) for the different Cu spacer thicknesses in an applied external field of $800Oe$.

coupling term are calculating as function of the copper thickness and as shown in the inset of Fig.7.18, its value varies from $0.15ergcm^{-2}$ for a $t_{Cu} = 2.0nm$ to $22ergcm^{-2}$ for a $t_{Cu} = 0.7nm$.

In the spectra of the respective patterned samples two peaks are also visible but they result dispersionless and the frequency value of both of them is smaller than the acoustic mode in the unpatterned samples (Fig.7.17). The demagnetizing field generated by the finite-size of the disc could explain this reduction of the frequency values.

To understand the spatial profiles of eigenmodes micromagnetic simulations are performed with the same procedure used for the dipolar coupled $\mathrm{Py}_{(10nm)}/\mathrm{Cu}_{(10nm)}/\mathrm{Co}_{(10nm)}$ nanodiscs. As has already been explaned, only the stack with the copper spacer equal to $2.0nm$ has been simulated. The calculated power spectra show several peaks corresponding to different eigenmodes for the two ferromagnetic layers (Fig.7.19). For the Py disc an end mode (EM) at lower frequency can be seen and increasing in frequency, a fundamental (F) and a couple of Damon-Eshbach (DE) modes are visible. For the Co layer, in

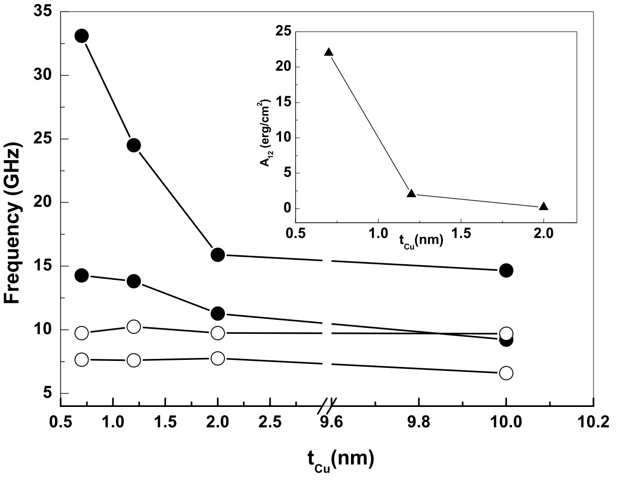

Figure 7.18: Spin wave frequency measured by BLS in the unpatterned (full points) and patterned (open points) Py/Cu/Co samples for different values of the Cu spacer thickness. The applied field value is of $800Oe$. The data for $10nm$-thick Cu spacer taken from [127] are shown for comparison. The fitted values of the interlayer coupling constant values are reported in the inset (for $10nm$-thick Cu spacer the interlayer coupling constant is zero).

addition to the EM and F modes a sort of hybrid mode is found. It is neither a pure fundamental mode nor an end mode and it is classified as F+2-EM. The two Damon Eshbach modes of the Co are at $14GHz$ and $17GHz$, i.e. outside the frequency range explored in this experiment. The simulated and experimental power spectra result quite different relating to the number of peaks as well as to the frequency values of the eigenmodes. However taking a second exam, the two fundamental modes are the most intense peaks in both the power spectra of Py and Co, with the same frequency, about $8.0GHz$, and the same spatial profile. This is the direct evidence of the presence of a non-negligible interlayer exchange coupling in this trilayered system. In fact the same investigation on the sample with the copper spacer of $10nm$ thickness showed different frequency values for the two fundamental modes of Py and Co discs (see also the related section). Concerning the other simulated peaks, it is important to notice that the only modes contributing to the measured spectra are those with the largest cross-section, i.e. the mode at $8.0GHz$ and the one at $10.0GHz$. This latter is probably a convolution of the F+2EM mode for the Co disc and 2-DE modes for

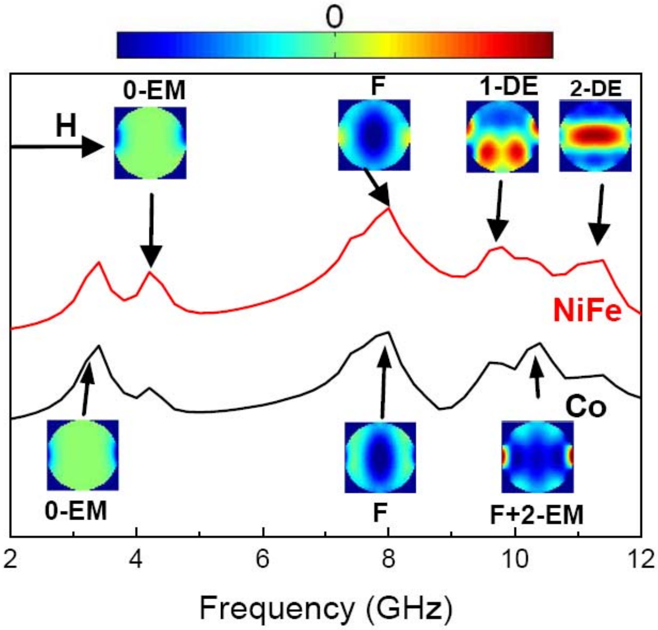

Figure 7.19: Calculated power spectra for the Py and Co discs for the sample with 2nm-thick Cu spacer in an external magnetic field of 800Oe. The spatial profiles corresponding to some relevant eigenmodes are shown as insets. The external field direction relative to the spatial profiles is shown.

the Py disc. The EM modes at about 4.0GHz are not discernible from the quite noisy experimental spectra. After all the area involved in the spin precession for such modes is quite reduced and the cross-section thus results small.

7.5.3 Conclusions

In the sample with 1nm thick Cu, the reversal of both layers occurs through the formation of a vortex structure. This behaviour can be explained as being due to the presence of a ferromagnetic coupling that, by contrasting the dipolar antiferromagnetic coupling, makes the vortex formation the favourite process to reduce the magnetostatic energy of the structure.

The following investigation of different values of the non-magnetic Cu spacer in the range $0.7 - 2.0nm$ has allowed to identify this ferromagnetic coupling with an interlayer exchange coupling and to quantitatively determine the intensity of this interaction as it varies with the thickness of the Cu spacer. The study of the spatial profiles of the magnetic excitations of the system outlines the presence of an in-phase fundamental mode which exists in both magnetic layers at the same frequency of about $8.0GHz$.

Conclusions

This thesis places itself within the basic research of differently shaped magnetic nanosystems with a view to technological application of data storage devices and spintronics. To control the magnetic switching of nano-objects precisely, one needs to a well defined picture of the equilibrium magnetic states and magnetization reversal mechanisms. In closed packed arrays, the effects of the inter-element interactions become important and their study reveals often very interesting aspects. The principal interaction is the dipolar coupling, because the demagnetising field leaking from the borders of the single object changes the effective magnetic field felt from the other neighbour elements of the array. This interaction has been investigated for each of the three sets of samples studied in this thesis: permalloy (Py) nanowires arrays, Py triangular microrings and Py/Cu/Co nanosize discs. The single elements of the array have been arranged very close (tens of nanometers) in the first two samples in order that the coupling direction is substantially in the plane of the sample surface. The trilayered systems show an out of plane interaction instead, because the elements of the array are separated by a larger distance in order to neglect the dipolar coupling between adjacent trilayer discs and to consider only the dipolar interaction between the Py and Co layers within the single element of the array. Reducing the thickness of the Cu spacer, another kind of coupling between the Py and Co layers emerges, the short range interlayer exchange interaction.

Py nanowires with fixed width of $185nm$, spacing of $35nm$ and film thicknesses from 10 to $120nm$ have been investigated with vectorial Magneto-optical Kerr effect (MOKE) magnetometry. The magnetization reversal mechanism results strongly dependent on film thickness and in particular shows a transition from coherent rotation to inhomogeneous reversal mode for wires thickness above $80nm$. The effects of dipolar interactions are evidenced by the variation of the saturation field in the hard-axis hysteresis loops as a function of wires thickness, showing that the dipolar coupling starts to play a role for wires thickness $\geq 20nm$.

The motion and pinning of domain walls have been investigated in vertical and horizontal chains of Py triangular microrings and compared with the isolated rings case. In the former interacting sample an apex of each triangle is in proximity to the edge centre of the triangle above it, in the latter the proximity is between the adjacent corners of the triangles. The investigation is a combined numerical and experimental study, performing the longitudinal and diffracted magneto-optical Kerr effects and magnetic force microscopy (MFM).

Triangular rings are particularly interesting because the remanent state of each ring is an 'onion' state characterized by two domain walls positioned at two vertices of the triangle. The magnetization reversal takes place through two onion states via the formation of an intermediate vortex state, which arises from the motion and annihilation of the two domain walls.

The study of field dependence of the spin structure in the rings shows an additional intermediate state during reversal in the case of vertical chains. The new state involves a domain wall pinned at the center of the edge that is in close proximity to the apex of its neighbour. This study can be thus considered as a preliminary approach for the development of magnetic logic applications.

For future development it would be interesting to speculate that if one were to construct a triangular ring with two smaller triangular rings below its base, switching in the large ring might be tailored to depend on the magnetic state of both small rings. Such structures could lead directly to magnetic logic gates.

Static and dynamical properties have been studied in patterned Py/Cu/Co arrays with different shape and thickness in order to clarify the interplay between dipolar and interlayer exchange interactions and to introduce further possibilities for manipulating the magnetic behaviour of the system. The complexity of the study has required 3D micromagnetic simulations and the employ of different experimental techniques, the already cited Magneto-optical Kerr effect (MOKE), followed by the X-ray resonant magnetic scattering (XRMS) and by the Brillouin light scattering (BLS).

A first investigation on dipolar coupled $\mathrm{Py}_{(10nm)}/\mathrm{Cu}_{(10nm)}/\mathrm{Co}_{(10nm)}$ circular discs have shown that the interaction favours the antiparallel alignment of the magnetization of the Py and Co layers at remanence, having the two ferromagnetic material different reversal nucleation fields. It is worth noting that, during the reversal process, the magnetization of the two layers remains in a nearly single domain state thanks to the dipolar coupling. The results have been confirmed by investigations of magnetic dynamic and by a following work about $\mathrm{Py}/\mathrm{Cu}_{(10nm)}/\mathrm{Co}$ circular and elliptical nano-elements with different thicknesses of the magnetic layers.

Reducing the thickness of Cu spacer to a range $0.7 - 2.0nm$, both the simulations and meausurements show that the reversal is accomplished via the formation of a vortex state in both discs due to the presence of a ferromagnetic exchange coupling that competes with the dipolar interaction.

The dynamical study has been fundamental to clarify the nature of this short range interaction, showing the presence of an in-phase fundamental mode which exists in both magnetic layers at the same frequency.

Bibliography

[1] S. S. P. Parkin, N. More, K. P. Roche, *Phys. Rev. Lett.*, **64**, 2304 (1990).

[2] M. N. Baibich, J. M. Broto, A. Fert, F. Nguyen Van Dau, F. Petroff, P. Etienne, G. Creuzet, A. Friederich, J. Chazelas *Phys. Rev. Lett.*, **61**, 2472 (1988).

[3] G. Binasch, P. Grünberg, F. Saurenbach, W. Zinn, *Phys. Rev.* B, **39**, 4828 (1989).

[4] J. G. Gay, R. Richter, *Phys. Rev. Lett.*, **56**, 2728 (1986).

[5] B. T. Jonker, K-H Walker, E. Kisker, G. A. Prinz, C. Carbone, *Phys. Rev. Lett.*, **57**, 142 (1986).

[6] R. P. Cowburn, *J. Phys. D: Appl. Phys.*, **33**, R1-R16 (2000).

[7] X. Portier, A. K. Petford-Long, *J. Phys. D: Appl. Phys.*, **32**, R89 (1999).

[8] A. Aharoni, *Introducttion to the Theory of Ferromagnetism*, (Oxford University Press, Oxford, 1996).

[9] W. F. Brown, *Micromagnetics*, (Wiley, New York, 1963).

[10] R. Carey, E. D. Isaac, *Magnetic Domains and Techniques for their Observation*, (English Universities Press, London, 1966).

[11] S. D. Bader, *Rev. Mod. Phys.*, **78**, 1 (2006).

[12] L. Néel, *Ann. Geophys. (C.N.R.S.)*, **5**, 99 (1949).

[13] C. Kittel, *Rev. Mod. Phys.*, **21**, 541 (1949).

[14] P. Vavassori, *Riv. Nuovo Cimento*, **25**, 10 (2002).

[15] M. Solzi, M. Ghidini, G. Asti, *Magnetic Nanostructures*, edited by H. S. Nalwa (American Scientific Publishers, Los Angeles, 2002).

[16] J. A. Osborn, *Phys. Rev.*, **67**, 351 (1945).

[17] T. Shinjo, T. Okuno, R. Hassdorf, K. Shigeto, T. Ono, *Science*, **289**, 930 (2000).

[18] E. H. Frei, S. Shtrikman, and D. Treves, *Phys. Rev.*, **106**, 446 (1957).

[19] P. Vavassori, O. Donzelli, V. Metlushko, M. Grimsditch, B. Ilic, P. Neuzil, R. Kumar, *J. Appl. Phys.*, **88**, 999 (2000).

[20] J. A. Johnson, M. Grimsditch, V. Metlushko, P. Vavassori, B. Ilic, P. Neuzil, R. Kumar, *Appl. Phys. Lett.*, **77**, 4410 (2000).

[21] Y. Zheng, J. G. Zhu, *J. Appl. Phys.*, **81**, 5471 (1997).

[22] M. Herrmann, S. Mcvitie, J. N. Chapman, *J. Appl. Phys.*, **87**, 2994 (2000).

[23] K. J. Kirk, J. N. Chapman, C. D. Wilkinson, *Appl. Phys. Lett.*, **71**, 539 (1997).

[24] T. L. Gilbert, *Phys. Rev.*, **100**, 1243 (1955).

[25] R. P. Cowburn, M. E. Welland, *Science*, **287**, 1466 (2000).

[26] R. P. Cowburn, *Phys. Rev.* B, **65**, 092409 (2002).

[27] R. P. Cowburn, *J. Magn. Magn. Mater.*, **242-245**, 505 (2002).

[28] M. Grimsditch, Y. Jaccard, I. Schuller, *Phys. Rev.* B, **58**, 11539 (1998).

[29] J. S. Moodera, L. R. Kinder, T. M. Wong, R. Meservey *Phys. Rev. Lett.*, **74**, 3273 (1995).

[30] J. F. Bobo, L. Gabillet, M. Bibes *J. Phys.: Condens. Matter*, **16**, 471 (2004).

[31] M. A. Ruderman, C. Kittel *Phys. Rev.*, **96**, 99 (1954).

[32] T. Kasuya *Prog. theor. Phys.*, **16**, 45 (1956).

[33] K. Yosida *Phys. Rev.*, **106**, 893 (1957).

[34] J. C. Slonczewski *Phys. Rev. Lett.*, **67**, 3172 (1991).

[35] J. F. Bobo, H. Kikuchi, O. Redon, E. Snoeck, M. Piecuch, R. L. White *Phys. Rev.* B, **60**, 4131 (1999).

[36] J. F. Bobo, H. Fischer, M. Piecuch, *Mater. Res. Soc. Symp. Proc.*, **313**, 467 (1993).

[37] P. Grünberg, R. Schreiber, Y. Pang, M. B. Brodsky, H. Sowers *Phys. Rev. Lett.*, **57**, 2442 (1986).

[38] C. Carbone, S. F. Alvarado *Phys. Rev.* B, **36**, 2433 (1987).

[39] S. S. P. Parkin *Phys. Rev. Lett.*, **67**, 3598 (1991).

[40] F. Petroff, A. Barthélemy, D. H. Mosca, D. K. Lottis, A. Fert, P. A. Schroeder, W. P. Pratt, Jr., R. Loloee, S. Lequien *Phys. Rev.* B, **44**, 5355 (1991).

[41] P. Bruno, C. Chappert *Phys. Rev. Lett.*, **67**, 1602 (1991).

[42] P. Bruno, C. Chappert *Phys. Rev. Lett.*, **67**, 2592 (1991).

[43] P. Bruno, C. Chappert *Phys. Rev.* B, **46**, 261 (1992).

[44] M. T. Johnson, S. T. Purcell, N. W. E. McGee, R. Coehoorn, J. aan de Stegge, W. Hoving *Phys. Rev. Lett.*, **68**, 2688 (1992).

[45] B. Heinrich, J. F. Cochran *Adv. Phys.*, **42**, 523 (1993).

[46] M. D. Stiles *J. Magn. Magn. Mater.*, **200**, 322 (1999).

[47] P. Bruno *Europhys. Lett.*, **23**, 615 (1993).

[48] L. Néel *C. R. Acad. Sci.*, **255**, 1545 (1966).

[49] L. Néel *C. R. Acad. Sci.*, **255**, 1676 (1966).

[50] J. Kerr, *Philos. Mag.*, **3**, 339 (1877).

[51] J. Kerr, *Philos. Mag.*, **5**, 161 (1878).

[52] M. Faraday, *Trans. Royal Soc.*, **5**, 592 (1846).

[53] A. Hubert, R. Schäfer, *Magnetic Domains*, (Springer, Berlin, 1998).

[54] D. A. Allwood, Gang Xiong, M. D. Cooke, R. P. Cowburn *J. Phys. D: Appl. Phys.*, **36**, 2175 (2003).

[55] Z. Q. Qiu, S. D. Bader, *Rev. Sci. Instrum.*, **71**, 1243 (2000).

[56] H. R. Hulme, *Proc. R. Soc. London*, Ser. A **135**, 273 (1932).

[57] C. Kittel, *Phys. Rev.*, **83**, 208(A) (1951).

[58] P. N. Argyres, *Phys. Rev.*, **97**, 334 (1955).

[59] M. J. Freiser, *IEEE Trans. Magn.*, **MAG-4**, 152 (1968).

[60] C.-Y. You, S.-C. Shin, *J. Appl. Phys.*, **84**, 541 (1998).

[61] A. K. Zvezdin, V. A. Kotov, *Modern Magnetooptics and Magnetooptical Materials*, (Taylor and Francis Group, New York, 1997).

[62] R. P. Hunt, *J. Appl. Phys.*, **38**, 1652 (1967).

[63] Y. J. Yang, M. R. Scheinfein, *J. Appl. Phys.*, **74**, 6810 (1993).

[64] J. M. Florczak, E. Dan Dahlberg *J. Appl. Phys.*, **67**, 12 (1990).

[65] P. Vavassori, *Appl. Phys. Lett.*, **77**, 1605 (2000).

[66] R. C. Jones, *J. Opt. Soc. A*, **31**, 488-493 (1941).

[67] R. M. Osgood, S. D. Bader, B. M. Clemens, R. L. White, H. Matsuyama, *J. Magn. Magn. Mater.*, **182**, 297 (1998).

[68] O. Geoffroy, D. Givord, Y. Otani, B. Pannetier, A. D. Dos Santos, M. Schlenker, Y. Souche *J. Magn. Magn. Mater.*, **121**, 516 (1993).

[69] Y. Souche, M. Schlenker, A. D. Dos Santos, *J. Magn. Magn. Mater.*, **140-144**, 2179 (1995).

[70] Y. Souche, V. Novosad, B. Pannetier, O. Geoffroy, *J. Magn. Magn. Mater.*, **177-181**, 1277 (1998).

[71] P. Vavassori, V. Metlushko, R. M. Osgood, M. Grimsditch, U. Welp, G. Crabtree, Wenjun Fan, S. R. J. Brueck, B. Ilic, P. J. Hesketh, *Phys. Rev.* B, **59**, 6337 (1999).

[72] M. Grimsditch, P. Vavassori *J. Phys.: Condens. Matter*, **16**, R275-R294 (2004).

[73] M. Grimsditch, P. Vavassori, V. Novosad, V. Metlushko, H. Shima; Y. Otani, K. Fukamichi *Phys. Rev.* B, **65**, 172419 (2002).

[74] E.Meyer, H. J. Hug, R. Bennewitz, *Scanning Probe Microscopy: The Lab on a Tip*, (Springer, Berlin, 2004).

[75] G. Schütz, W. Wagner, W. Wilhelm, P. Kienle, R. Zeller, R. Frahm, G. Materlik, *Physic. Rev. Lett.*, **58**, 737 (1987).

[76] J. P. Hannon, G. T. Trammel, M. Blume, D. Gibbs, *Phys. Rev. Lett.*, **61**, 1245 (1998).

[77] C. Spezzani, S. Cherifi, M. Sacchi, J. Vogel, M. Fabrizioli and G. Panaccione, *Laterally confined magnetic systems studied by synchrotron radiation techniques*, in *Magnetic Properties of Laterally Confined Nanometric Structures*, (Transworld Research Network, Kerala (IN), 2006).

[78] G.Carlotti, G. Gubbiotti, *Riv. Nuovo Cimento*, **22**, 12 (1999).

[79] J. R. Sandercock, *Opt. Commun.*, **2**, 73 (1970).

[80] J. I. Martín, J. Nogués, Kai Liu, J. L. Vicent, Ivan K. Schuller, *J. Magn. Magn. Mater.*, **256**, 449 (2003).

[81] R. P. Cowburn, A. O. Adeyeye, M. E. Welland, *New J. Phys.*, **1**, 16 (1999).

[82] A. O. Adeyeye, J. A. C. Bland, C. Daboo, D. G. Hasko, and H. Ahmed, *J. Appl. Phys.*, **82**, 469 (1997).

[83] T. Masumoto, I. Ohnaka, A. Inoue, M. Hagiwara, *Scripta Metall.*, **15**, 293 (1981).

[84] G. C. Han, B. Y. Zong, P, Luo, Y. H. Wu, *J. Appl. Phys.*, **93**, 9202 (2003).

[85] J. Meier, B. Doudin, J. Ph. Ansermet, *J. Appl. Phys.*, **79**, 6010 (1996).

[86] N. Singh, S. Goolaup, A. O. Adeyeye, *Nanotechnology*, **15**, 1539 (2004).

[87] M. Knobel, L.C. Sampaio, E.H.C.P. Sinnecker, P. Vargas, D. Altbir, *J. Magn. Magn. Mater.*, **249**, 60 (2002).

[88] J. Velázquez, C. García, M. Vázquez, A. Hernando, *Phys. Rev.* B, **54**, 9903 (1996).

[89] L.C. Sampaio, E.H.C.P. Sinnecker, G. R. C. Cernicchiaro, M. Knobel, M. Vázquez, J. Velázquez, *Phys. Rev.* B, **61**, 8976 (2000).

[90] G. Gubbiotti, S. Tacchi, G. Carlotti, P. Vavassori, N. Singh, S. Goolaup, A. O. Adeyeye, A. Stashkevich, M. Kostylev, *Phys. Rev.* B, **72**, 224413 (2005).

[91] S. Goolaup, N. Singh, A. O. Adeyeye, V. Ng, M. B. A. Jalil, *Eur. Phys. J.* B, **44**, 259 (2005).

[92] C. H. Bajorek, C. Coker, L.T. Romankiv, D. A. Thompson, *IBM J. Res. Develop.*, **18**, 541 (1974).

[93] B. B. Pant, *J. Appl. Phys.*, **79**, 6123 (1996).

[94] P. Vavassori, V. Bonanni, G.Gubbiotti, A.O. Adeyeye, S. Goolaup, N. Singh, *J. Magn. Magn. Mater.*, **31**, e31-e34 (2007).

[95] M. J. Donahue, D. G. Porter, *OOMMF User's Guid, Version 1.2 alpha 3*, (NIST, Gaithersburg MD, 2002).

[96] J. G. Zhu, Y. Zheng, G. A. Prinz, *J. Appl. Phys.*, **87**, 6668 (2000).

[97] M. M. Miller, G. A. Prinz,S.-F. Cheng, S. Bounnak *Appl. Phys. Lett.*, **81**, 2211 (2002).

[98] M. Kläui, C. A. F. Vaz, J. A. C. Bland, W. Wernsdorfer, G. Faini, E. Cambril, *Appl. Phys. Lett.*, **81**, 108 (2002).

[99] M. Kläui, C. A. F. Vaz, J. Rothman, J. A. C. Bland, W. Wernsdorfer, G. Faini, E. Cambril, *Phys. Rev. Lett.*, **90**, 97202 (2003).

[100] S. Kasai, T. Niiyama, E. Saitoh, H. Miyajima, *Appl. Phys. Lett.*, **81**, 316 (2002).

[101] D. A. Allwood, G. Xiong, C. C. Faulkner, D. Atkinson, D. Petit, R. P. Cowburn, *Science*, **309**, 1688 (2005).

[102] M. Kläui, C. A. F. Vaz, L. Lopez-Diaz, J. A. C. Bland, *J. Phys.: Condens. Matter*, **15**, R985-R1023 (2003).

[103] J. Rothman, M. Kläui, L. Lopez-Diaz, C. A. F. Vaz, A. Bleloch, J. A. C. Bland, Z. Cui, R. Speaks, *Phys. Rev. Lett.*, **86**, 1098 (2001).

[104] S. P. Li, W. S. Lew, J. A. C. Bland, M. Natali, A. Lebib, Y. Chen *J. Appl. Phys.*, **92**, 7397 (2002).

[105] M. Kläui, J. Rothman, L. Lopez-Diaz, C. A. F. Vaz, J. A. C. Bland, *Appl. Phys. Lett.*, **78**, 3268 (2001).

[106] P. Vavassori, O. Donzelli, M. Grimsditch, V. Metlushko, B. Ilic, *J. Appl. Phys.*, **101**, 023902 (2007).

[107] A. Libál, M. Grimsditch, V. Metlushko, P. Vavassori, B. Jankó, *J. Appl. Phys.*, **98**, 083904 (2005).

[108] K. M. Lebecki, M. J. Donahue, M. W. Gutowski, *Journal of Physics* D, **41**, 175005 (2008).

[109] P. Vavassori, M. Grimsditch, V. Novosad, V. Metlushko, B. Ilic, *Phys. Rev.* B, **67**, 134429 (2003).

[110] P. Vavassori, D. Bisero, V. Bonanni, A. Busato, M. Grimsditch, K. M. Lebecki, V. Metlushko, B. Ilic, *Physical Review* B, **78**, 174403 (2008).

[111] C. F. Majkrzak, J. W. Cable, J. Kwo, M. Hong, D. B. McWhan, Y. Yafet, J. V. Waszcak, C. Vettier, *Phys. Rev. Lett.*, **56**, 2700 (1986).

[112] M. B. Salamon, S. Sinha, J.J. Rhyne, J. E. Cunningham, R. W. Erwin, J. Borchers, C. P. Flynn, *Phys. Rev. Lett.*, **56**, 259 (1986).

[113] M. D. Stiles, *Phys. Rev.* B, **48**, 7238 (1993).

[114] B. Heinrich,Z. Celinski, J. F. Cochran, W. B. Muir, J. Rudd, Q. M. Zhong, A. S. Arrott, K. Myrtle, J. Kirschner, *Phys. Rev. Lett.*, **64**, 673 (1990).

[115] D. Pescia, D. Kerkmann, F. Schumann, W. Gudat, *Phys. Rev.* B, **78**, 475 (1990).

[116] W. R. Bennett, W. Schwarzacher, W. F. Egelhoff, Jr., *Phys. Rev. Lett.*, **65**, 3169 (1990).

[117] Z. Celinski, B. Heinrich, *J. Magn. Magn. Mater.*, **99**, L25 (1991).

[118] S. S. P. Parkin, R. Bahdra, K. P. Roche, *Phys. Rev. Lett.*, **66**, 2152 (1991).

[119] B. Heinrich,Z. Celinski, J. F. Cochran, A. S. Arrott, K. Myrtle, S. T. Purcell, *Phys. Rev.* B, **47**, 5077 (1993).

[120] D. H. Mosca, F. Petroff, A. Fert, P. A. Schroeder, W. P. Pratt, Jr., R. Loloee, *J. Magn. Magn. Mater.* , **94**, L1 (1991).

[121] G. Gubbiotti, M. Madami, S. Tacchi, G. Carlotti, T. Okuno *Phys. Rev.* B, **73**, 144430 (2006).

[122] K. S. Buchanan, K. Yu. Guslienko, A. Doran, A. Scholl, S. D. Bader, V. Novosad, *Phys. Rev.* B, **72**, 134415 (2005).

[123] http://www.elettra.trieste.it.

[124] R. D. McMichael, M. D. Stiles, *J. Appl. Phys.*, **97**, 10J901 (2005).

[125] G. Gubbiotti, G. Carlotti, T. Okuno, M. Grimsditch, L. Giovannini, F. Montoncello, F. Nizzoli, *Phys. Rev.* B, **72**, 184419 (2005).

[126] L. Giovannini, F. Montoncello, F. Nizzoli, G. Gubbiotti, G. Carlotti, T. Okuno, T. Shinjo, M. Grimsditch, *Phys. Rev.* B, **70**, 172404 (2004).

[127] P. Vavassori, V. Bonanni, A.Busato, D. Bisero, G. Gubbiotti, A. O. Adeyeye, S. Goolaup, N. Singh, C. Spezzani, M. Sacchi, *J. Phys. D: Appl. Phys.*, **41**, 134014 (2008).

[128] R. P. Cowburn, D. K. Koltsov, A. O. Adeyeye, M. E. Welland, D. M. Tricker, *Phys. Rev. Lett.*, **83**, 1042 (1999).

[129] M. R. Pufall, C. Platt, A. Berger, *J. Appl. Phys.*, **85**, 4818 (1999).

[130] P. Vavassori, V. Bonanni, A.Busato, G. Gubbiotti, M. Madami, A. O. Adeyeye, S. Goolaup, N. Singh, C. Spezzani, M. Sacchi, *J. Appl. Phys.*, **103**, 07C512 (2008).

[131] M. Madami, S. Tacchi, G. Gubbiotti, V. Bonanni, D. Bisero, P. Vavassori, A. O. Adeyeye, S. Goolaup, N. Singh, C. Spezzani, submitted to *J. Appl. Phys.*, (2008).

List of publications

1. *Magnetization reversal and spin waves in exchange coupled NiFe/Cu/Co nanodisks*
   M. Madami, S. Tacchi, G. Gubbiotti, V. Bonanni, D. Bisero, P. Vavassori, A. O. Adeyeye, S. Goolaup, N. Singh, C. Spezzani
   in press on the Journal of Applied Physics.

2. *Shape and thickness effects on the magnetization reversal of Py/Cu/Co nanostructures*
   V. Bonanni, D. Bisero, P.Vavassori, G. Gubbiotti, M. Madami, A.O. Adeyeye, S. Goolaup, N. Singh, T. Ono, C. Spezzani
   submitted to the Journal of Magnetism and Magnetic Materials.

3. *Magnetostatic dipolar domain wall pinning in chains of Permalloy triangular rings micromagnets*
   P. Vavassori, D. Bisero, V. Bonanni, A. Busato, M. Grimsditch, K. M. Lebecki, V. Metlushko, B. Ilic
   Physical Review B, **78**, 174403 (2008).

4. *Magnetostatic and exchange coupling in the magnetization reversal of trilayer nanodots*
   P. Vavassori, V. Bonanni, A. Busato, G. Gubbiotti, A. O. Adeyeye, S. Goolaup, N.Singh, C. Spezzani, M. Sacchi
   J. Phys. D: Appl. Phys., **41**, 134014 (2008).

5. *Static and dynamical properties of circular NiFe/Cu/Co nanodisks*
   P. Vavassori, V. Bonanni, A. Busato, G. Gubbiotti, M. Madami, A. O. Adeyeye, S. Goolaup, N. Singh, C. Spezzani, M. Sacchi
   J. Appl. Phys., **103**, 07C512 (2008).

6. *Cross-over from coherent rotation to inhomogeneous reversal mode in in-*

teracting ferromagnetic nanowires

P. Vavassori, V. Bonanni, G.Gubbiotti, A.O. Adeyeye, S. Goolaup, N. Singh

J. Magn. Magn. Mater., **31**, e31-e34 (2007).